Density Functional Theory Studies of Furfural Hydrodeoxygenations on Various Catalysts

by

He Dong

Master of Science (MSc.), Queen's University Belfast, 2015

A Dissertation Submitted in Partial Fulfillment
of the Requirements for the Degree of

Doctor of Philosophy

in the Graduate Academic Unit of Chemical Engineering

Supervisor: Ying Zheng, Ph.D., Chemical Engineering

Examining Board: Brian Lowry, Ph.D., Chemical Engineering

Felipe Chibante, Ph.D., Chemical Engineering

Stijn De Baerdemacker, Ph.D., Chemistry

External Examiner: Qingfeng Ge, Ph.D., Department of Chemistry and Biochemistry, Southern Illinois University

This thesis is accepted by the
Dean of Graduate Studies

THE UNIVERSITY OF NEW BRUNSWICK

August, 2019

©He Dong, 2019

ABSTRACT

Furfural conversions via hydrodeoxygenation pathways were thoroughly investigated by using density functional theory (DFT) calculations on the Ru/Co_3O_4 surface, Re/Pt bimetallic system, and Ni_2P (0001) surface, respectively.

On the Ru/Co_3O_4 surface, it was found that an oxygen vacancy was necessary to be generated in the form of water for the subsequent hydrodeoxygenation of furfural. In order to generate 2-methylfuran, the reaction initiated from hydrogenation of furfural into furyl–CH_2O alkoxide intermediate, followed by C–O bond cleavage, and finally the hydrogenation of the unsaturated furyl–CH_2 species. This reaction pathway was both kinetically and thermodynamically facile. Comparing with the group X metals and ruthenium, the decarbonylation pathway to produce furan and carbon monoxide was inhibited on Ru/Co_3O_4 surface by the adsorption geometry.

In the Re/Pt bimetallic system, it was found that the kinetically favoured product was furfuryl alcohol, while the 2-methylfuran and water were the thermodynamically favoured products. Based on the calculations, the hydrodeoxygenation product 2-methylfuran was achievable via the hydrogenation of furfural into hydroxyalkyl species, followed by C–OH bond cleavage, and successive hydrogenations of the furyl–CH intermediate. However, the production of 2-methylfuran was prohibited as the oxidised Re surface cannot accept further oxygen deposition, because the removal of oxygen in the form of water via hydrogenations was difficult at the experimental condition. Comparing the results from the Re/Pt system with those on a monometallic flat Pt surface, we were able to demonstrate

that incorporation of the oxophilic metals to active hydrogenation metals could promote the hydrodeoxygenation route by reducing the barrier of C–O bond cleavage.

As the Ni_3P_2-termination was more stable than the Ni_3P_1-termination in Ni_2P (0001) surface, it was mainly focused in the calculations. The generation of 2-methylfuran was favoured via hydrogenation to hydroxyalkyl species, followed by the cleavage of C-OH bond and successive hydrogenations, which indicated that the furfuryl alcohol was not a necessary intermediate for the 2-methylfuran formation. During the further conversion of 2-methylfuran, the ring-hydrogenation pathway to generate 2-methyltetrahydrofuran was kinetically favoured than the ring-opening pathway to produce 2-pentanone. The formation of difurfuryl ether could not be achieved without the participation of phosphorus. The adsorption geometry of furfural was the main factor which inhibited the decarbonylation reaction to generate furan on Ni_3P_2-termination.

Based on the comparisons of these three systems for the hydrodeoxygenation of furfural, Ru/Co_3O_4 system was the best choice which led to a high selectivity of the desire product 2-methylfuran while inhibited the by-products formation.

ACKNOWLEDGEMENTS

Firstly, I would like to express my deepest gratitude to my supervisor, Dr. Ying Zheng, for her persistent guidance and continuous encouragement throughout my Ph.D. study. Her demonstration of a strong enthusiasm for research and a strict scientific attitude will benefit me for my entire life. I also want to express heartfelt thanks to Dr. Peijun Hu, my co-supervisor, I learnt a great deal through our discussions about the density functional theories which applied in the calculations. His knowledge and novel ideas inspired me to solve the problems within my research. This thesis could not have been completed without their guidance, assistance and encouragement.

Many thanks to the previous and current members of our research group who helped me diligently, which allowed me to accomplish the projects of my Ph.D. I am extremely grateful to my research colleagues, Zihao Yao, Chenxi Guo, Yu Mao and Peter Rice. Zihao Yao and Chenxi Guo helped me a lot at the beginning of my Ph.D. career, I cannot get experienced in the calculation field without them. Yu Mao, he illustrated the concepts of calculations when I was confused. My smart friend Peter, I often got inspired based on the discussions with him.

I gratefully thank the Natural Sciences and Engineering Research Council of Canada for the financial assistance.

Last but not least. *¡Muchas gracias a mis padres, y el hermano!*

List of Abbreviations

DFT – density functional theory

FT – Fischer-Tropsch

FUR – furfural

FA – furfuryl alcohol

2-MF/MF – 2-methylfuran

2-MTHF – 2-methyltetrahydrofuran

HDO – hydrodeoxygenation

DCO – decarbonylation

VASP – Vienna ab initio simulation package

vdw – Van der Waals forces

PAW – project-augmented wave

XRD – X-ray diffraction

ZPE – zero point energy

IS – initial state

FS – final state

TS – transition state

Table of Contents

ABSTRACT ii
ACKNOWLEDGEMENTS iv
List of Abbreviations v
Table of Contents vi
List of Figures x
Chapter 1 Introduction 1
1.1. Background 1
1.2. Objectives and thesis outline 3
Chapter 2 Literature review 5
2.1. Development of biofuels 5
2.1.1. First generation biofuels 5
2.1.2. Second generation biofuels 5
2.1.3. Properties of furfural and 2-methylfuran 6
2.2. Upgrading of furfural 7
2.2.1. Monometallic catalysts 7
2.2.2. Bimetallic catalysts 10
2.2.3. Phosphide catalysts 13
2.3. Density functional theory studies of furfural conversion 13
Chapter 3 Method 16
3.1. Basic concepts 16
3.1.1. Arrhenius equation and transition state theory 16
3.1.2. Heterogeneous catalysis 17

3.2. Theory and computational methods 20

3.2.1. Overview of electronic structure and density functional theory 20

3.2.2. Main approximations 28

3.2.3. Technical aspects 31

Chapter 4 DFT Study of Direct Furfural Conversion to 2-Methylfuran on Ru/Co_3O_4 Surface 39

4.1. Introduction 39

4.2. Computational methods 39

4.3. Results 42

4.3.1. Vacancy formation on Co_3O_4 and Ru/Co_3O_4 surfaces 42

4.3.2. Reaction pathways of 2-methylfuran generation 47

4.4. Discussions 53

4.4.1. Vacancy generation tendency of Co_3O_4 and Ru/Co_3O_4 via hydrogenations 53

4.4.2. Competitions of the 2-methylfuran formation pathways 54

4.4.3. Synergistic effects between Ru metal and Co_3O_4 support in furfural conversion 57

4.4.4. Factors which inhibited the decarbonylation of furfural on Ru/Co_3O_4 61

4.5. Conclusions 61

Chapter 5 DFT Study of Furfural Conversion on Re/Pt Bimetallic Surface: Synergetic Effect on the Promotion of Hydrodeoxygenation 63

5.1. Introduction 63

5.2. Computational methods 63

5.3. Results 65

5.3.1. Adsorption of intermediates (furfural, furfuryl alcohol, and 2-methylfuran) . 65

5.3.2. Mechanism of furfural conversions 66

5.4. Discussions 80

5.4.1. Determination of the selectivity of hydrogenation and hydrodeoxygenation routes at 403 K on Re/Pt surface 80

5.4.2. Rhenium effects on the C-O bond and C-C bond cleavages 84

5.4.3. Synergistic effects in Re/Pt system 87

5.5. Conclusions 87

Chapter 6 DFT Study of Furfural conversion on $Ni_2P(0001)$ 89

6.1. Introduction 89

6.2. Method 90

6.3. Results and discussions 92

6.3.1. Adsorption of intermediates (furfural, furfuryl alcohol, and 2-methylfuran) . 92

6.3.2. Reaction mechanisms 93

6.4. Conclusions 130

Chapter 7 Conclusions and Recommendations 132

7.1. Conclusions 132

7.1.1. Furfural hydrotreating on Ru/Co_3O_4 surface 132

7.1.2. Furfural upgrading on Re/Pt bimetallic surface 133

7.1.3. Furfural conversion on Ni_2P (0001) surface 133

7.2. Recommendations 134

Bibliography 136

Curriculum Vitae

List of Figures

Figure 3-1 A catalyst lowers the activation energy barrier (E_a) of a reaction 18

Figure 3-2 Illustration of the procedure to find the transition state using the constrained minimisation technique 32

Figure 4-1 a) Schematic illustration of vacancy formation via hydrogenations of threefold oxygen on the Co_3O_4(110) surface 42

Figure 4-1 b) Mechanism of vacancy formation via hydrogenations of threefold oxygen on the Co_3O_4(110) surface 43

Figure 4-2 a) Schematic illustration of vacancy formation via hydrogenations of threefold oxygen on Ru/Co_3O_4 surface 45

Figure 4-2 b) Mechanism of vacancy formation via hydrogenations of threefold oxygen on Ru/Co_3O_4 surface 47

Figure 4-3 Schematic illustration of reaction pathways of furfural conversion to furfuryl alcohol on Ru(0001) surface 48

Figure 4-4 a) Schematic illustration of 2-methylfuran formations via hydrodeoxygenations of furfural and furfuryl alcohol on the Ru/Co_3O_4 surface 51

Figure 4-4 b) Mechanism of 2-methylfuran formations via hydrodeoxygenations of furfural and furfuryl alcohol on the Ru/Co_3O_4 surface 53

Figure 4-5 Reaction profiles of oxygen vacancy generations on the Co_3O_4 and Ru/Co_3O_4 surfaces 54

Figure 4-6 Reaction profile of Furfuryl alcohol formations on the Ru(0001) surface 55

Figure 4-7 Reaction profile of 2-methylfuran formations on the Ru/Co_3O_4 surface 57

Figure 4-8 Charge analysis of the structures..... 60
Figure 5-1 Top and side views of the Re/Pt surface structure and the most stable adsorption geometries..... 66
Figure 5-2 Adsorption of hydrogen atom on Re/Pt bimetallic system..... 67
Figure 5-3 a) Reaction profile of furfural conversions to furfuryl alcohol..... 68
Figure 5-3 b) Mechanisms of furfural conversion to furfuryl alcohol..... 68
Figure 5-4 a) Reaction profile of water formation via successive hydrogenations of oxygen atom..... 71
Figure 5-4 b) Mechanism of successive hydrogenations of oxygen into water..... 71
Figure 5-5 a) Reaction profile of 2-methylfuran formation via direct cleavage of C-OH bond of furfuryl alcohol..... 73
Figure 5-5 b) Mechanism of 2-methylfuran formation via direct cleavage of C-OH bond of furfuryl alcohol..... 74
Figure 5-6 a) Reaction profile of 2-methylfuran formation via the cleavage of C-O bond of alkoxide intermediate..... 75
Figure 5-6 b) Mechanism of 2-methylfuran formation via the cleavage of C-O bond of alkoxide intermediate..... 75
Figure 5-7 a) Reaction profile of 2-methylfuran formation via the cleavage of C-OH bond of hydroxyalkyl intermediate..... 77
Figure 5-7 b) Mechanism of 2-methylfuran formation via the cleavage of C-OH bond of hydroxyalkyl intermediate..... 77
Figure 5-8 a) Reaction profile of 2-methylfuran formation via the direct cleavage of C-O bond of furfural..... 78

Figure 5-8 b) Mechanism of 2-methylfuran formation via the direct cleavage of C-O bond of furfural 79
Figure 5-9 Mechanism of furfural dehydrogenation 80
Figure 5-10 Free energy reaction profiles at 403 K in Re/Pt bimetallic system 82
Figure 5-11 Key steps of furfural hydrodeoxygenation reaction structures on Pt(111) ... 87
Figure 6-1 Top and side views of the Ni_3P_2-termination surface structure and the most stable adsorption geometries 92
Figure 6-2 Adsorption geometry of hydrogen atom on Ni_3P_2-termination surface 94
Figure 6-3 a) Reaction profile of water formation via successive hydrogenations of oxygen atom 97
Figure 6-3 b) Mechanisms of successive hydrogenations of oxygen into water 98
Figure 6-3 c) Charge analysis of the step of hydrogenation of hydroxyl species at Ni trimer site 99
Figure 6-3 d) Charge analysis of the step of hydrogenation of hydroxyl species at Ni-P bridge site 100
Figure 6-4 a) Reaction profile of furfuryl alcohol formations via successive hydrogenations of furfural 103
Figure 6-4 b) Mechanisms of furfural conversion to furfuryl alcohol 104
Figure 6-5 Mechanism of 2-methylfuran formation via direct cleavage of C-OH bond of furfuryl alcohol 106
Figure 6-6 Mechanism of 2-methylfuran formation via the cleavage of C-OH bond of hydroxyalkyl intermediate 107

Figure 6-7 Mechanism of 2-methylfuran formation via the direct cleavage of C-O bond of furfural 108
Figure 6-8 a) Reaction profile of 2-methylfuran formations 111
Figure 6-8 b) Charge analysis of the C-OH cleavage step in pathway 1 112
Figure 6-8 c) Charge analysis of the C-OH cleavage step in pathway 2 113
Figure 6-8 d) Charge analysis of the C-O cleavage step in pathway 3 114
Figure 6-9 a) Reaction profile of furan formation via the decarbonylation of furfural on Ni_3P_1-termination surface 117
Figure 6-9 b) Mechanism of furan formation via the decarbonylation of furfural on Ni_3P_1-termination surface 118
Figure 6-9 c) Charge analysis of furfural adsorption geometries on Ni_3P_2 and Ni_3P_1 termination surfaces 120
Figure 6-10 a) Adsorption geometry of difurfuryl ether on Ni_3P_2-termination surface . 122
Figure 6-10 b) Reaction profile of difurfuryl ether formation from furfural 123
Figure 6-10 c) Mechanism of difurfuryl ether formation 123
Figure 6-10 d) Charge analysis of the dimerisation step 124
Figure 6-11 a) Reaction profile of 2-methyltetrahydrofuran formation via the successive hydrogenations of 2-methylfuran 125
Figure 6-11 b) Mechanism of 2-methyltetrahydrofuran formation via successive hydrogenations of 2-methylfuran 126
Figure 6-12 a) Adsorption geometry of 2-pentanone on Ni_3P_2-termination surface 128
Figure 6-12 b) Reaction profile of 2-pentanone formation from 2-methylfuran 128
Figure 6-12 c) Mechanism of 2-pentanone formation from 2-methylfuran 129

Chapter 1 Introduction

1.1. Background

In 2016, 85.5% energy consumption of the world was derived from fossil resources.[1] It is obvious that the energy demand of our society is mainly dependent on the utilisation of fossil fuel resources, which is also playing an important role in the acceleration of economic growth.[2, 3] However, environmental problems were revealed during the application of these energy resources which include climate change, greenhouse gas emissions, global warming, petroleum deposits decrease and crude oil prices increase.[4-8] These factors promote people on the development of renewable energy.[9-11] Due to the features of CO_2 consumption, high abundance in earth and eco-friendly application, biomass have attracted tremendous attention,[6, 7, 12-18] which is a cost-efficient source of liquid biofuels and organic chemicals.[16, 19]

Biofuels, derived from plant biomass, are the only current carbon neutral, renewable liquid fuels alternative to fossil fuels.[20] In the first generation biofuels, the main types used commercially are biodiesel and bioethanol, which are produced through transesterification of vegetable oil and fermentation of sugar respectively. However, there are some environmental and economic limitations upon the application of the first generation of biofuels, such as increasing the food price due to the cultivation of feedstocks competes with food production for arable land, the reduction in greenhouse gas emissions is very limit and the fuels produced are not cost competitive to those from fossil fuels without subsidies,[21] which lead to the development of second generation biofuels.

The second generation biofuels are originated from lignocellulosic materials,[22] they have additional benefits to overcome the defects of the first generation biofuels, such as non-competing with food cultivation, existing in high abundance, being inexpensive, and non-edible;[23-26] which seems to be an environmentally benign option for the sustainable production of chemicals and fuels.[7, 27-31]

However, there are some properties attributed to the high oxygen content of biofuels which prevent the direct applications such as low energy density, thermal/chemical instability, high acidity, corrosiveness, high viscosity and immiscibility with hydrocarbon fuels.[32-36] Therefore, oxygen removal is necessary before the utilisation of biofuels.[37]

As one of the top value added chemicals derived from biomass,[27] furfural is mainly treated as a typical compound for hydrodeoxygenations to represent the upgrading of biofuels. They can be converted via decarbonylation, hydrodeoxygenation and ring-opening reactions. In order to generate the substitutions of petroleum, the C/H ratio has to be maintained, hence the hydrodeoxygenation route is required to be facilitated.

In this thesis I use DFT calculations to identify the functionalities of different catalysts at the atomic scale, get better understanding of their mechanisms and provide insights for the development of more economical hydrodeoxygenation catalysts.

1.2. Objectives and thesis outline

The ultimate objective is to provide insights for developing a catalyst that promotes the hydrodeoxygenation of furfural to generate 2-methylfuran, which could keep hydrogen consumption to a minimum and obtain the maximum amount of gasoline fuel substitutions. The specific objectives of the study are described as follows:

(1) Investigate the coordination effects between the metal and oxide support of Ru/Co_3O_4 and the factors that promote the direct elimination of aliphatic oxygen and inhibit the decarbonylation of furfural.

(2) Study the incorporation effects of oxophilic metal Rhenium to the active metal Platinum for the hydrodeoxygenation of furfural.

(3) Identify the effects of phosphorus addition on nickel which perform the outstanding generation of 2-methylfuran to represent the hydrodeoxygenation ability of metal phosphides.

Overall, the mechanisms of furfural conversions on different types of catalysts were presented by DFT study, their advantages in hydrodeoxygenation of furfural were illustrated, and hence better insights for the development of more economical hydrodeoxygenation catalysts were found.

Chapter 2 summarises the history of biofuels production, which emphasised at the furfural conversions based on the development of second generation biofuels.

Chapter 3 presents an overview of the theories and computational methods applied in the DFT calculations.

Chapter 4 illustrates the furfural conversion mechanisms on Ru/Co_3O_4 with the features of catalyst discussed.

Chapter 5 describes the furfural upgrading routes on Re/Pt bimetallic surface with comparisons to the Pt monometallic surface.

Chapter 6 studies the properties of Ni_2P catalyst which make it capable of doing hydrodeoxygenations by presenting the mechanisms of furfural conversion.

Chapter 7 summarises the main conclusions of the work and give recommendations for future work.

Chapter 2 Literature review

2.1. Development of biofuels

2.1.1. First generation biofuels

The two main types of first generation biofuels used commercially are biodiesel and bioethanol. Biodiesel is fatty acid methyl esters which serves as a diesel fuel substitute. The production of biodiesel is achieved by transesterification of the triglyceride from vegetable oil with methanol, which gives a high value chemical glycerol as a by-product.[38, 39] While bioethanol serves as a substitute of gasoline and it is generated via the fermentation of starch or sugar.

Up to now, as the agricultural crop feedstocks of biodiesel and bioethanol are also used for food production, their feedstock price has increased due to the high demand,[40] which promotes the development of second generation biofuels.

2.1.2. Second generation biofuels

Compared with the first generation biofuels, the second generation biofuels are generated from biomass with more eco-friendly properties like being carbon neutral and highly abundance.[41] The feedstocks of second generation biofuels are non-edible crops, which are mainly made up of lignocellulosic materials. The lignocellulosic biomass is composed of cellulose (40-50%), hemicellulose (25%-35%) and lignin (15-20%) respectively.[16, 42, 43] It seems to be the most suitable source for biorefinery,[7, 29, 44, 45] and the biofuels can be obtained via the treatment processes such as gasification, pyrolysis and hydrolysis.[29, 46-48]

The gasification process generates syngas CO and H_2, which can be upgraded by the operation of Fischer-Tropsch and methanol synthesis.[49, 50] Bio-oil is the main product from pyrolysis, which is a thermal degradation process of biomass in the absence of oxygen.[47, 51-53] While hydrolysis can convert cellulose and hemicellulose to a wide range of biofuels and platform molecules,[3, 6, 16] which includes polyols such as glycerol and arabitol, monosaccharides such as glucose and xylose, furanics such as furfural and 5-hydroxymethylfurfural, and acids such as levulinic acid and lactic acid.[16, 27, 29]. Among these chemicals, furfural presents a strong connection between the biofuel-chemical industry and biomass resources.

2.1.3. Properties of furfural and 2-methylfuran

Furfural has a molecular weight of 96.08 g/mol with a chemical formula of $C_5H_4O_2$, it is a colourless oily liquid with a boiling point of 162°C.[54] Due to the aromatic character of the furyl ring and its intermediate polarity, it is both soluble in non-polar compounds such as benzene and highly polar compounds such as water and ethanol.[55] Furfural is generally produced by acidic catalysed dehydration of xylose,[56-59] which is the most abundant monomer in hemicellulose that exists in agricultural wastes such as corncobs and cornstalks.[60-63] The world production of furfural is estimated at 280,000 ton per year with 90% generated in China, South Africa, and Dominican Republic.[56, 59]

2-methylfuran has a molecular weight of 82.10 g/mol with a chemical formula of C_5H_6O, it is a colourless to pale yellow liquid with a boiling point range of 63-66°C.[64] It has a low polarity which makes it only slightly soluble in water. Based on the comparison with

ethanol and gasoline, it has several outstanding physical properties to be a better fuel alternative to gasoline than ethanol, such as a closer boiling point to gasoline, similar energy density and higher octane number than gasoline.[65] The production of 2-methylfuran is mainly through dehydration and hydrogenolysis of cellulose.[64, 66]

2.2. Upgrading of furfural

In order to produce fuel substitutes, the deoxygenation of furfural is necessary. It can be converted to short chain fuel via hydrodeoxygenation and etherification. The long chain fuel is also achievable via the aldol condensation with ketones followed by hydrodeoxygenations.[2, 67, 68] After the comparison of the potential products, my research topics were mainly focused on hydrodeoxygenation of furfural to generate the desire product 2-methylfuran, which was proved to be a promising liquid fuel with a higher octane value and energy density than ethanol,[69, 70] it was also tested on the road over 90,000 km with prospective results reported.[44]

2.2.1. Monometallic catalysts

In the interest of generating 2-methylfuran, the interaction between furyl ring and metal surface should be avoided and the hydrogenolysis of the carbonyl bond should be facilitated. Therefore, monometallic catalysts are not promising options for the production of 2-methylfuran. For instance, Ni is an excellent hydrogenation active metal, but it provides a huge interaction to the furyl ring. As Sitthisa et al. applied Ni/SiO_2 catalyst for the upgrading of furfural, the major product was furan and further ring opening compounds such as butane and butanol were detected.[71]

Similar to Ni, noble metals like Pd and Pt are also good at hydrogenation, but the ring interaction is less than that on Ni, which has less ring-opening products during the furfural conversions. Zhao et al. performed hydrogenation of furfural on 5wt% Pd/SiO_2, 70.9% yield of furfuryl alcohol was obtained at a conversion of 75.0%.[72] Sitthisa et al. achieved 85% conversion at 250°C with a major product of 59% furan, due to the stable adsorption conformation of the acyl species at high temperatures.[71] Stevens et al. also claimed that by using supercritical CO_2 as the solvent, where the hydrogen and furfural were both highly soluble, 98% yield of furan was obtained at 100% conversion under the 5wt% Pd/C catalysis.[73] Ishida et al. also found the furan was the major product with a selectivity of 86% on Pd/ZrO_2.[74] Biradar et al. detected 66% furfuryl alcohol by using 3wt% Pt/C at a conversion of 89.3%.[75] Taylor et al. attempted furfural conversion on Pt/gamma-Al_2O_3, with furfuryl alcohol got a selectivity of 99% from overall 80% conversion at 50°C.[76]

Ruthenium is also a popular option in monometallic hydrodeoxygenation of furfural. Vlacho et al. attempted the catalytic hydrogen transfer process of furfural on 5wt% Ru/C, which gave a major product of 2-methylfuran at 61% yield in a conversion of 95%.[77] Biradar et al. also detected 17% 2-methylfuran on the 3wt% Ru/C at a conversion of 57.3%, but the tetrahydrofurfural was the main product at 40% selectivity, which was converted from furfuryl alcohol.[75]

Copper-based catalysts have lower hydrogenation ability than the noble metals, which could selectively hydrogenate and hydrogenolyse the carbonyl group, and the hydrogenation of the furyl ring is also avoided due to the tilted adsorption mode of furfural.

Lesiak et al. showed that the furfuryl alcohol was the only product when furfural conversion was performed on 5% Cu/Al_2O_3 at an overall conversion of 81%.[78] Sitthisa et al. operated liquid phase furfural conversion on 10wt% Cu/SiO_2, the product was a mixture of furfuryl alcohol with a small portion of 2-methylfuran in the temperature range between 230-290^oC.[71] While Dong et al. achieved the vapour phase furfural upgrading on Cu/SiO_2 at a full conversion, with 89.5% of 2-methylfuran detected;[79] and this group also introduced an ammonia evaporation method for the Cu/SiO_2 catalyst preparation, which led to the formation of a copper phyllosilicate phase. The copper was more dispersed and more acid sites were found than the conventional precipitation method, 95.5% 2-methylfuran were obtained at 200^oC as a result.[80]

Ir-based catalysts have also been applied for hydrodeoxygenation of furfural. Date et al. performed furfural conversion on Ir/C catalyst, 95% selectivity of 2-methylfuran was achieved at 220^oC with a low hydrogen pressure of 100 psig. They found that furfuryl alcohol was also a by-product at a lower temperature, and the ring saturation was facilitated at a higher temperature.[81]

Overall, in order to achieve the selective hydrogenolysis of the carbonyl group in furfural, the interaction between metal and the furyl ring should be hindered, and the oxophilicity of catalyst should be altered to promote the C-O bond cleavage. Based on the consideration of these factors, the development of bimetallic catalysts become popular recently.

2.2.2. Bimetallic catalysts

Generally, the fundamental idea of constructing bimetallic catalysts is that, by incorporating oxophilic metals into active hydrogenation metals, the hydrogenolysis ability of furfural is improved while preserving its aromaticity and prohibiting the decarbonylation reaction.

Sitthisa et al. performed $NiFe/SiO_2$ upgrading of furfural at 250^oC. A selectivity of 39.1% 2-methylfuran was observed from a total conversion of 96.3%, while only 1.4% selectivity to 2-methylfuran in a conversion of 50.9% by using Ni/SiO_2 catalyst. These results indicated that the addition of oxophilic Fe metal promoted the formation of 2-methylfuran.[82] Wang et al. also obtained 2-methylfuran as the major product on carbon supported NiFe.[83] It was found by Jiménez-Gómez et al., that the incorporation of MgO to Ni successfully reduced the strong interaction between Ni and furyl ring, which led to furan generation with 88% selectivity.[84] Seemala et al. investigated the support effect on NiCu bimetallic catalyst, it was found that the Al_2O_3 promoted the hydrogenation to form furfuryl alcohol and tetrahydrofurfuryl alcohol, while the TiO_2 helped the carbonyl bond hydrogenolysis to produce 2-methylfuran.[85] While Fu et al. achieved 2-methylfuran production on $NiCu/Al_2O_3$ based on a catalytic hydrogen transfer mechanism, which the furfural was hydrogenated to furfuryl alcohol first, then the C-O bond cleavage was promoted via hydrogen transfer from the formic acid to the alcohol functional group, and the reaction was completed by successive hydrogenation of the FCH_2 species.[86]

Nakagawa et al. incorporated Ir to Pd/SiO_2 at 2°C, which not only improved the conversion from 25% to 61%, but also kept the selectivity to furfuryl alcohol.[87] It was assumed the addition of Ir facilitated the adsorption of furfural via the carbonyl group. Lesiak et al. investigated the effect of copper addition to Pd on Al_2O_3 support, they found that the conversion of furfural was slightly decreased from 100% to 94%, but the selectivity of furfuryl alcohol was increased while the tetrahydrofurfuryl alcohol was decreased, which was consistent to the observation from the copper that the furyl ring was repelled from the surface.[78] Chang group also attempted the incorporation of Cu and Pd in ZrO_2 support, by using 2-propanol as a donor for the catalytic transfer hydrogenation, 63.6% yield of 2-methylfuran was obtained which was higher than on both the Cu and Pd monometallic catalysts.[88] Pino et al. applied the incorporation of Fe to Pd/SiO_2, they obtained the major product of 2-methylfuran. While the gamma Al_2O_3 support made PdFe behave more like Pd/SiO_2, due to the major production of furan.[89]

While Shi et al. showed that the Zn could play a similar role as oxophilic metals for the hydrodeoxygenation of furfural. With the addition of Zn to Pt, the furyl ring was tilted away from the surface, the carbonyl group interacted with surface atoms to promote the formation of furyl-CH species, which could be further converted into 2-methylfuran.[90] Chen et al. studied bimetallic catalysts such as PtRe, PtIn, PtSn; among these experiments, PtRe presented the full conversion of furfural with 95.7% selectivity to furfuryl alcohol; compared with the Pt monometallic catalyst, the selectivity to tetrahydrofurfuryl alcohol was heavily reduced, which indicated the hydrogenation activity of Pt was declined by incorporation of Re.[91] Merlo et al. reported the PtSn catalyst could achieve a high

selectivity to furfuryl alcohol between 96-98% upon the conversion of furfural, the catalyst deactivation was less than the Pt which showed the conversion was doubled after 3 runs.[92] Dohade et al. stated the incorporation of Co to Pt selectivity promoted the C-O bond cleavage which selectively changed the major product from furfuryl alcohol to 2-methylfuran while maintained the conversion.[93] Chen et al. introduced oxophilic metals of Fe, Co, Ni, and Cu to Pt(111), the selectivity for 2-methylfuran generation followed the order of CoPt > FePt > NiPt > CuPt, they also proved that the surface oxygen coverage prohibited the formation of 2-methylfuran.[94]

Jaatinen et al. found that during the addition of Fe to Cu/C, not only improved the conversion, but also increased the product yield of 2-methylfuran from 2.3% to 41%.[95] It was identified that the weak adsorption of furfural and low dissociation of hydrogen limited the further improvement of 2-methylfuran production. The Co incorporation effect on Cu was performed by Seemala et al., as the Co played main role on the ring opening mechanism to favour the C-O cleavage of 2-methylfuran to generate 2-propanol at a yield of 71.1%.[96]

Tomoshige et al. reported the Ir-ReOx/SiO_2 catalyst was a profound catalyst for the hydrogenation of the carbonyl group, which generated over 99% of furfuryl alcohol at a temperature of 30°C.[97]

In summary, based on the incorporation of oxophilic metals, the active hydrogenation metals demonstrate less interaction with the furyl ring, as a result, ring opening and

saturation reactions are inhibited, and the selective hydrogenolysis of the carbonyl group is also facilitated in some cases.

2.2.3. Phosphide catalysts

Recently, transition metal phosphides received much attention for the hydrodeoxygenation of biomass-derived molecules, due to their outstanding activities in hydrodenitrogenation and hydrodesulfurisation.[98, 99] In the hydrodeoxygenation of anisole and guaiacol, Ni_2P showed a greater activity than other metal phosphides like Co_2P, Fe_2P, MoP, and WP.[100, 101] Jiménez-Gómez et al. and Wang et al., performed the hydrodeoxygenation of furfural on Ni_2P, both groups obtained 2-methylfuran as the major product.[102, 103] Bonita et al. used RuMo bimetallic phosphide to upgrade furfural, with 99% selectivity of furfuryl alcohol was detected.[104] Sampath et al. claimed that the Ru phosphide suppressed huge ring interaction than ruthenium monometallic catalyst, due to the addition of phosphorus inhibited the electron back donation to furfural. Hence the decarbonylation pathway became dominant on Ru phosphide.[105]

2.3. Density functional theory studies of furfural conversion

In order to further improve the catalysis, reaction mechanisms on metal surfaces require detailed investigations. The noble metals such as Ni, Pd, and Pt showed strong interaction with the furyl ring, which originated from the sp^2-to-sp^3 hybridisation between the metal and π bonds of furfural.[106] As a result, the furyl ring adsorbed in a parallel conformation on the metal surface with the carbonyl group also bonded to the surface in a η^2(C-O) pattern.[82, 107-111] The η^2(C-O) adsorption mode of furfural led the conversion of the carbonyl

bond to alcohol and further hydrogenolyse to methyl group, while the strong ring-metal interaction could favour the ring-hydrogenation and ring-opening to generate ring-saturation and aliphatic compounds respectively. The decarbonylation of furfural was promoted to produce furan at high temperatures, it was attributed to the η^2(C-O) adsorption mode was transformed into η^1(C).

Vorotnikov et al. performed furfuryl conversion on Pd(111), it was found that the most stable adsorption of furfural was in an acyl pattern, which facilitated the decarbonylation pathway to generate the thermodynamically stable products of furan and carbon monoxide via the steps of deprotonation, followed by C-C bond rupture and rehydrogenation of furyl ring.[112] While the furfural decarbonylation pathway on Pt(111) was also found to follow the same reaction steps as on Pd(111).[110]

On the Ru(0001) surface, Banerjee et al., stated that the ring opening mechanism was favoured both kinetically and thermodynamically to produce pentane via complete hydrodeoxygenation.[113] The furfural conversion on Ni(111) surface was also carried out by the same group, it was found the barrier of C-C bond cleavage was low in a wide range of temperature, which promoted the production of furan. They also investigated the hydrogen coverage effect based on temperature change, the hydrogen adsorption became less thermodynamically favourable upon temperature increase, which resulted the product selectivity to furfuryl alcohol at low temperature, while the linear chain products were promoted at high temperature.[114]

Contrast to the results of noble metals, it was proved that the most stable adsorption geometry of furfural was tilted η^1(O) on Cu(111).[108, 115] Whereas the strong repulsion of furan ring with Cu(111) surface came from the partial overlap of the 3d band of the Cu atoms with the antibonding orbitals of the furan ring.[115, 116] Therefore, the adsorbed hydrogen atoms preferred to react with the carbonyl group to generate furfuryl alcohol.

Bimetallic calculations were also achieved, upon the addition of Fe to Ni(111), the aliphatic carbonyl bond was extended and presented a stronger adsorption strength on the NiFe(111) surface, the distance between oxygens and metal surface were decreased, and the lengths between carbons and the surface were increased, which resulted in a slightly tilted adsorption mode of furfural that favoured the production of 2-methylfuran.[117] A similar observation of C-O bond length extension was also found on Fe/Pt(111) surface.[118]

Chapter 3 Method

3.1. Basic concepts

3.1.1. Arrhenius equation and transition state theory

The Arrhenius equation is an expression to build a relationship between the activation energy of reaction and the rate constant.

$$k = Ae^{\frac{-E_a}{RT}} \qquad \text{Equation 3-1}$$

Where A is known as the pre-exponential factor, E_a is the activation energy, and R is the universal gas constant. Hence, the Arrhenius equation indicates that the reaction rate constant depends exponentially on the activation energy.

Transition State Theory, which was introduced by Eyring in the 1930s, assumes an equilibrium energy distribution among all the reactant and transition states. For a reaction to proceed, the reactants move from the initial state (IS) to the final state (FS), where the transition state (TS) between these two states must be overcome.

By assuming the transition state is in equilibrium with the initial state, the reaction rate constant can be written as:

$$k = \frac{k_B T}{h} e^{\frac{-\Delta^{\neq} G^{\circ}}{RT}} \qquad \text{Equation 3-2}$$

where $\Delta^{\neq} G^{\circ}$ is the Gibbs free energy difference between the initial state and the transition state, k_B is Boltzmann's constant, h is Plank's constant.

By incorporation of the definition of Gibbs free energy:

$$\Delta^{\neq} G^{\circ} = \Delta^{\neq} H^{\circ} - T\Delta^{\neq} S^{\circ} \qquad \text{Equation 3-3}$$

where $\Delta^{\neq}H^{\circ}$ and $\Delta^{\neq}S^{\circ}$ are differences of enthalpy and entropy between the transition state and the initial state respectively.

Then the rate constant can be expressed as:

$$k = \frac{k_B T}{h} e^{\frac{\Delta^{\neq}S^{\circ}}{R}} e^{\frac{-\Delta^{\neq}H^{\circ}}{RT}} \qquad \text{Equation 3-4}$$

Comparing the transition state theory expression for the reaction constant with the Arrhenius equation, it can be established that when the reaction is in the gas phase:

$$E_a = 2RT + \Delta^{\neq}H^{\circ} \qquad \text{Equation 3-5}$$

$$A = \frac{e^2 k_B T}{h} e^{\frac{\Delta^{\neq}S^{\circ}}{R}} \qquad \text{Equation 3-6}$$

Therefore, it is clear that the activation energy E_a is depending on the enthalpy change between IS and TS ($\Delta^{\neq}H^{\circ}$), and the pre-exponential factor *A* is determined by the entropy change between IS and TS ($\Delta^{\neq}S^{\circ}$). By using these equations, we are able to calculate $\Delta^{\neq}H^{\circ}$ and $\Delta^{\neq}S^{\circ}$.

3.1.2. Heterogeneous catalysis

As we know, the most convenient way to increase the reaction rate is to reduce the activation energy E_a, this is the real reason why the catalyst is applied. Basically, there are two type of catalysts used in chemical reactions, they are classified as heterogeneous and homogeneous catalysts. Heterogeneous catalysts are in the different physical states to the reactants, while homogeneous catalysts are in the same physical state as the reactants.

An important feature that distinguishes these two classes of catalyst is that the heterogeneous ones usually generate similar products, but the homogeneous ones provide

special properties to the products such as chirality. The importance of catalysis was reported, as solid state catalysts were involved in about 85% to 90% of all chemical productions.[119] As it is shown in Figure 3-1, the activation barrier is lowered by application of catalyst which can increase the rate of reaction.

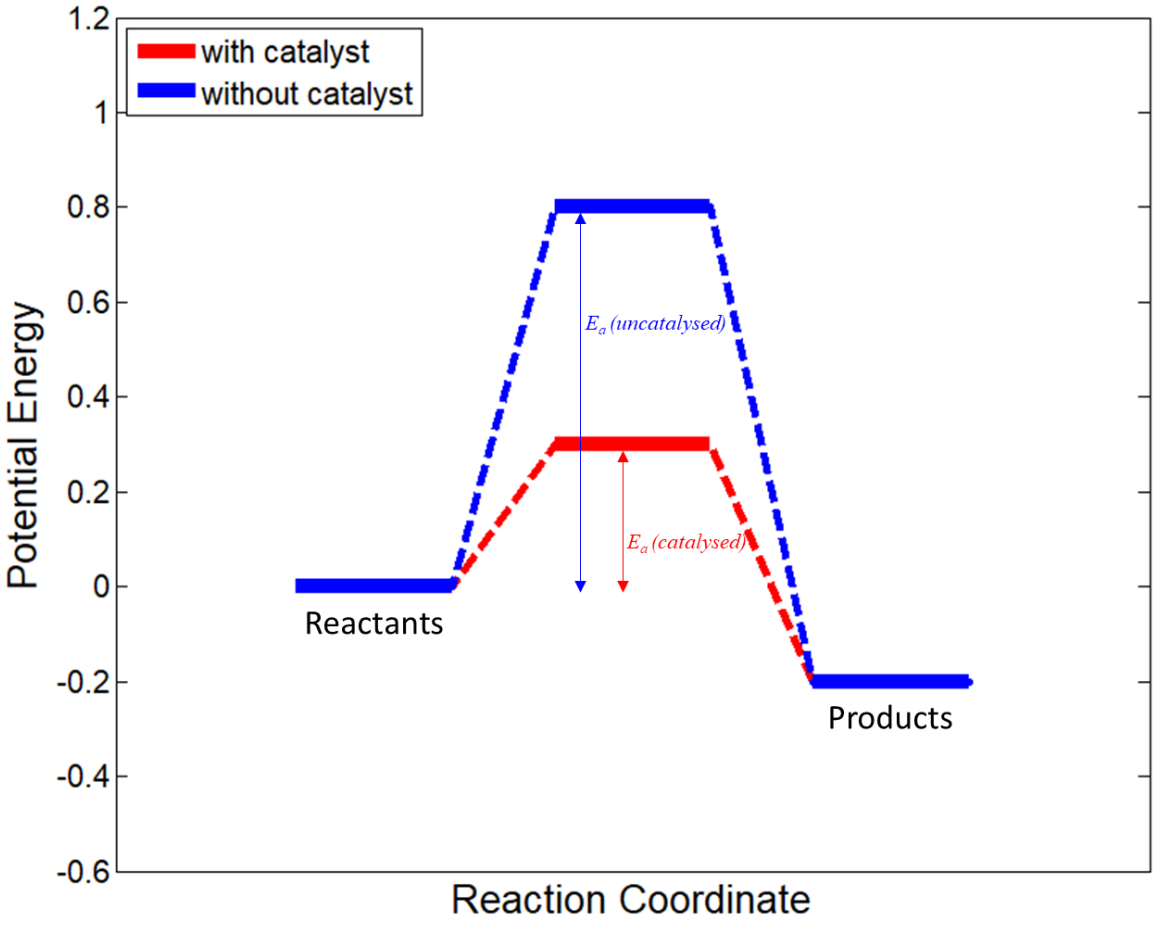

Figure 3-1 A catalyst lowers the activation energy barrier (E_a) of a reaction

Considering heterogeneous catalysis in the solid phase, the reactants in liquid or gaseous phase, it is found that the reaction occurs at the interface between them. In 1915 Langmuir

stated that the catalytic reactions happen on the surface, such as gaseous reactants react after they are adsorbed at specific sites on the surface of solid catalyst.[120]

Up to now, bimolecular surface reactions are classified as the following two types:

(1) The Langmuir-Hinshelwood mechanism, where the reaction initiates between two adsorbed molecules on the solid surface.

(2) The Eley-Rideal mechanism, where the reaction starts by the collision between a gas molecule and an adsorbed molecule on the surface.

The study of heterogeneous reactions entered a new era in the last 40 years,[121-123] as the atomic level pictures of surface reactions could be obtained. By interpreting the electronic properties of the catalytic surfaces, we can construct the understanding of heterogeneous catalysis at an atomic level. In order to identify the surface and adsorbed molecules, experimental approaches such as Ultraviolet Photoelectron Spectroscopy (UPS), Scanning Tunneling Microscopy (STM), Low Energy Electron Diffraction (LEED), and Temperature Programmed Desorption (TPD) have been applied. However, the current technologies cannot provide high resolution to observe rapid reactions.

Nowadays, density functional theory has become a wonderful tool to study the heterogeneous reactions. As a result of simulation, geometrical features and relative energies of reaction states can be calculated, and reaction pathways can be identified as well.

3.2. Theory and computational methods

3.2.1. Overview of electronic structure and density functional theory

3.2.1.1. The Schrödinger equation

Schrödinger equation is the fundamental concept to describe the electronic structure of matter in quantum mechanics:

$$\widehat{H}\Psi = E\Psi \qquad \text{Equation 3-7}$$

where $\widehat{H}$ is the Hamiltonian operator,Ψ is the wavefunction of the system, and E is the energy of the system. The Hamiltonian operator can be separated into two parts, the kinetic energy term $\frac{-\hbar^2}{2m}\nabla^2$ and the potential energy term V:

$$\widehat{H} = \frac{-\hbar^2}{2m}\nabla^2 + V \qquad \text{Equation 3-8}$$

where m is the mass, $\hbar$ is defined as $\frac{h}{2\pi}$, and ∇^2 is the Laplace operator.

However, the application of the Schrödinger equation to obtain accurate results is limited to simple systems such as atomic hydrogen and H_2^+ molecular ion. Hence we are only able to get approximate details in the complex systems.

3.2.1.2. Many Body problem

The Born-Oppenheimer approximation is necessary to be introduced for solving the many body problems.[124] Which proposed that the nuclei can be treated in a frozen state due to the relative motion of an electron is much faster than nuclei, and the electrons are in their ground states. Hence this concept makes the motion of electrons and nuclei that can be reasonably be decoupled as:

$$\Psi(r,R) = \chi(R)\phi(r,R) \qquad \text{Equation 3-9}$$

where $\chi(R)$ and $\phi(r,R)$ are the wavefunctions of nuclei and electrons respectively.

First, the nuclear kinetic energy is neglected to solve the electronic Schrödinger equation:

$$\widehat{H}_e(r,R)\phi(r,R) = E_e\phi(r,R) \qquad \text{Equation 3-10}$$

As the Hamiltonian operator for electron is expressed in the following way:

$$\widehat{H_e} = T + V_{en} + V_{ee} \qquad \text{Equation 3-11}$$

where T is the kinetic energy of electron, V_{en} is the interaction between electrons and nuclei, and V_{ee} is the interaction between electrons respectively.

The equation 3-11 can also be described in a detailed version:

$$\widehat{H_e} = \sum_{i=1}^{n}\left(\frac{-\hbar^2}{2m}\nabla_i^2 + \nu_{ext}(\vec{r_i})\right) + \sum_{i<j}\frac{e^2}{|\vec{r_i}-\vec{r_j}|} \qquad \text{Equation 3-12}$$

where $\nu_{ext}(\vec{r_i})$ is the external (nuclear) potential, e is the electric charge, and $\vec{r_i}$ is radius vector of electron.

Then the nuclear kinetic energy term T_n is reintroduced to solve the nuclear Schrödinger equation:

$$[T_n + E_e(R)]\chi(R) = E\chi(R) \qquad \text{Equation 3-13}$$

As the nuclear motion is mainly depending on the electronic motion, based on application of the Born-Oppenheimer approximation, the many body system is simplified into many electron system.

3.2.1.3. The Hartree-Fock approximation

In order to avoid the complicated mathematics involved in the many electron wavefunction, the problem is often simplified into single-electron formats, which was stated in the Hartree-Fock approximation.[125]

Hartree stated that the total electron wavefunction can be expressed as a product of individual electron wavefunction.

$$\phi(r) = \varphi_1(r_1)\varphi_2(r_2)\varphi_3(r_3)\ldots\varphi_n(r_n) \qquad \text{Equation 3-14}$$

However, as the electrons are fermions, there should be a sign change in the wavefunction upon the exchange of any two electron coordinates.

Then the Slater determinant is used to describe the wavefunction:

$$\Psi_{HF} = \frac{1}{\sqrt{n!}}\begin{vmatrix} \phi_1(s_1,\overrightarrow{r_1}) & \ldots & \phi_n(s_1,\overrightarrow{r_1}) \\ \cdots & \ldots & \ldots \\ \phi_1(s_n,\overrightarrow{r_n}) & \ldots & \phi_n(s_n,\overrightarrow{r_n}) \end{vmatrix} \qquad \text{Equation 3-15}$$

where $\phi_i(s_j,\overrightarrow{r_j}) = \psi_i(\overrightarrow{r_j})\chi_i(s_j)$, $\psi_i(\overrightarrow{r_j})$ is the spatial function and $\chi_i(s_j)$ is the spin function respectively.

Thus, the anti-symmetry is guaranteed, as the sign of the determinant is changed when the rows or columns are interchanging. Also, if any two rows or columns are the same, the determinant is zero, which makes sure the one-electron states cannot be doubly occupied. According to the variational principle of quantum mechanics, the lowest Hartree-Fock energy can then be obtained by self-consistent field iteration.

The Hartree-Fock approximation can be expressed as:

$$E_{HF} = \sum_{i=1}^{n} h_i + \frac{1}{2}\sum_{i,j=1}^{n}(C_{ij} - A_{ij}) \qquad \text{Equation 3-16}$$

with:

$$h_i = \int \psi_i^* (\vec{r}) \left[\frac{-\hbar^2}{2m} \nabla^2 + v_{ext}\right] \psi_i(\vec{r}) d\vec{r} \qquad \text{Equation 3-17}$$

$$C_{ij} = \iint |\psi_i(\vec{r_1})|^2 \frac{e^2}{|\vec{r_1} - \vec{r_2}|} \left|\psi_j(\vec{r_2})\right|^2 d\vec{r_1} d\vec{r_2} \qquad \text{Equation 3-18}$$

$$A_{ij} = \delta(s_i s_j) \iint \psi_i^* (\vec{r_1}) \psi_j(\vec{r_1}) \frac{e^2}{|\vec{r_1} - \vec{r_2}|} \psi_i^* (\vec{r_2}) \psi_j(\vec{r_2}) d\vec{r_1} d\vec{r_2} \qquad \text{Equation 3-19}$$

where h_i is the kinetic energy and electron-nuclei energy integral; C_{ij} is the electron-electron Coulomb interaction integral; and A_{ij} is the exchange energy and also used to represent the electrons are fermions. As the spin electrons prefer to avoid meeting each other, the electrostatic interaction between them is decreased, hence the energy of system is reduced. The presence of the Kroneker delta prefixing in the exchange integral indicates that A_{ij} = 0, unless s_1=s_2.

However, the correlation between unlike spin electrons is completely neglected in the Hartree-Fock approximation. The difference between the Hartree-Fock energy and the exact energy is known as the correlation energy, which is defined as:

$$E_{exact} - E_{HF} = E_{correlation} \qquad \text{Equation 3-20}$$

3.2.1.4. The Hohenberg-Kohn Theorems

In the 1960s, Density Functional Theory was developed to include both the exchange and correlation terms in the total energy calculations. In 1964, Hohenberg and Kohn published two theorems which use electron density as a basis to calculate the electronic structures.[126] The first theorem stated that the electron density $(\rho(\vec{r}))$ can determinate the external

potential $\left(v_{ext}(\vec{r})\right)$ and the electron number by integration over r, then the Hamiltonian of the system can be obtained. Hence the total energy of system can be expressed in terms of the electron density. The second theorem indicated that the minimum value of the functional coincides with the ground state of the system.

The energy functional can be expressed as:

$$E[\rho] = T[\rho] + V_{en}[\rho] + V_{ee}[\rho] \qquad \text{Equation 3-21}$$

where $T[\rho]$ is the kinetic, $V_{en}[\rho]$ is the electron-nuclear, and $V_{ee}[\rho]$ is the electron-electron values respectively. If the energy of interaction between the electrons and external potential is separated out, the equation can be written as:

$$E[\rho] = F_{HK}[\rho] + \int \rho\,(\vec{r}) v_{ext}(\vec{r}) d\vec{r} \qquad \text{Equation 3-22}$$

where $F_{HK}[\rho] = \langle \Psi | T + V_{ee} | \Psi \rangle$ is the Hohenberg-Kohn functional. The Hohenberg-Kohn functional can be expressed as:

$$F_{HK}[\rho] = \frac{1}{2} e^2 \iint \frac{\rho(\vec{r_1})\rho(\vec{r_2}) d\vec{r_1} d\vec{r_2}}{|\vec{r_1} - \vec{r_2}|} + G[\rho] \qquad \text{Equation 3-23}$$

where the electron-electron interaction is separated out, and $G[\rho]$ is the sum of exchange-correlation and kinetic energy values.

The second Hohenberg-Kohn theorem expressed that the minimum energy can be obtained corresponding to the electron density and variation principle of quantum mechanics. Therefore, the variation principle required the density of ground state satisfied the stationary condition:

$$\frac{\delta}{\delta \rho}\{E[\rho] - \mu(\int \rho\,(\vec{r}) d\vec{r} - n)\} = 0 \qquad \text{Equation 3-24}$$

where the undetermined multipliers are employed to make sure the number of electrons was constant, as the electron number n can be calculated by the integration of $\rho(\vec{r})$ over all r.

By incorporation of the equations of 3-22, 3-23, and 3-24, the Euler-Lagrange equation of DFT is constructed as:

$$\frac{\delta E}{\delta \rho} = \mu = \nu_{ext} + \phi_H + \frac{\delta G}{\delta \rho} \qquad \text{Equation 3-25}$$

where ϕ_H is the Hartree potential, and μ is the chemical potential of the system, this equation would be an exact expression of the ground state electron density once we knew the exact form of $F_{HK}[\rho]$, which could make this method applicable to any systems.

3.2.1.5. The Kohn-Sham Equations

For calculation of the ground state energy, Kohn and Sham proposed a method to determine the density $\rho(\vec{r})$ based on the single electron orbital scheme in 1965.[127]

The many-electron wavefunction can be written as a single Slater determinant of one electron wavefunctions as:

$$\left(\frac{-\hbar^2}{2m}\nabla^2{}_i + \nu_\circ(\vec{r})\right)\phi_i^\circ(s,\vec{r}) = \varepsilon_i \phi_i^\circ(s,\vec{r}) \qquad \text{Equation 3-26}$$

And the density $\rho(\vec{r})$ can be expressed as:

$$\rho(\vec{r}) = \sum_{i=1}^{n/2}\sum_s \left|\phi_i^\circ(s,\vec{r})\right|^2 \qquad \text{Equation 3-27}$$

where $\phi_i(s_j,\vec{r_j}) = \psi_i(\vec{r_j})\chi_i(s_j)$, $\psi_i(\vec{r_j})$ and $\chi_i(s_j)$ are the spatial and spin function respectively.

The equation 3-26 and 3-27 are the fundamental concepts of Kohn-Sham method in determination of the ground state density which also satisfy the Euler-Lagrange equation of DFT. Then Kohn and Sham treated the system as non-interacting electrons, which the ground state energy functional is

$$E_{◦}[\rho] = T_{◦}[\rho] + \int \rho(\vec{r}) v_{◦}(\vec{r}) d\vec{r} \qquad \text{Equation 3-28}$$

where $T_{◦}[\rho]$ is the kinetic energy of the non-interacting electrons, and the relative Euler-Lagrange equation is shown as follow:

$$\mu_{◦} = v_{◦}(\vec{r}) + \frac{\delta T_{◦}}{\delta \rho} \qquad \text{Equation 3-29}$$

Because the V_{ee} = 0 when there is no interacting electrons, the many electron wavefunction can be expressed as a single determinant, hence the electron orbitals and density can be calculated from equation 3-26 and 3-27.

Kohn and sham then first redefined the exchange and correlation terms as:

$$E_{xc} = (T - T_{◦}) + (V_{ee} - C) \qquad \text{Equation 3-30}$$

where $(T - T_{◦})$ is the kinetic energy difference between interaction and non-interacting systems, and $(V_{ee} - C)$ is the difference between the electron-electron interaction and the Coulomb energy. Then based on the Euler-Lagrange equation of the real system, they defined the effective potential by introducing the new definition of exchange and correlation.

$$v_{eff}[\rho, \vec{r}] = v_{ext}(\vec{r}) + \phi_H(\vec{r}) + \frac{\delta E_{xc}}{\delta \rho} \qquad \text{Equation 3-31}$$

Notice that if v_{eff} is identical to the $v_{◦}$ in equation 3-29, the correct ground state density of a real interacting system can be obtained by solving the equation 3-29.

Hence Kohn and Sham replaced the $v_{\circ}$ in equation 3-26 by v_{eff} to get

$$\left(\frac{-\hbar^2}{2m}\nabla^2{}_i + v_{eff}[\rho,\vec{r}]\right)\phi_i(s,\vec{r}) = \varepsilon_i\phi_i(s,\vec{r}) \qquad \text{Equation 3-32}$$

And the correct ground state density of the interacting system can be expressed as:

$$\rho(\vec{r}) = \sum_{i=1}^{n/2}\sum_s|\phi_i(s,\vec{r})|^2 \qquad \text{Equation 3-33}$$

Based on equation 3-32 and 3-33, Kohn-Sham provided a method to solve the Euler-Lagrange equation of the real system, which determines the ground state density of the system to get the total energy. Hence in principle, DFT is an exact theory without approximations have been made. However, the exact exchange-correlation functional cannot be obtained to get accurate solution of the Kohn-Sham equations. Up to date, the exact exchange-correlation functional is still unknown, therefore the approximations of exchange-correlation functional are employed at this stage.

3.2.1.6. Local density approximation

One successful expression of the exchange-correlation functional is the local density approximation (LDA).[128] This method assumes the exchange-correlation energy of one election at the position $\vec{r}$ is identical to that electron in a homogeneous electron gas with the same density. Therefore the effects of exchange and correlation at any point $\vec{r}$ are entirely local which are not affected by the adjacent density variation. However, the electron gas is not actually in the homogeneous state. Despite this approximation can predict the molecular geometries and vibrational frequencies with reliable results, the bonding energies cannot get well interpreted with an error exceeded over 10%, due to the exchange-correlation contribution is underestimated at the regions of low density.

3.2.1.7. Generalised gradient approximation

In order to correct the error of overestimated binding energies in LDA, the gradient of electron density at point $\vec{r}$ is introduced by a concept called generalised gradient approximation (GGA),[129] which provides the accuracy of bonding energies as well as the molecular geometries and vibrational frequencies.[129, 130] The functionals that employ the correction based on the gradient are all referred to generalised gradient approximations, the better improvements in the exchange-correlation term, the more accurate results can be obtained.[131] The most common GGA functional used in chemistry is Perdew-Burke-Ernzerhof (PBE).[132]

3.2.2. Main approximations

3.2.2.1. The super-cell approach

In the Kohn-Sham equations, non-interacting electrons moving in an effective potential is used to represent the interacting electrons. However, there are an infinite number of ions involved in solids, which arise two problems need to be solved. The first is description of the electrons requires an infinite number of wavefunctions to be calculated. The second is an infinitely large basis set is necessary to describe all electrons independently. According to the Bloch' theorem,[133] which simplifies the calculation solution by using a finite unit cell which is repeated periodically in 3-dimensional space, followed by applying the Bloch's theorem to the electronic wavefunctions of the periodic system.

Bloch's theorem states that all of the electronic wavefunctions in the periodic solid can be expressed as the product of a wavelike part $exp\left[i\vec{k}\cdot\vec{r}\right]$ and a cell periodic part $f_i(\vec{r})$ like:

$$\psi_i(\vec{r}) = exp\left[i\vec{k}\cdot\vec{r}\right]f_i(\vec{r}) \qquad \text{Equation 3-34}$$

which the cell periodic part $f_i(\vec{r})$ can be represented by using a basis set consisting of plane waves, whose wave vectors are reciprocal lattice vectors of the super cell:

$$f_i(\vec{r}) = \sum_G C_{i,G}\, exp\left[i\vec{G}\cdot\vec{r}\right] \qquad \text{Equation 3-35}$$

where $\vec{G}$ is the reciprocal lattice vectors and defined by $\vec{G}\cdot\vec{l} = 2\pi m$, and $\vec{l}$ is the lattice vector, and m is an integer. Therefore the wavefunction ψ_i can be expressed in terms of a plane wave basis set:

$$\psi_i(\vec{r}) = \sum_G C_{i,k+G}\, exp\left[i\left(\vec{k}+\vec{G}\right)\cdot\vec{r}\right] \qquad \text{Equation 3-36}$$

In addition to the basis sets composed of plane waves, the basis functions are generally expressed as a linear combination of atomic orbitals. Corresponding to the relative distance between the atoms and molecules, the wavefunction exponentially decreases to zero at long distances. There are two types of atomic orbitals used in total energy calculations, namely, the Slater type orbitals (STO), and Gaussian type orbitals (GTO).[134, 135] Generally more GTOs are required to form a suitable basis set than STOs, about three times the GTOs to reach the same accuracy as the STOs. However, as GTOs are more efficient than STOs, this feature makes the GTOs more popular in the calculations. Also, the accuracy of the calculations is depending on the size of the basis set, the larger basis set used, the more accurate results to have.

The electronic wavefunctions are determined by the boundary conditions of system at a limited range of k-points, and the density of the allowed k-points is proportional to the

volume of the solid system. The infinite number of k-points is used to describe the infinite number of electrons in the solid system, and only a finite number of electronic states are occupied at each k-point.

Therefore, instead of calculating an infinite number of wavefunctions directly, the Bloch's theorem employs a finite number of wavefunctions at an infinite number of k-points to solve the problem. While the calculation of wavefunctions at an infinite number of k-points can be achieved by using the k-point sampling technique, as the wavefunctions at adjacent regions of k-space are almost equal, calculation at a sample number of k-points is enough to describe the wavefunctions. Generally, the more k-points used, the more accurate a calculation. However, more k-points lead to the higher consumption of the computational resources, so it requires to build a balance between the accuracy and resource consumption.

3.2.2.2. The pseudo-potential approximation

The Bloch's theorem implicates that the electronic wavefunctions can be expressed in terms of plane waves. However, a plane wave basis set is not an adequate choice to describe the electronic wavefunctions, due to an enormous amount of plane waves are required to describe core orbitals and the wavefunctions of the valence electrons that oscillate in the core region. In order to simplify the calculation, the amount of plane waves involved have to be limited, which is achieved by introducing the pseudo-potential approach.[136-139] This approach used a weaker pseudo-potential to replace the core electrons and the strong ionic potential. Despite the application of pseudo-potential affects the accuracy of the total energy, the error can be cancelled when calculating the relative energies such as the

activation energies and reaction energies where the same approximation is used in all of the calculations.

3.2.3. Technical aspects

3.2.3.1. Software and codes

The software employed for visual modelling is materials studio® running in windows. It is a product of Accelrys Inc. (Material studio is a registered trademark of Accelrys Inc.)

The DFT code used in this thesis is VASP, which is an acronym of Vienna Ab-initio Simulation Program.[140, 141] It is a commercial software package arising from a suite of programs developed by the Computational Materials Physics group at University of Vienna. This code accomplishes the ab-initio calculations by using pseudopotentials and a plane wave basis set. The interaction between ions and electrons is expressed by using ultrasoft Vanderbilt pseudopotentials and the projector augmented wave method. VASP has been applied to a wide range of material science problems, such as heterogeneous catalysis, surface structure and phase transition. More information about this code can be found from its homepage http://www.vasp.at/.

3.2.3.2. The constrained minimisation technique

In this thesis a method called constrained minimisation is used to find the geometries at the transition states, which the method is illustrated in figure 3-2. Basically, the distance between the targeted atoms is set within a typical transition state range. Then the optimisation of the geometry at the rest degrees of freedom begins with fixing the set distance. The transition state is identified when the energy reaches the maximum along the

reaction coordinate, but a minimum with respect to the rest degrees of freedom, and the forces on the atoms get vanished. Finally, the transition states are checked for possession of only one imaginary eigenvalue by employing the vibrational frequency analysis.

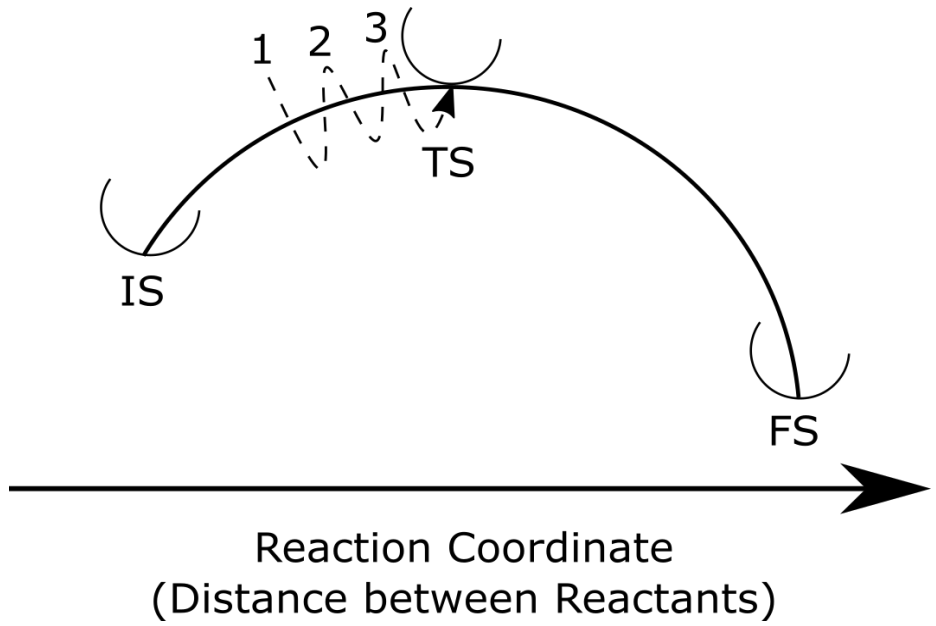

Figure 3-2 Illustration of the procedure to find the transition state using the constrained minimisation technique

In Figure 3-2, the bold solid line is the lowest energy pathway from the initial state to the final state, with the transition state sits on the top along the reaction coordinate. The dotted line represents the optimisation procedure.

The procedure of the technique can be described as follows. At the beginning, we input a guessed structure of the transition state as point 1 in figure 3-2, with the distance between the targeted atoms is fixed at a set distance. The constrained optimisation is then performed by fixing the set distance between the targeted atoms, and relaxing all the rest degrees of

freedom simultaneously, this process stops at the position when the structure is optimised to stay on the lowest energy reaction pathway. After the first optimisation, the constrained distance is changed based on the results obtained by the program, which promotes the structure to move towards the transition state. With the further adjustment of the constrained distance, the structure is changed which presents the total energy reached the point 2. Then the constrained technique optimise the structure to have an energy on the pathway again. By repeating the optimisations, the transition state is found eventually.

3.2.3.3. Surface modelling

The reactions analysed in this thesis occured on the solid surfaces of transition metals and their combinations. In order to obtain accurate calculation results, constructing the surface properly is of great importance. One key feature of the model is the lattice constant of the material, it is optimised by relaxing the unit cell with the fractional coordinates of the atoms remain fixed, to ensure that no strain exists in the lattice due to the attractive and repulsive forces between the atoms. The optimised values of lattice constant are then compared with the experimental values of the bulk materials to guarantee the model is reasonably accurate to represent the materials in the following calculations. Then the specific crystal face is obtained by cleaving the bulk material in a particular direction. For example, to get the most stable flat surface of Pt, the (111) direction is cleaved for representation.

3.2.3.4. Chemisorption energies

The chemisorption energy is a label to describe the relative stability of adsorbates at different sites on the surface, which is defined in the thesis as:

$$E_{ads} = E_{A+surface} - \left(E_A + E_{surface}\right)$$ Equation 3-37

where $E_{A+surface}$ is the total energy when species A is adsorbed on the surface, E_A and $E_{surface}$ are the total energies of the species A in the gas phase and the clean surface respectively. By using this definition, it is worth mentioning that a negative chemisorption energy means the adsorption is an exothermic process. The gaseous phase energy of the adsorbed molecules can be obtained by placing the species in a suitable size unit cell that is repeated infinitely in three dimensions. Additionally, it is necessary to state that the total energies calculated are at zero kelvin (0 K), hence it requires further corrections to account for specific temperatures.

3.2.3.5. Free energy corrections

The energy values obtained from VASP calculations are the total energies at zero kelvin temperature, which requires a conversion into free energy for reactions at specific temperatures. For surface reactions, statistical thermodynamics is a common way to correct the total energy into free energy, which is composed of three sections, the zero-point energy, internal energy, and the entropy energy. Basically, the vibrational mode is emphasised according to the frustrated translational and rotational modes based on harmonic oscillation approximation.[142-144] However, this method is limited to a molecule adsorbed on the surface. While simulations using Gaussian09 software are employed to achieve the free energy correction in the gas phase.[145, 146]

The standard molar Gibbs free energy for each surface elementary reaction state is calculated as:

$$G^\circ = E + ZPE + U^\circ - TS^\circ \quad \text{Equation 3-38}$$

where E is the total energy obtained at 0K from DFT calculation; ZPE, U°, S° are the corrections from zero point energy, internal energy and entropy respectively.

For surface reactions, only vibration modes were taken into account. All the vibrational frequencies were calculated based on the harmonic oscillators approximation in Hz.[144] The zero point energy correction is calculated as following expression:

$$ZPE = \sum_i \frac{hv}{2} \quad \text{Equation 3-39}$$

where h is Planck constant, v is the vibrational frequencies.

While in the gas phase, the molar Gibbs free energy correction can be expressed as:

$$G(T,p) = G^\circ(0K,p^\circ) + \Delta G(T,p^\circ) + RTln\frac{p}{p^\circ} \quad \text{Equation 3-40}$$

where $G^\circ(0K,p^\circ)$ is the molar Gibbs free energy at standard temperature (0K) and standard pressure (1 bar), which equals to the zero point energy corrected total energy of an isolated molecule($E + ZPE$). $\Delta G(T,p^\circ)$ is the thermal correction term of molar Gibbs free energy respect to the standard temperature, and $RTln\frac{p}{p^\circ}$ is the pressure correction term respect to the standard pressure.

Which the thermal correction term $\Delta G(T,p^\circ)$ can be further broken into:

$$\Delta G(T,p^\circ) = [H(T,p^\circ) - H(0K,p^\circ)] - TS(T,p^\circ) \quad \text{Equation 3-41}$$

where $H(T,p^\circ)$ is the molar enthalpy at specific temperature, $H(0K,p^\circ)$ is the molar enthalpy at standard temperature, and $S(T,p^\circ)$ is the molar entropy at specific temperature respectively.

3.2.3.6. Van der Waals Forces

Van der Waals force (vdw) is used to define the intermolecular interactions between the molecules, which is composed of instantaneous dipole-induced dipole force (also known as London dispersion force) and permanent dipole-dipole force.

The instantaneous dipole-induced dipole force is generated by the electrons moving to an end of the molecule to present a δ^- charge, which the other end of the molecule is short of electrons to present a δ^+ charge. This temporary polarity created can induce the polarity of the adjacent non-polar molecule, due to the δ^- attracts the δ^+, which can hold a huge number of molecules together. The strength of the force increases as the number of electrons in the molecule increases, which can be reflected on the comparisons between the boiling points of noble gases. The permanent dipole-dipole force also behaves in a similar way except the polarity of the molecule is generated constantly.

While in the computational section, vdw is incorporated by applying the D3 correction method of Grimme et al,[147] with the following expression is used:

$$E_{disp} = -\frac{1}{2}\sum_{i=1}^{N_{at}}\sum_{j=1}^{N_{at}}\sum_{L}{}' \left(f_{d,6}(r_{ij,L})\frac{C_{6ij}}{r_{ij,L}^{6}} + f_{d,8}(r_{ij,L})\frac{C_{8ij}}{r_{ij,L}^{8}}\right) \qquad \text{Equation 3-42}$$

where the dispersion coefficients C_{6ij} are depending on the geometry, as they are adjusted on the basis of local geometry (coordination number) around atoms i and j. And the Beche-Jonson (BJ) damping is applied as:

$$f_{d,n}(r_{ij}) = \frac{s_n r_{ij}^n}{r_{ij}^n + (a_1 R_{0ij} + a_2)^n} \qquad \text{Equation 3-43}$$

with $s_6 = 1$ and a_1, a_2, and s_8 are the adjustable parameters, this method is invoked in VASP with code of IVDW=12 in INCAR file.

3.2.3.7. On-site Coulomb interaction: DFT+U

The fundamental idea of DFT+U is to describe the strong on-site Coulomb interaction of localised d and f electrons, which is not correctly presented by LDA or GGA. The strength of the on-site interactions are usually expressed by parameters U (on site Coulomb) and J (on site exchange). This correction is proposed by Dudarev et al. in DFT calculations,[148] where only a single effective parameter of $U_{eff} = U - J$ accounts for the Coulomb interaction. This correction is important for calculations of metal oxides, which is applied in the calculations of the cobalt oxide chapter.

3.2.3.8. Assumptions within the calculations

In order to reach a good balance between the computational resource consumption and molecular understanding of the reaction system, there were some assumptions made throughout the calculations:

(1) The supercell model was created in the smallest scale. With the target of understanding the intrinsic activity of catalyst, the coverage effect was not considered.

(2) All of the energy corrections were based on optimised structures obtained from VASP calculations, which were calculated at 0 K temperature condition. Hence the geometrical change was assumed to be neglected upon the temperature difference.

(3) All the reactants were referenced to the gas phase pressure of 1 bar, except the hydrogen pressure which was stated in the relative experimental work.

(4) All the resultant products were easily desorbed from the catalytic surface, according to the low values of their adsorption energies.

Chapter 4 DFT Study of Direct Furfural Conversion to 2-Methylfuran on Ru/Co_3O_4 Surface

4.1. Introduction

In 2014, Wang et al. achieved furfural conversion on Ru/Co_3O_4 in THF solvent at 170 ^oC, and the final products were composed of 92.5% 2-methylfuran and 6.7% furfuryl alcohol.[149] It showed the possibility to avoid the undesired decarbonylation reactions for furfural conversion. Hence, in order to reveal the mystery, the latest PBE-D3-GGA+U method was used to investigate the mechanisms of furfural upgrading in this work. To the best of our knowledge, this was the first theoretical study presenting mechanisms of furfural conversion on metal-oxide complexes. Based on the free energy data, a favoured reaction pathway for 2-methylfuran production via hydrodeoxygenation of furfural was identified, with an oxygen vacancy was necessary to be created.

4.2. Computational methods

All calculations reported here were carried out by using plane-wave-based DFT method with application of Vienna ab initio simulation package (VASP).[140, 141] The PBE-D3 correction method was employed in order to include van der Waals (vdw) interactions.[132, 147] Also, to recover the 3d electron correlations, the Coulomb and exchange interactions were considered, and hence the GGA+U method of Dudarev was applied.[148] As the Co_3O_4 single crystals exposes naturally the (110) and (111) surfaces,[150] these surfaces have been studied by Auger electron spectroscopy, low-energy electron diffraction, X-ray photoelectron spectroscopy, and scanning tunneling microscopy.[151-154] Li et al.,[155] have

addressed that at oxygen-poor condition, (111) is relatively more stable. However, it was reported that the (110) surface presents a much greater catalytic activity.[156-160] Also, as the key step of furfural hydrogenolysis to 2-methylfuran is the aliphatic carbon-oxygen bond cleavage, this bond is required to be activated via both atoms bonding with surface metal atoms,[117] which is the cobalt in Co_3O_4 that is not present on the (111) surface. Due to these factors, we chose the (110) surface instead. U_{eff} = U-J = 3.0 eV was chosen for the Co_3O_4(110), which is an optimum value for catalysis-related applications.[161, 162] The project-augmented wave (PAW) method was used to represent the core-valence interaction.[163, 164] For the calculations of total energy, a cutoff energy of 400 eV was set for plane wave basis sets to expand the valence electronic states. Transition states (TS) were determined by a constrained optimisation method[159, 165-168] in which TSs are verified until (i) all forces on atoms are vanished and (ii) the total energy reaches a maximum along the reaction coordinate but a minimum with respect to the rest of the degree of freedom. The TS were checked by vibrational calculations. After the lattice parameter optimisation, a unit cell of bulk Co_3O_4 which is composed of 32 O and 24 Co was chosen to construct the (110) surface.[169] (a = 7.99 Å, experimental value is 8.05 Å.[170]) In order to get better computational efficiency, p(1 x ½) of the slab was considered in the calculations. There are two types of surface terminations in the (110) slab model; type A is composed of two Co^{3+} at the octahedral sites and two Co^{2+} at tetrahedral sites, and four threefold coordinated O^{2-} anions; type B is composed of two Co^{3+} cations at octahedral sites, two twofold and two threefold coordinated O^{2-} anions. In Figure S2 of the supporting information provided by Wang et al.,[149] the XRD pattern of the Ru/Co_3O_4 catalyst showed a decreased ratio of oxygen to cobalt, which indicated that the oxygen vacancy was generated during the

reaction. Due to the importance of oxygen vacancy requirements in the reactions, the type B surface termination was used, as both two and threefold oxygens could be examined and compared in the calculations. The Co_3O_4(110) surfaces were modelled as a p(1 x ½) periodic slab with 6 atomic layers. The Ru(0001) surface was modelled with a 4 x 4 unit cell composed of 4 atomic layers. As Wang et al. also stated that the ruthenium was in a highly dispersed pattern,[149] the Ru/Co_3O_4 surface was modelled based on the Co_3O_4(110) surface with further addition of 1 line Ru atoms of Ru(0001) surface situated on the Co_3O_4 surface between the unreacted Co^{3+} cation and twofold coordinated O^{2-} anions. A model with an extension of Ru atoms on the surface was also tested. The bottom 2 layers were frozen. The vacuum between the slabs was set at 15 Å to minimise the effect of the slab. Brillouin zone was sampled with a 2 x 2 x 1 k-point grid. Surface relaxation was performed until all forces were lower than 0.05 eV/Å. To obtain the free energy of species, some standard formulae of statistical mechanics were used to calculate the thermodynamic correction including zero point energy, thermal energy, and entropy derived from partition functions.[171, 172] As the DFT calculated energies are the total energies at T = 0 K, these energies were converted into Gibbs free energies according to $G = E + E_{ZPE} + U - TS$ (ZPE = zero point energy) at 443 K. All the reaction energies and activation barriers were reported as the Gibbs free energy calculated at reaction condition of 443 K with the hydrogen pressure of 10 bar, which was stated in the experiment,[149] while other components were treated at 1 bar pressure. The adsorption energy (ΔG_{ad}) was defined as

$$\Delta G_{ad} = G_{adsorbate+slab} - G_{adsorbate} - G_{slab}$$

where G_{slab}, $G_{adsorbate}$, and $G_{adsorbate+slab}$ are the free energies of slab, adsorbate in the gas phase, and adsorbate adsorbed on the slab, respectively. Vibrational analysis was carried

out to ensure the transition states had one imaginary frequency only along the reaction coordinate, all of the lowest-energy conformations and intermediates were confirmed to have all real frequencies.

4.3. Results

4.3.1. Vacancy formation on Co_3O_4 and Ru/Co_3O_4 surfaces

From the analysis of the Co_3O_4(110) surface, the adsorption energy of furfural was weak which was only -0.18 eV via the carbonyl oxygen in a η^1(O) pattern on the cobalt atom. In order to obtain better furfural adsorption, an oxygen vacancy is required to be created on the surface. Due to the reaction circumstances, the only way to create the vacancy is to remove the surface O^{2-} anions in the form of water: There are two options, the twofold and threefold O^{2-} anions. Our calculations showed that the twofold O^{2-} vacancy was extremely difficult to be generated with the reaction energy of the hydroxyl coupling was 2.90 eV, and thus only threefold O^{2-} vacancy is illustrated in figure 4-1. Due to the easiness of H_2 activation in the hydrogenation catalysis, H was used instead of $1/2H_2$ for simplicity.

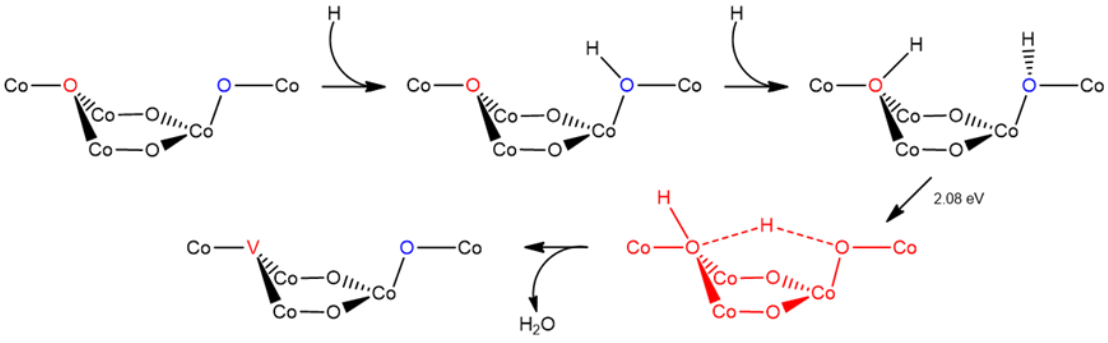

Figure 4-1 a) Schematic illustration of vacancy formation via hydrogenations of threefold oxygen on the Co_3O_4(110) surface

Where twofold oxygen is marked in blue, threefold oxygen, vacancy, and transition state are marked in red.

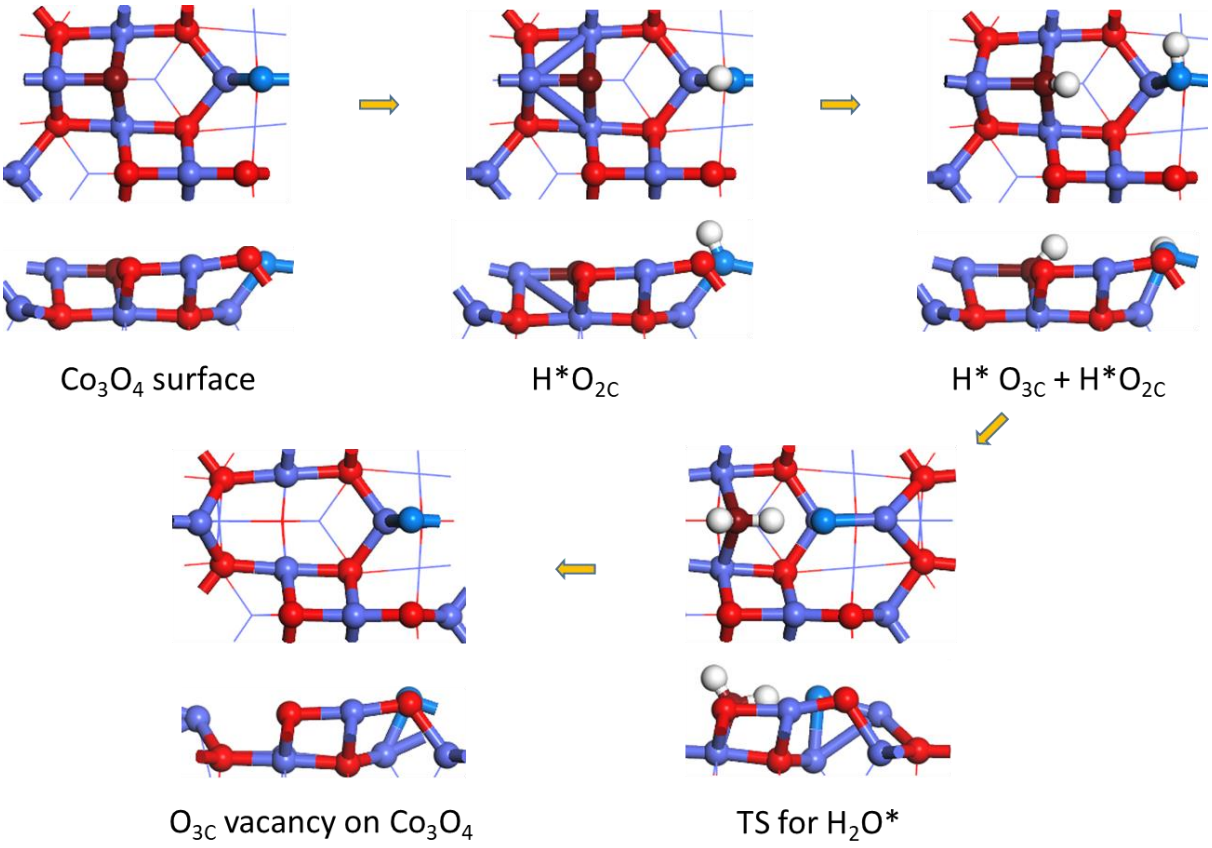

Figure 4-1 b) Mechanism of vacancy formation via hydrogenations of threefold oxygen on the $Co_3O_4(110)$ surface

Where cobalt atoms, threefold oxygen, twofold oxygen, hydrogens, and other oxygens are marked in light purple, dark red, light blue, white, and red respectively.

The first hydrogen adsorbed on the twofold O^{2-} anion with an adsorption energy of 0.78 eV, and the second hydrogen adsorbed on the threefold O^{2-} anion with a further adsorption energy of 0.12 eV. The hydrogen binding to the twofold oxygen was transferred to the

threefold oxygen in the next step, and at the transition state, the new H-O bond formed at a length of 1.42 Å. A water molecule was generated subsequently, and left a vacancy for furfural to adsorb on the surface.

Calculations for the vacancy formation were also carried out on Ru/Co_3O_4 surface, the results of which is shown in figure 4-2. The first hydrogen adsorbed at the bridge site of two Ru atoms with an adsorption energy of 0.45 eV, and this hydrogen was then transferred to the threefold O^{2-} anion. In the TS, the H-O distance was 1.57 Å, and the new H-O bond formed at a length of 0.99 Å at the final state. After the first hydrogen transfer, the second hydrogen was co-adsorbed at the similar position as the first hydrogen on the Ru bridge site with an adsorption energy of 0.83 eV. Afterwards, the successive hydrogenation occurred with a H-O distance of 1.39 Å in the TS, and finally the second new H-O bond formed at a length of 1.01 Å as the vacancy generated via water formation.

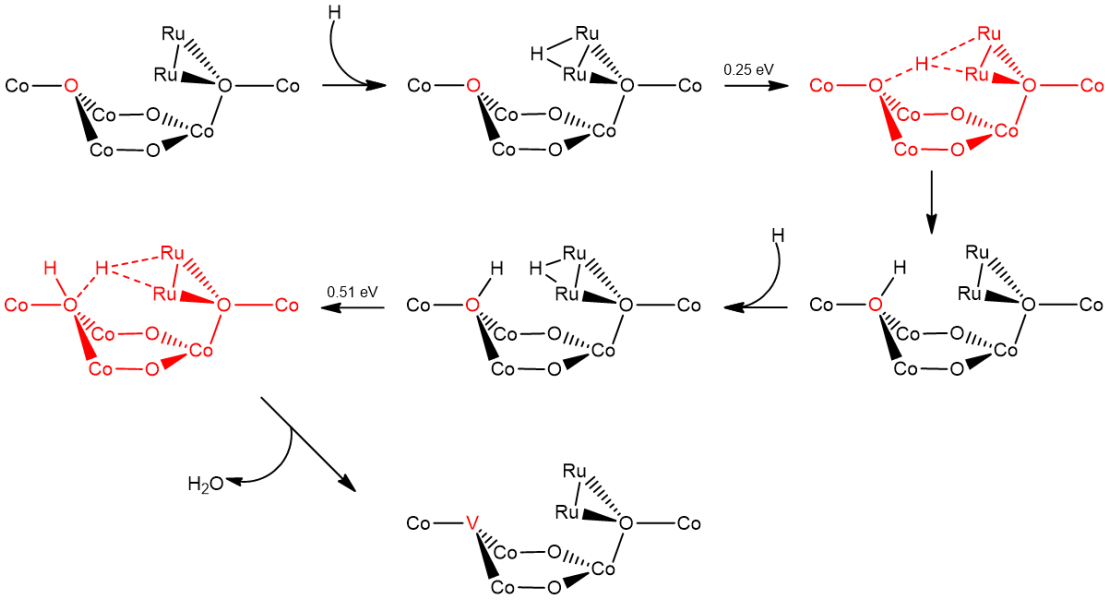

Figure 4-2 a) Schematic illustration of vacancy formation via hydrogenations of threefold oxygen on Ru/Co_3O_4 surface

Where threefold oxygen, vacancy, and transition states are marked in red.

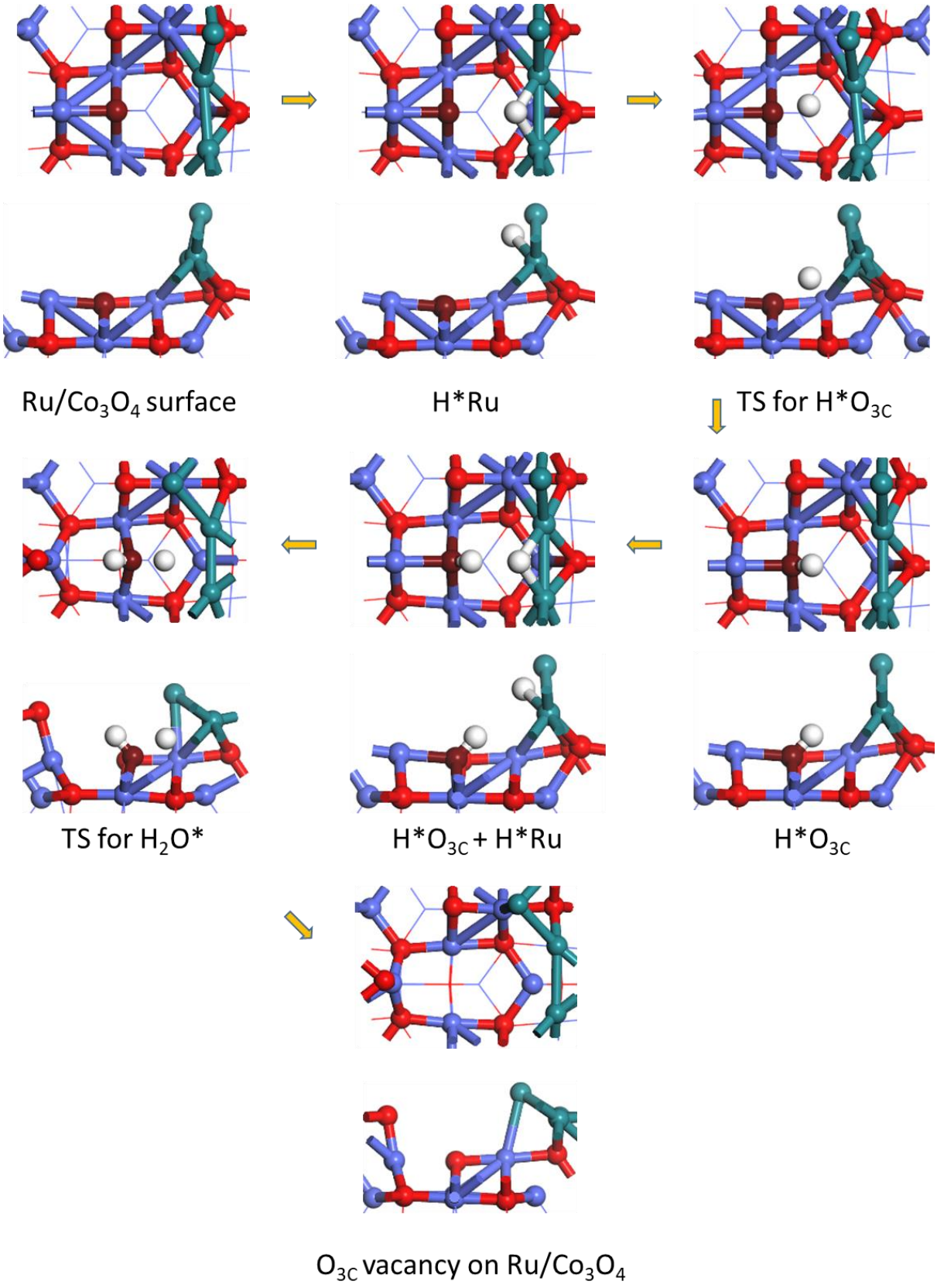
Ru/Co3O4 surface
H*Ru
TS for H*O3C
H*O3C
H*O3C + H*Ru
TS for H2O*
O3C vacancy on Ru/Co3O4

Figure 4-2 b) Mechanism of vacancy formation via hydrogenations of threefold oxygen on Ru/Co_3O_4 surface

Where ruthenium atoms, cobalt atoms, threefold oxygen, hydrogens, and other oxygens are marked in green, light purple, dark red, white, and red respectively.

4.3.2. Reaction pathways of 2-methylfuran generation

During the production of 2-methylfuran on the Ru/Co_3O_4 surface, there were two pathways totally. One was that the furfural could be hydrogenated to furfuryl alcohol on the ruthenium surface, and then converted to 2-methylfuran on the Ru/Co_3O_4 surface, which was suggested with the experiments of Wang et al.[149] The other was that the furfural could be directly converted into 2-methylfuran on the Ru/Co_3O_4 surface.

4.3.2.1. Furfuryl alcohol production via hydrogenations of furfural on Ru(0001)

The reaction pathway involved in furfuryl alcohol (FA) production is illustrated first, with the FA generation via furfural hydrogenation was computed on the flat Ru(0001) surface which is shown in figure 4-3. Due to the furfural upgrading calculations have been done by Arghya et al.,[113] only the partial aliphatic hydrogenation of furfural to furfuryl alcohol was repeated to make the following results consistent. The pathways could be split to the order of hydrogenation, either via an alkoxide intermediate or via a hydroxyalkyl species.

In the furfural adsorption configuration, all the ring carbon atoms were close to the top position of the Ru atoms; however, only the alpha carbon atoms bonded to the ruthenium surface. The side carbonyl carbon was located at a hcp follow site, while the carbonyl

oxygen was directly bonding to the Ru atom at a top position. The adsorption energy of furfural was 1.37 eV.

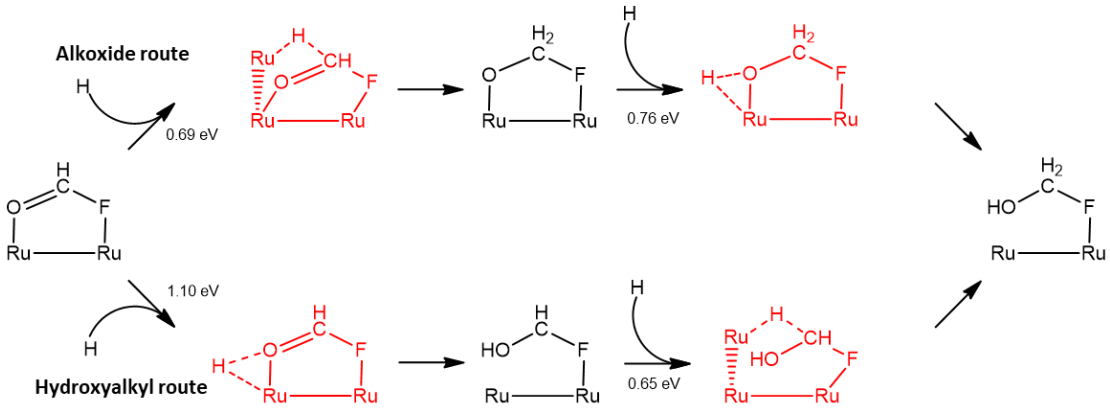

Figure 4-3 Schematic illustration of reaction pathways of furfural conversion to furfuryl alcohol on Ru(0001) surface

Where the transition states are marked in red. F stands for the furyl ring.

4.3.2.1.1. The alkoxide route

The first hydrogenation at carbonyl carbon started by the hydrogen attacked from the top site of the Ru atom with a H-C distance of 1.60 Å in the TS, and the aldehyde hydrogen moved further away from the top site of the same Ru atom. The carbonyl C-O bond increased from 1.33 Å to 1.35 Å and the aromatic C-aliphatic C bond length extended from 1.44 Å to 1.49 Å. The alkoxide intermediate was generated at the FS, at which the new C-H bond had a length of 1.11 Å with the C moved further away from the surface. Contrast to the IS, the aliphatic oxygen-Ru bond length decreased from 2.11 Å to 1.99 Å.

The alkoxide intermediate was further attacked by a hydrogen atom from a bridge site. In the TS, the H-O distance was 1.43 Å, while the O-Ru bond length stretched from 1.99 Å to 2.13 Å, and the C-O distance extended slightly from 1.41 Å to 1.42 Å. With the furfuryl alcohol was generated subsequently in the FS, the new H-O bond formed at a length of 0.98 Å.

4.3.2.1.2. The hydroxyalkyl route

The hydroxyalkyl route started with the hydrogen approached from the bridge site to the carbonyl oxygen. In the TS, the H-O distance was 1.33 Å, carbonyl bond length was increased to 1.37 Å, and there was no bonding between the aliphatic oxygen and Ru surface anymore. As the hydroxyalkyl was generated, the new H-O bond formed at a distance of 0.99 Å, the carbonyl bond length further extended to 1.43 Å, and the oxygen was further away from Ru atom with the distance increased to 2.41 Å.

When the second hydrogen attacked the aliphatic carbon from a top site of the Ru atom, the H-C distance was 1.47 Å, and the C-O bond was also increased to 1.44 Å, while the aromatic carbon-aliphatic carbon bond length stretched from 1.44 Å to 1.49 Å in the TS. The geometry details of furfuryl alcohol adsorption was stated at the end of pathway 1, with the new C-H bond formed at a distance of 1.10 Å, and the aromatic C-aliphatic C bond length was increased to 1.49 Å.

4.3.2.2. 2-methylfuran generation via hydrodeoxygenation of furfuryl alcohol on Ru/Co_3O_4

The 2-methylfuran generation pathways are shown in figure 4-4. The furfuryl alcohol adsorbed at the vacancy of Ru/Co_3O_4 via its carbonyl O at a η^1(O) geometry and one of its aromatic carbon to one Ru atom, with an adsorption energy of 1.61 eV. The furfuryl alcohol was then deprotonated at its alcohol group, and the H-O bond length stretched from 1.03 Å at the IS to 1.33 Å at the TS. The resultant furyl-CH_2O intermediate adsorbed in a similar pattern to that of furfuryl alcohol, and the released proton adsorbed with an energy of 0.21 eV at the adjacent Ru-Ru bridge site. The proton was further desorbed to give space for the following C-O cleavage of the furyl-CH_2O intermediate, and the C-O bond increased from 1.44 Å at the IS to 2.13 Å in the TS, which the resultant intermediate CH_2 group adsorbed on the top site of adjacent Ru atom in the FS. The second hydrogenation was subsequently achieved via a hydrogen atom adsorbed at the recovered threefold O^{2-} anion in the IS with an adsorption energy of 0.84 eV. Contrast to the IS, the H-O bond length increased from 0.99 Å to 1.28 Å and the H-C distance was 1.38 Å in the TS. Finally, the 2-methylfuran was produced and the surface was regenerated.

4.3.2.3. 2-methylfuran generation via hydrodeoxygenation of furfural on Ru/Co_3O_4

At the beginning, the furfural adsorbed vertically on the surface at a η^2(C-O) geometry and one of its aromatic carbon to one Ru atom, with an adsorption energy of 1.78 eV. Then the first hydrogen approached from a Ru bridge site to the carbonyl carbon with an adsorption energy of 0.61 eV, in the TS the H-C distance was 1.43 Å, and the alkoxide was generated

at the FS with the new H-C bond formed at a distance of 1.10 Å. The C-O bond was cleaved afterwards, and the rest of steps were the same as illustrated in the section 4.3.2.2.

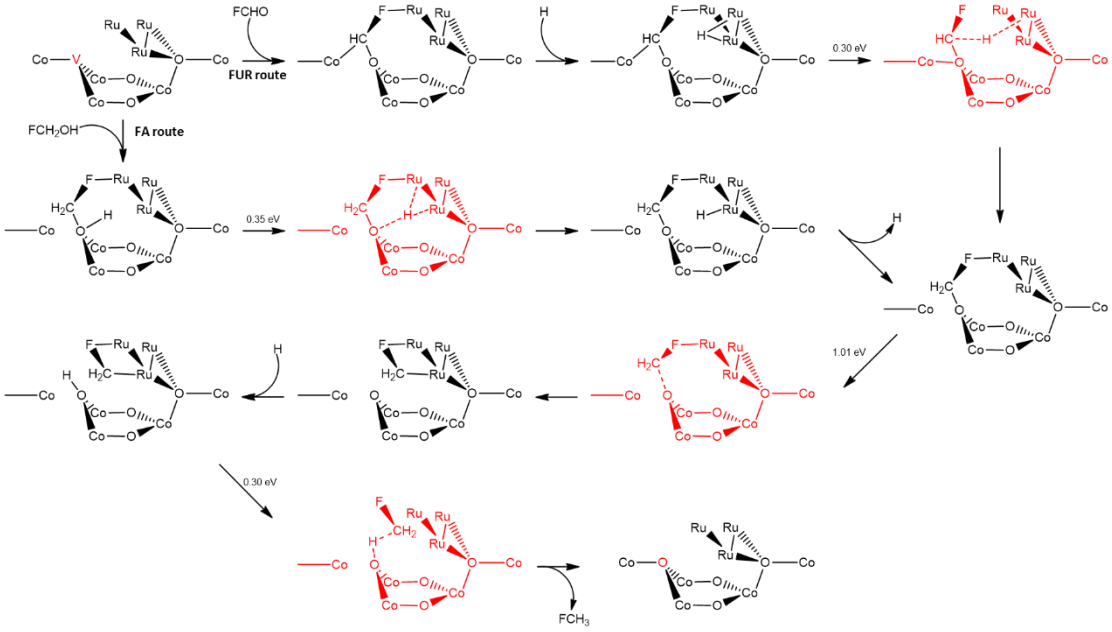

Figure 4-4 a) Schematic illustration of 2-methylfuran formations via hydrodeoxygenations of furfural and furfuryl alcohol on the Ru/Co_3O_4 surface

Where threefold oxygen, vacancy, and transition states are marked in red. F stands for furyl ring.

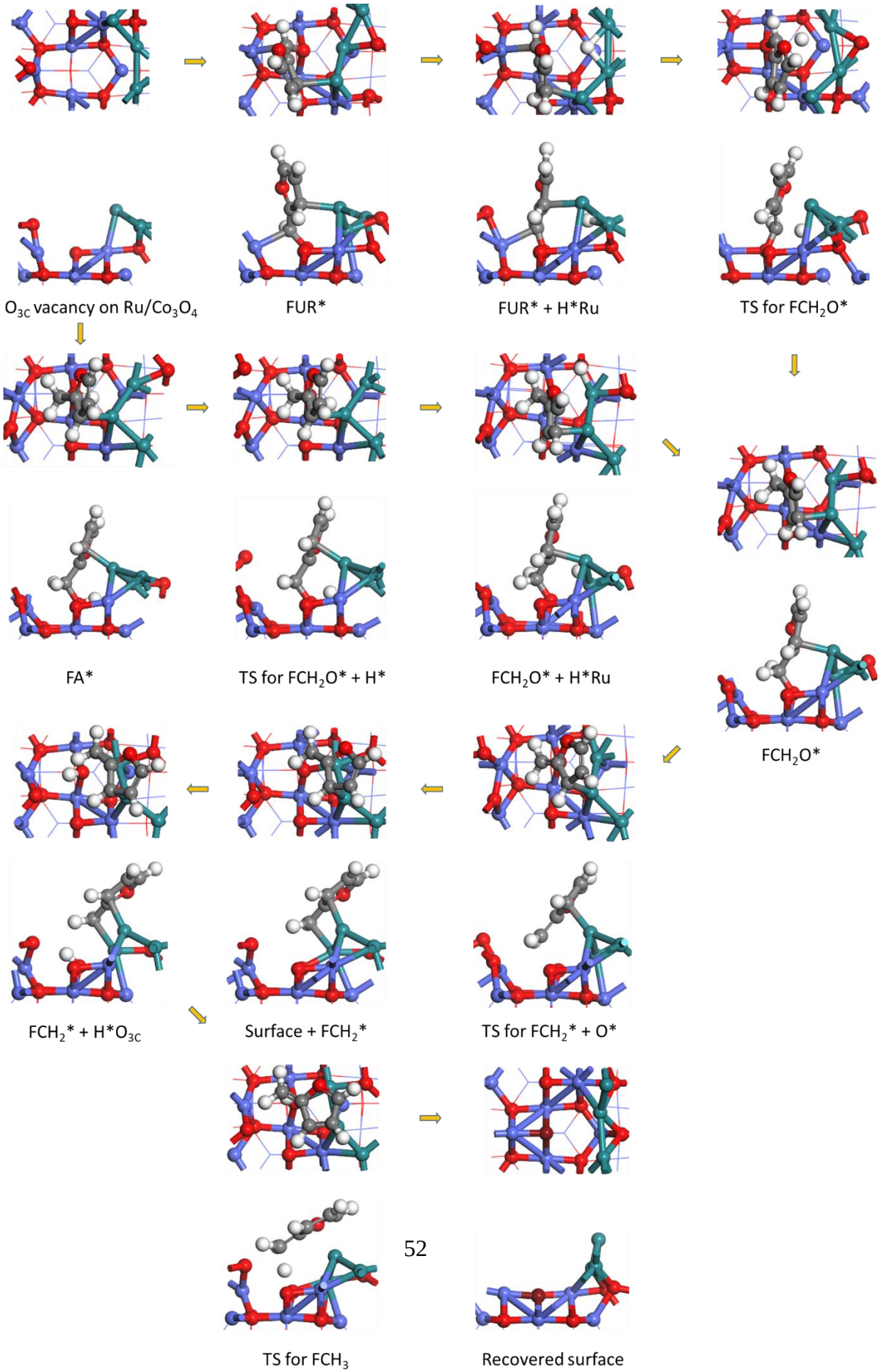
O_{3C} vacancy on Ru/Co_3O_4
FUR*
FUR* + H*Ru
TS for FCH_2O*
FCH_2O*
FCH_2O* + H*Ru
TS for FCH_2O* + H*
FA*
FCH_2* + H*O_{3C}
Surface + FCH_2*
TS for FCH_2* + O*
TS for FCH_3
Recovered surface

Figure 4-4 b) Mechanism of 2-methylfuran formations via hydrodeoxygenations of furfural and furfuryl alcohol on the Ru/Co_3O_4 surface

Where ruthenium atoms, cobalt atoms, carbons, hydrogens, oxygens, and the recovered threefold oxygen are marked in green, light purple, grey, white, red, and dark red respectively.

4.4. Discussions

4.4.1. Vacancy generation tendency of Co_3O_4 and Ru/Co_3O_4 via hydrogenations

From the reaction profile shown in figure 4-5, the reaction barrier of proton transfer from twofold oxygen to threefold oxygen was 2.08 eV, suggested that the mobility of proton on the Co_3O_4 surface was low and unfavourable to generate an oxygen vacancy in the form of water by itself. Also, the energy profile showed a general trend of decreasing stability, indicated that the reactions may not readily take place.

After the addition of ruthenium to the Co_3O_4 surface, the whole reaction mechanism was switched to successive hydrogen transfer from Ru to the threefold oxygen. The energy profile in figure 4-5 showed a general trend of increasing stability along the reaction coordinate without high barriers (0.25 and 0.51 eV, respectively). Contrast to the trend from the Co_3O_4 surface, possession of ruthenium made the reaction both kinetically and thermodynamically favoured which is represented by the blue pathway in figure 4-5. From the barrier data, it was clear that the ruthenium had a function of facilitating hydrogenation in this system.

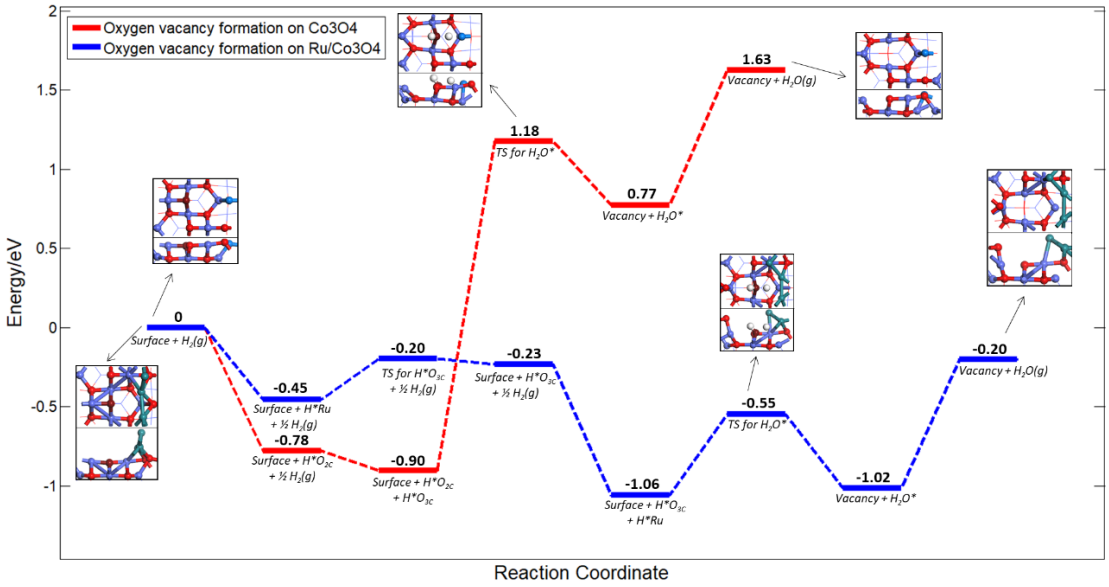

Figure 4-5 Reaction profiles of oxygen vacancy generations on the Co_3O_4 and Ru/Co_3O_4 surfaces

Where ruthenium atoms, cobalt atoms, threefold oxygen, twofold oxygen, hydrogens, and other oxygens are marked in green, light purple, dark red, light blue, white, and red respectively.

4.4.2. Competitions of the 2-methylfuran formation pathways

The experimental data of Wang et al. only showed two products with major 2-methylfuran and minor furfuryl alcohol, respectively,[149] and hence 2-methylfuran could be generated from furfural and furfuryl alcohol in both ways. The furfuryl alcohol formation was achieved on the flat Ru(0001) surface, with the reaction profile is shown in figure 4-6. The successive hydrogenation barriers were 0.69 eV and 0.76 eV via alkoxide intermediate route, and 1.10 eV and 0.65 eV via hydroxyalkyl intermediate route, respectively. Therefore, the alkoxide route was favoured kinetically for the furfuryl alcohol production

which is represented by the red pathway in figure 4-6. It is also worth noting that the adsorption energy of furfuryl alcohol on the ruthenium surface was 1.22 eV, which is in a considerable scale if furfuryl alcohol is required to desorb for the subsequent reactions.

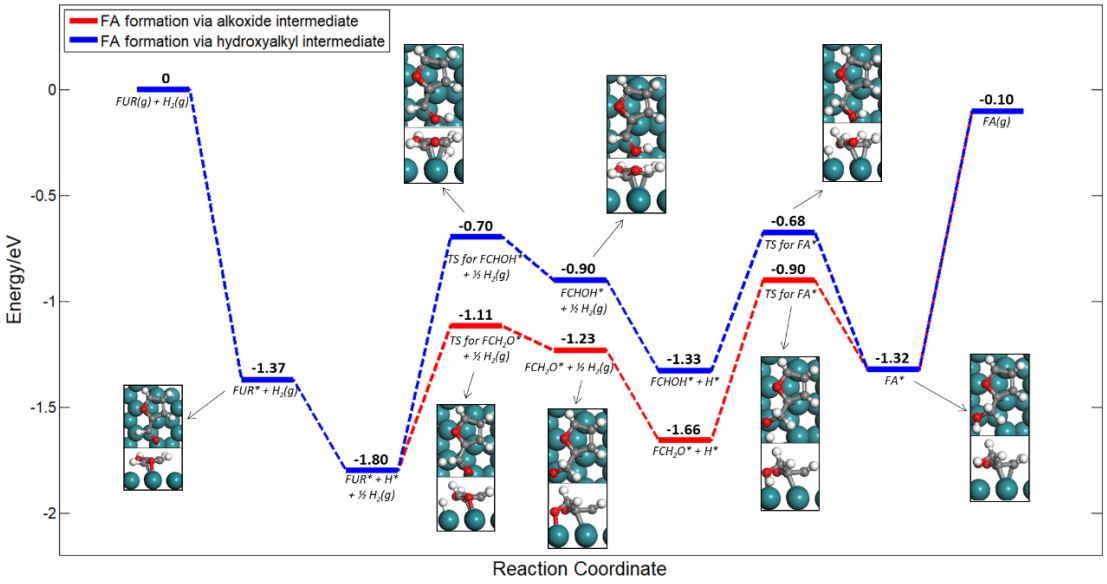

Figure 4-6 Reaction profile of Furfuryl alcohol formations on the Ru(0001) surface

Where ruthenium atoms, carbons, hydrogens, and oxygens are marked in green, grey, white, and red respectively.

The reaction profile of 2-methylfuran formations on Ru/Co_3O_4 is shown in figure 4-7. When the furfuryl alcohol adsorbed at the vacancy, the deprotonation barrier of the alcohol group was 0.35 eV, and the proton release required 0.21 eV, which were both facile. The further common barriers of C-O cleavage and hydrogenation of furyl-CH_2 were 1.01 eV and 0.30 eV, respectively. If the furfural was converted directly into 2-methylfuran on the Ru/Co_3O_4 surface, the only different step to the furfuryl alcohol pathway was the first

alkoxide formation, which needed to overcome a barrier of 0.30 eV. Additionally, the large hydrogenation barrier of the carbonyl oxygen (0.99 eV) showed that the furfuryl alcohol was less likely to be generated on the Ru/Co_3O_4 vacancy. There were a few advantages that the 2-methylfuran was produced directly from furfural on the Ru/Co_3O_4 vacancy: (i) Based on the XRD test result, Wang et al.[149] stated that the Ru atoms were highly dispersed, which means furfuryl alcohol formation was less likely. (ii) If the furfuryl alcohol was generated on Ru(0001) surface, it required an desorption energy of 1.22 eV; then the furfuryl alcohol had to compete with furfural on Ru/Co_3O_4 vacancy with an adsorption energy of 0.17 eV disadvantage. (iii) Furthermore, it was not necessary to produce furfuryl alcohol for further generation of 2-methylfuran. Therefore, the 2-methylfuran was obtained directly from furfural at the Ru/Co_3O_4 vacancy which is represented as the red pathway in figure 4-7, and the furfuryl alcohol was generated in a small amount as a by-product without participating in the production to 2-methylfuran.

There were some papers suggested that the furfuryl alcohol was a key intermediate for 2-methylfuran production. However, furfuryl alcohol could not be produced substantially in the Ru/Co_3O_4 system. In the work of adsorption of furfural and furfuryl alcohol on Pd(111), Medlin et al.,[173] they stated that 2-methylfuran could be generated via hydrogenolysis of furfuryl alcohol. Only the results of the reactants adsorbed on the flat metal surface were reported, which could interact directly with furfural to activate the specific bond to generate furfuryl alcohol. But in our system, the adsorption geometry of furfural was different because the Ru particles were highly dispersed. As Mei et al. stated in DFT furfural conversion on Pt,[110] the particle size could determine the reaction pathway. While in the

furfural conversion to 2-methylfuran on Ru/RuO_x/C, Xu et al.[174] showed that the furfuryl alcohol was generated from furfural via catalytic transfer hydrogenation on lewis acid sites, they required a tertiary alcohol to act as the proton donor. This was absent under the experimental condition of Wang et al.,[149] as hydroxymethylfurfural is a primary alcohol, which could not be stabilised as tertiary alcohols during dehydrogenation.

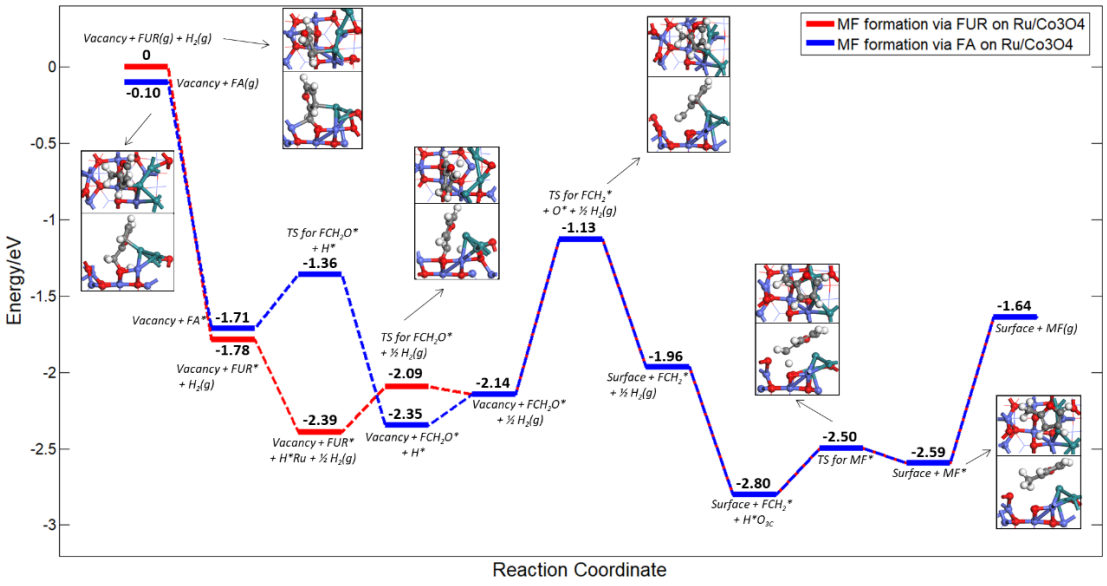

Figure 4-7 Reaction profile of 2-methylfuran formations on the Ru/Co_3O_4 surface

Where ruthenium atoms, cobalt atoms, carbons, hydrogens, and oxygens are marked in green, light purple, grey, white, and red respectively.

4.4.3. Synergistic effects between Ru metal and Co_3O_4 support in furfural conversion

From the computational work of Austin et al.,[175] the hydrodeoxygenation of phenol could be attributed to the acid-base interaction of the TiO_2 support with water molecule and

hydroxyl intermediate. In their work, water had a profound effect on the direct cleavage of C-O bond of phenol, which generated hydroxyl intermediate to achieve the heterolytic dissociation of hydrogen molecule for the following hydrogenation of phenyl intermediate on ruthenium. However, water was absent at the Ru/Co_3O_4 experimental condition,[149] and hence this kind of acid-base interaction was not likely to exist.

Based on the charge analysis of the reaction structures of furfural conversion on Ru/Co_3O_4 which is shown in figure 4-8, the initial adsorption of furfural on the Ru/Co_3O_4 vacancy was stabilised by the Ru atom donating electron density to one ring-carbon, and the cobalt atoms bonded to the carbonyl carbon and oxygen, respectively.

In the first step of hydrogenation of furfural, the adsorbed hydrogen was activated by the Ru atoms donating electron density, which promoted the nucleophilic attack to the carbonyl carbon of the furfural. During the C-O bond breaking, this step was facilitated by the Ru/Co_3O_4 coordination effect which stabilised the oxygen by the ruthenium and cobalt atoms together, with the produced FCH_2 intermediate adsorbed on Ru atoms. Finally, the hydrogen transferred from the recovered oxygen on the surface to the unsaturated carbon generated the 2-methylfuran. Overall, the ruthenium supplied ring stabilisation and hydrogen activation before the C-O bond breaking, while it operated cooperatively with cobalt to facilitate the C-O bond cleavage, and finally promoted the formation of 2-methylfuran via providing adsorption of FCH_2 intermediate.

To summarise, the oxygen vacancy of Co_3O_4 was created for stable adsorption of furfural on the surface, which was achieved with the addition of Ru particles. Then the surface cobalt stabilised the carbonyl group of furfural which was adsorbed at the oxygen vacancy, and the ruthenium particles facilitated the hydrogenation of the carbonyl carbon, followed by the C-O cleavage which was promoted by the oxygen stabilisation from cobalt, and the FCH_2 species was finally saturated to generate 2-MF. These results were consistent with experimental suggestions that the Ru particles were beneficial for H_2 activation and hydrogenation reactions, and CoO_x species played a key role in the cleavage of C-O bond. [176, 177]

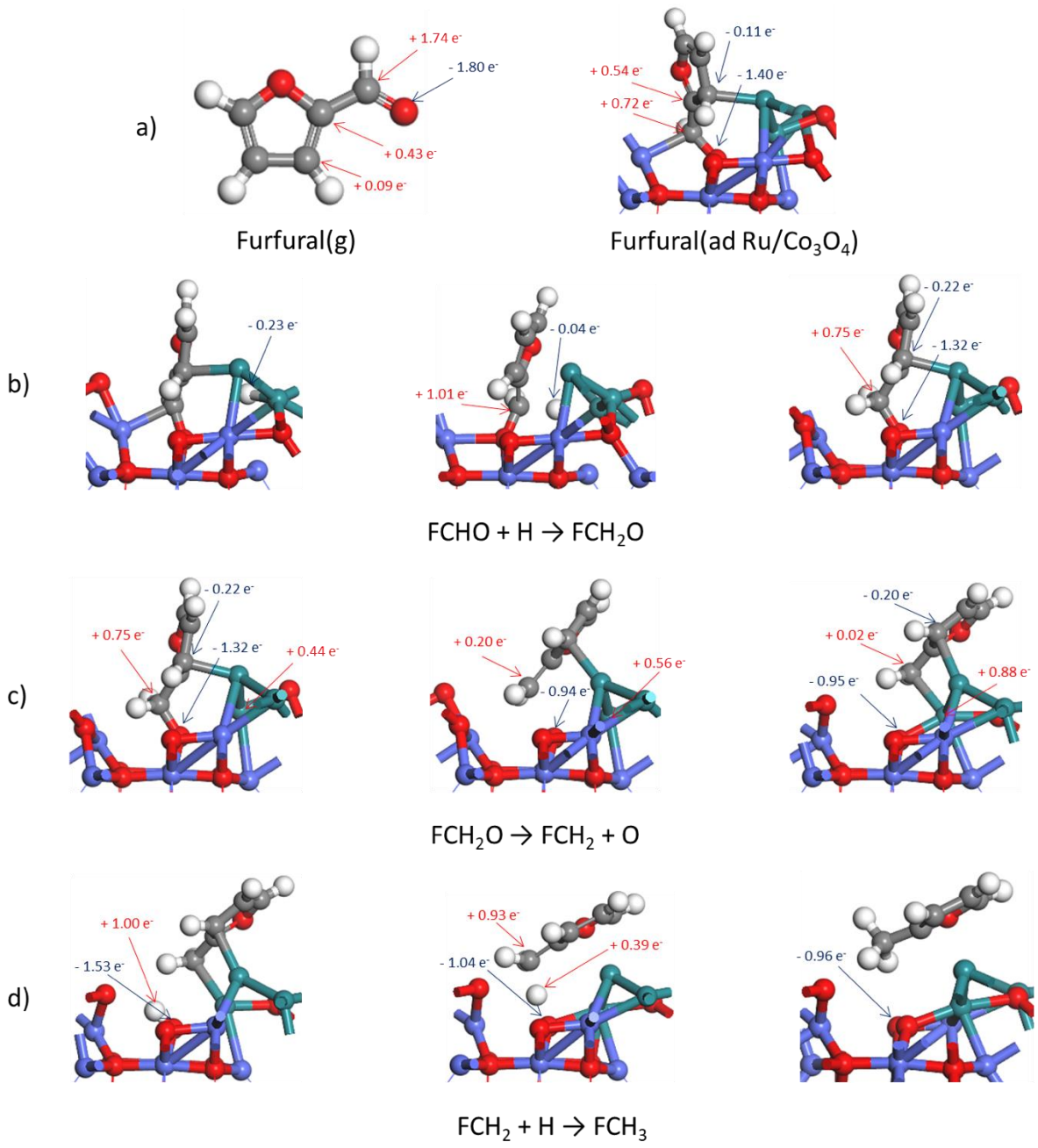

Figure 4-8 Charge analysis of the structures

The positive and negative charge are marked in red and blue relatively. Which a) for the furfural in gas phase and Ru/Co_3O_4 oxygen vacancy adsorbed state respectively; b), c), and

d) are for the key reaction steps of the furfural conversion to 2-methylfuran on Ru/Co_3O_4 threefold oxygen vacancy.

4.4.4. Factors which inhibited the decarbonylation of furfural on Ru/Co_3O_4

In the experimental results of Wang et al.,[149] the most beneficial feature was that the decarbonylation was difficult to achieve, which generated by-product furan and carbon monoxide. We tried to calculate the C-C bond cleavage but failed; the reason could be attributed to the adsorption geometry of furfural on the oxygen vacancy as the C-C bond was far away from the surface in our system. This feature was also found in Cu(111).[115] While the C-C bond could be cleaved when the furfural adsorbed on group X metals and ruthenium,[110, 112, 113] due to the C-C bond was close to the metal surfaces that could be easily accessed.

4.5. Conclusions

Detailed density functional theory calculations of 2-methylfuran formation on Ru/Co_3O_4 at 443 K was computed on PBE-D3-GGA+U functional with following results achieved:

(1) The adsorption of furfural on the Co_3O_4 surface was weak, which showed an oxygen vacancy was required to be generated for the following hydrodeoxygenation reactions, and the reaction barrier was considerably high to be overcome.

(2) Due to the hydrogenation ability of ruthenium metal, the oxygen vacancy via water molecule production was much improved upon ruthenium addition compared to the Co_3O_4-only surface.

(3) The furfuryl alcohol generation on the Ru(0001) surface was computed with both alkoxide and hydroxyalkyl pathways, and it was kinetically favoured to be produced via the alkoxide intermediate formation.

(4) The 2-methylfuran productions via both furfuryl alcohol and furfural were calculated. In the furfuryl alcohol pathway, the alcohol was first adsorbed on the oxygen vacancy, and then the hydrogen of alcohol group was released, followed by C-O bond cleavage and hydrogenation of the successive furyl-CH_2 species. The furfural pathway was similar to the furfuryl alcohol pathway, with the only difference from the first reaction step, which was the hydrogenation on carbonyl carbon of furfural. Overall, the rate-determining step barrier was 1.01 eV from the C-O bond cleavage step. With the consideration of furfuryl alcohol production procedure on the Ru(0001) surface, 2-methylfuran was favoured to be generated via hydrodeoxygenation of furfural directly, which indicated that the furfuryl alcohol detected in the experiment was attributed to the outstanding hydrogenation ability of ruthenium metal.

(5) The decarbonylation pathway was prohibited due to the adsorption geometry of the furfural on Ru/Co_3O_4 oxygen vacancy, because the C-C bond was difficult to be activated.

Chapter 5 DFT Study of Furfural Conversion on Re/Pt Bimetallic Surface: Synergetic Effect on the Promotion of Hydrodeoxygenation

5.1. Introduction

Due to the requirements of hydrogenation and selective hydrogenolysis of furfural, the combination of active hydrogenation metals and oxophilic metals becomes popular to develop new hydrodeoxygenation catalysts. It was shown by Burch et al. that the co-operation between platinum and rhenium worked well on amide hydrodeoxygenation, which showed that Re was capable of activating the carbonyl bond, and Pt was able to reduce the oxygen-related species.[178] Aiming to investigate the synergetic effect of two metals and their individual roles on selective C-O bond breaking, in this work we used PBE-D3 method to investigate the furfural conversion on the Re/Pt bimetallic surface at an experimental temperature of 403 K, which was the temperature performed by Chen et al.[91] To the best of our knowledge, this was the first theoretical study presenting mechanisms of furfural transformation on bimetallic systems.

5.2. Computational methods

All calculations reported here were carried out by using plane-wave-based DFT method with application of Vienna ab initio simulation package(VASP).[140, 141] The PBE-D3 correction method was employed in order to include van der Waals (vdw) interactions.[132, 147] The project-augmented wave (PAW) method was used to represent the core-valence interaction.[163, 164] For the calculations of total energy, a cutoff energy of 400 eV was set for plane wave basis sets to expand the valence electronic states. Transition states (TS) were

determined by a constrained optimisation method[159, 165-168] in which the TSs are verified until (i) all forces on atoms are vanished and (ii) the total energy reaches a maximum along the reaction coordinate but a minimum with respect to the rest of the degree of freedom. As the temperature-programmed reduction profiles from Burch et al.[178] indicated that the Re remained in its oxidised state even at a temperature of ~600 K which was above the experimental temperature of Chen et al.,[91] the Re/Pt surface was modelled with a p(3 x 3) Re(0001) monolayer covered by the maximum number of 8 oxygen atoms on a p(6 x 4) 3-layer Pt(111) flat surface, and the flat surface of Pt was modelled by a p(4 x 4) 4-layer Pt(111) facet. The bottom 2 layers were frozen. The vacuum between the slabs was set at 15 Å to minimise the effect of the slab. The Brillouin zone was sampled with a 2x3x1 k-point grid for Re/Pt system, and 3x3x1 k-point grid for Pt (111). Surface relaxations were performed until all forces were lower than 0.05 eV/Å. To obtain the free energy of species, some standard formulae of statistical mechanics were used to calculate the thermodynamic correction including zero point energy, thermal energy, and entropy derived from partition functions.[171, 172] The total energies were converted into Gibbs free energies according to $G = E + E_{ZPE} + U - TS$ (ZPE = zero point energy) at 403 K. All the reaction energies and activation barriers were reported as the Gibbs free energy calculated under reaction condition of 403 K with the hydrogen pressure of 50 bar, which was stated in the experiment,[91] while other components were treated at 1 bar pressure. The adsorption energy (ΔG_{ad}) was defined as

$$\Delta G_{ad} = G_{adsorbate+slab} - G_{adsorbate} - G_{slab}$$

where G_{slab}, $G_{adsorbate}$, and $G_{adsorbate+slab}$ are the free energies of slab, adsorbate in the gas phase, and adsorbate adsorbed on the slab, respectively. Vibrational analyses were carried

out to ensure the transition states had one imaginary frequency only along the reaction coordinate, and all of the lowest-energy conformations and intermediates were confirmed to have all real frequencies.

5.3. Results

5.3.1. Adsorption of intermediates (furfural, furfuryl alcohol, and 2-methylfuran)

There were three important compounds in the furfural conversion, which were furfural, furfuryl alcohol, and 2-methylfuran. The adsorption details were expressed in the following order; then the hydrogenation reaction pathways were presented, and the hydrodeoxygenations in later sessions. Figure 5-1 shows the Re/Pt bimetallic surface and adsorption conformations of the most stable geometries. Overall, these three compounds preferred to adsorb on the edge of Re layer due to the coordinate unsaturation of the atoms.

In the furfural adsorption configuration, the ring carbon atoms bonded to the edge Re atoms with the hydrogens pointed away from the surface, while the ring oxygen atom pointed towards the Pt layers. However, in the carbonyl part, the adsorption mode was reversed, with only the oxygen bonded on the adjacent Re atom. As the carbonyl functional group was saturated by hydrogenations, the aliphatic carbon and oxygen atoms of furfuryl alcohol were both further away from the Re edge, and the bond length of Re-O extended 0.22 Å longer than that of furfural. On the other hand, the furyl ring remained similar to that of the furfural adsorption. With the removal of the aliphatic oxygen to yield 2-methylfuran, the only difference to the furfural was that the methyl group pointed away from the surface.

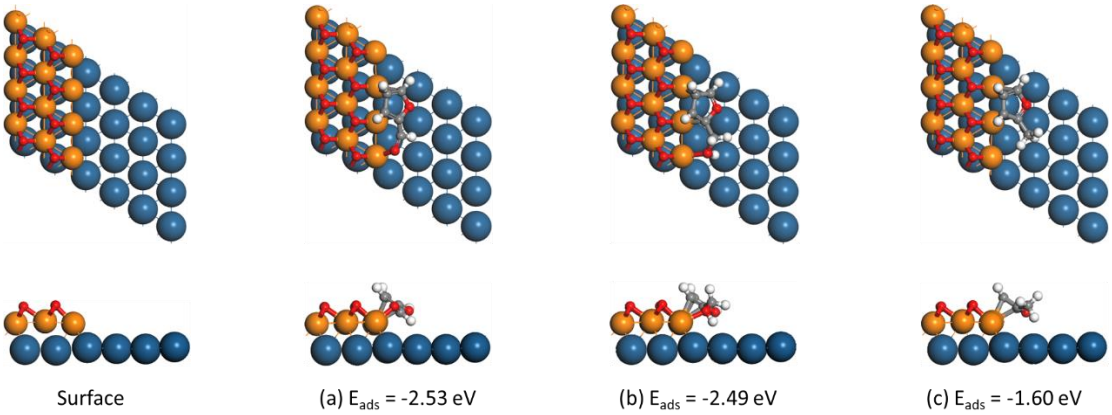

Figure 5-1 Top and side views of the Re/Pt surface structure and the most stable adsorption geometries

Which (a) is furfural, (b) is furfuryl alcohol, and (c) is 2-methylfuran respectively.

Comparing the adsorption energies of the three compounds, it was clear that the adsorption strength of the compounds was mainly attributed to the furan ring and the carbonyl oxygen. The unsaturated oxygen contributed less magnitude than the furan ring on the adsorption (0.93 eV vs 1.60 eV).

5.3.2. Mechanism of furfural conversions

There were two main reaction mechanisms of furfural conversion, which were hydrogenation and hydrodeoxygenation to generate furfuryl alcohol and 2-methylfuran, respectively. We identified the energy barriers, reaction energies, and the free energy profile was obtained. Hydrogen atom adsorption was most stable at the hollow site of the top Pt layer with the adsorption energy of 0.34 eV in the system, the geometry of which is shown in Figure 5-2. All the free energies were set with a reference of furfural adsorption plus two hydrogen molecules in the gaseous phase, except the water formation which was

referenced to the oxygen atom adsorption plus one hydrogen molecule in the gaseous phase.

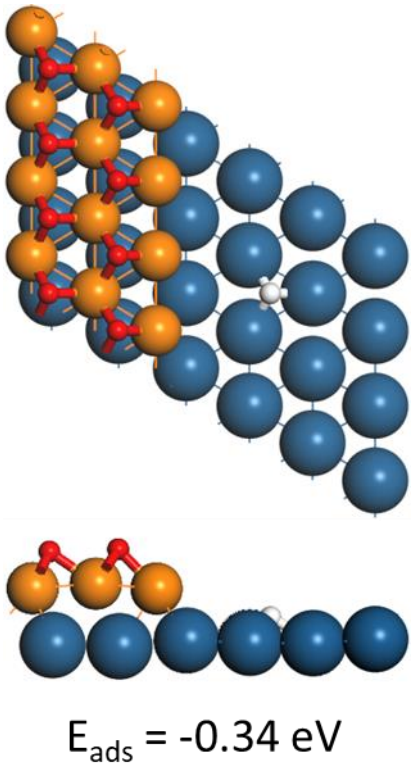

Figure 5-2 Adsorption of hydrogen atom on Re/Pt bimetallic system

5.3.2.1. Reaction pathways of furfural conversion to furfuryl alcohol

As DFT work on Pd suggested that 2-methylfuran was generated via the production of furfuryl alcohol,[112] the hydrogenation of furfural into furfuryl alcohol was calculated first. The reaction pathways could be split either via an alkoxide intermediate or via a hydroxyalkyl species in the order of hydrogenation. The reaction pathways are shown in figure 5-3.

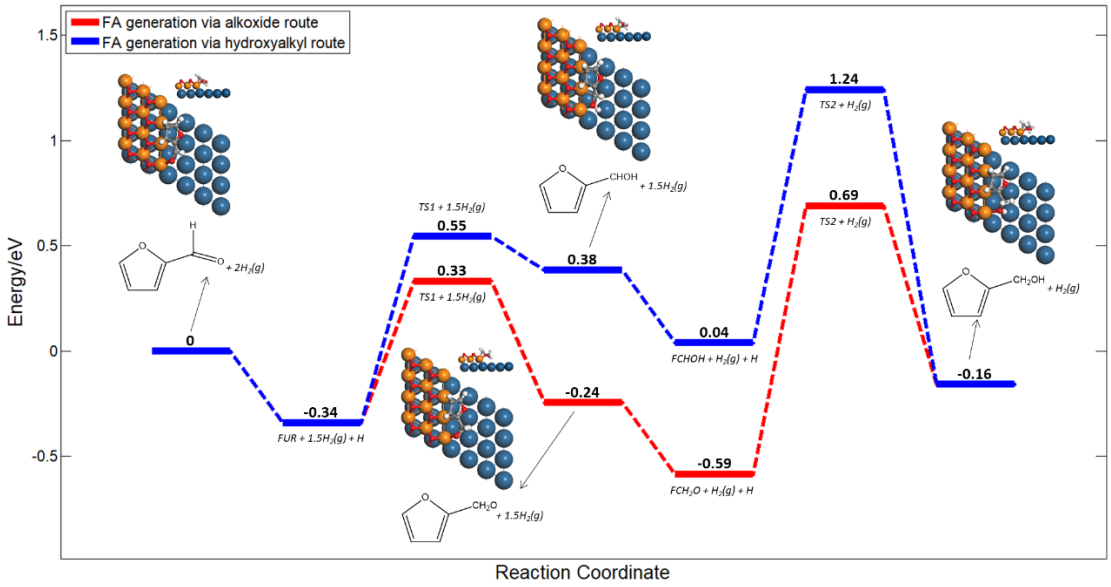

Figure 5-3 a) Reaction profile of furfural conversions to furfuryl alcohol

Which the red line represents the alkoxide route, and the blue line represents the hydroxyalkyl route.

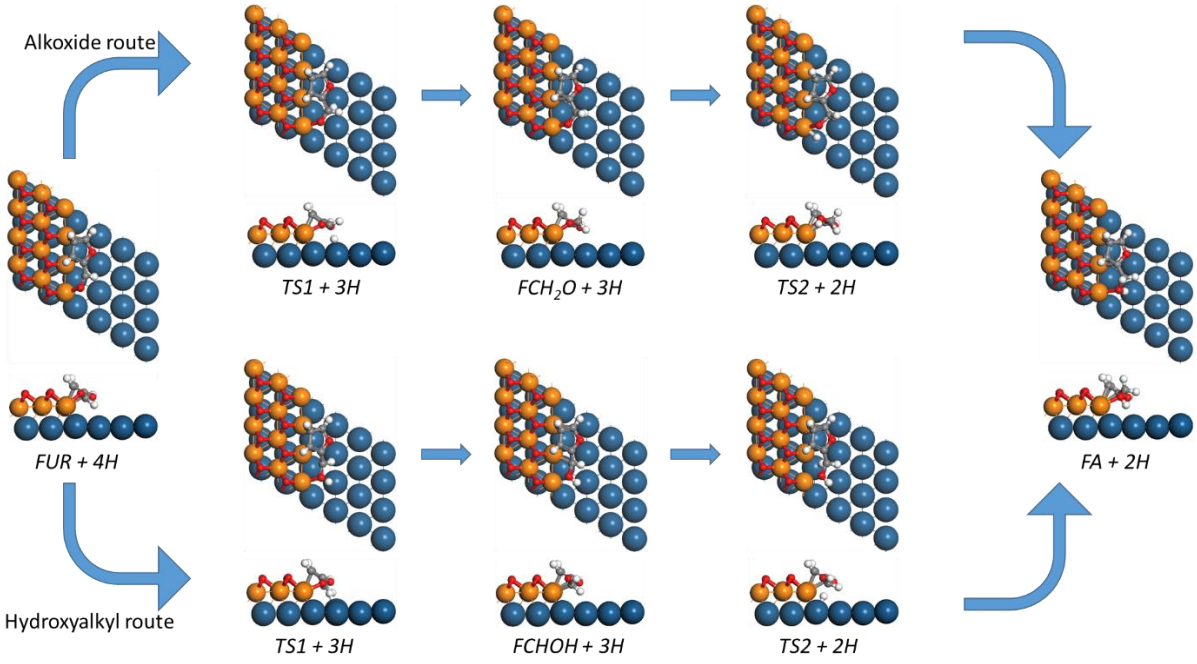

Figure 5-3 b) Mechanisms of furfural conversion to furfuryl alcohol

5.3.2.1.1. Alkoxide route

The first hydrogenation at the carbonyl carbon was initiated by the hydrogen approached the aliphatic carbon of furfural at a Pt top site with a H-C distance of 1.57 Å in the transition state and the original aldehyde hydrogen pointed away from the surface. The carbonyl C-O bond length was 1.33 Å, and the bond length of aromatic C-aliphatic C was 1.47 Å. The alkoxide intermediate was generated at the final state, in which the new C-H bond had a length of 1.11 Å with the C moved further away from the surface. In contrast to the initial state, the C-O bond increased from 1.36 Å to 1.42 Å, and the C-C bond also extended from 1.43 Å to 1.52 Å. The aliphatic oxygen was further attacked by a hydrogen atom at the Re step position. In the transition state, the H-O distance was 1.31 Å, while the O-Re bond length was 2.12 Å, and the C-O distance was 1.45 Å. With the furfuryl alcohol was generated subsequently in the final state, the new H-O bond formed at a length of 1.02 Å. Comparing with the alkoxide initial state, the bond length of O-Re increased from 1.91 Å to 2.25 Å, while the C-O distance also extended from 1.42 Å to 1.46 Å.

5.3.2.1.2. Hydroxyalkyl route

The hydroxyalkyl route started with the hydrogen approached from a Pt top site. In the transition state, the forming H-O distance was 1.30 Å, the O-Re bond distance was 2.19 Å, and C-O bond length was 1.40 Å. As the hydroxyalkyl species was generated, the new H-O bond formed at a distance of 0.98 Å. Comparing with the initial state, the O-Re distance increased from 2.03 Å to 2.28 Å, and the C-O bond length also extended from 1.36 Å to 1.45 Å. When the second hydrogen approached the aliphatic carbon of furfural, the H-C distance was 1.38 Å, the C-O bond length was 1.43 Å, and the C-C bond distance was 1.45

Å in the transition state. As the furfuryl alcohol was produced, the new C-H bond formed at a distance of 1.10 Å. Comparing with the initial state, the C-O bond increased from 1.45 Å to 1.46 Å, and the C-C bond length also extended from 1.43 Å to 1.51 Å.

5.3.2.2. Water formation

As the C-O bond rupture is necessary in 2-methylfuran production, oxygen atom and hydroxyl species are generated as by-products; these species were shown to be important on oxophilic catalyst applications,[179, 180] as they adsorbed strongly on the Re surface which may cause catalyst deactivation. The water formation via hydrogenations of these species should be considered into the whole reaction mechanism. It was found that these reaction steps possess larger activation barriers than the hydrogenolysis reactions. The successive hydrogenations of oxygen to water are shown in figure 5-4.

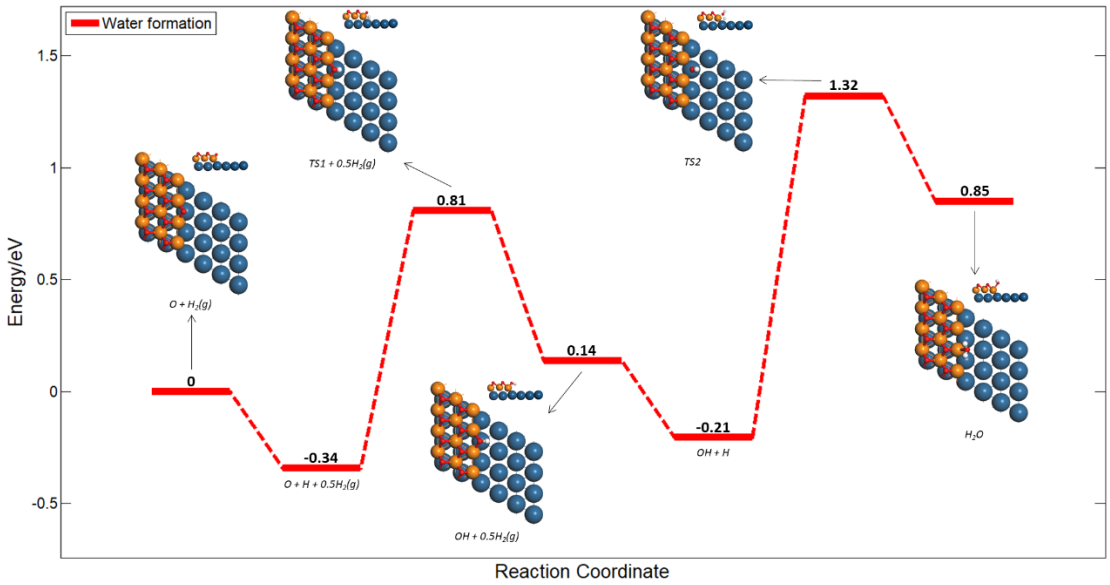

Figure 5-4 a) Reaction profile of water formation via successive hydrogenations of oxygen atom

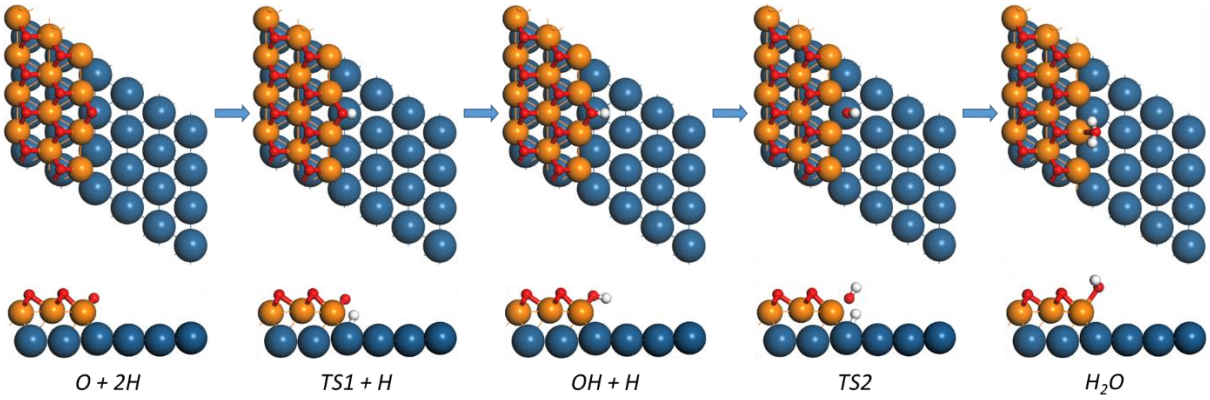

Figure 5-4 b) Mechanism of successive hydrogenations of oxygen into water

The reaction started with oxygen atom adsorbed at the bridge site of the Re edge, and the hydrogen approached from a Pt top site. The H-O distance was 1.36 Å in the transition state. As the hydroxyl species was generated, the new H-O bond formed at a distance of

0.98 Å. Comparing the transition state with the initial state, the Re-O distance increased from 1.94 Å to 2.12 Å. The hydroxyl species was then attacked by another hydrogen from a Pt top site in the transition state, and the H-O distance was 1.27 Å. As the water was produced and adsorbed at a top site of Re edge via its oxygen atom, the new H-O bond formed at a distance of 0.98 Å in the final state. The Re-O distance also increased from 2.12 Å in the initial state to 2.25 Å. The activation barriers of hydrogenation of oxygen atom and hydroxyl species were 1.15 eV and 1.53 eV, respectively.

5.3.2.3. Reaction pathways of 2-methylfuran formation

In the investigation of the mechanisms, four pathways were considered in total, which originated from furfural, alkoxide intermediate, hydroxyalkyl species, and furfuryl alcohol, respectively. The pathways were expressed in the order of successive hydrogenations before the C-O bond cleavage, which means route 1 via the production of furfuryl alcohol, route 2 via alkoxide intermediate, route 3 via hydroxyalkyl species, and route 4 directly from furfural. All these pathways had the same products of 2-methylfuran and water generated at the end.

5.3.2.3.1. Direct cleavage of OH functional group from furfuryl alcohol

Pathway 1 initiated with the direct cleavage of the C-OH bond at the beginning, followed by successive hydrogenations of the furyl-CH_2 and OH intermediates separately. The reaction mechanism is shown in figure 5-5.

In the first step, the C-O bond stretched to 2.04 Å in the transition state, the resulting C-C bond was 1.41 Å, and the Re-O distance was 2.03 Å. As the furyl-CH_2 intermediate was generated via the complete cleavage of the C-O bond, OH species diffused away and adsorbed at an adjacent bridge site of Re edge. At the final state, the C-C bond length decreased from 1.51 Å to 1.43 Å, and the Re-O bond decreased from 2.25 Å to 2.12 Å by comparing with the initial state. The furyl-CH_2 intermediate was then attacked by a hydrogen atom, and in the transition state the H-C distance was 1.45 Å, while the C-C bond length was 1.43 Å. When the 2-methylfuran was produced, the new H-C bond formed with a distance of 1.10 Å, and the C-C bond length extended from 1.43 Å in the initial state to 1.49 Å.

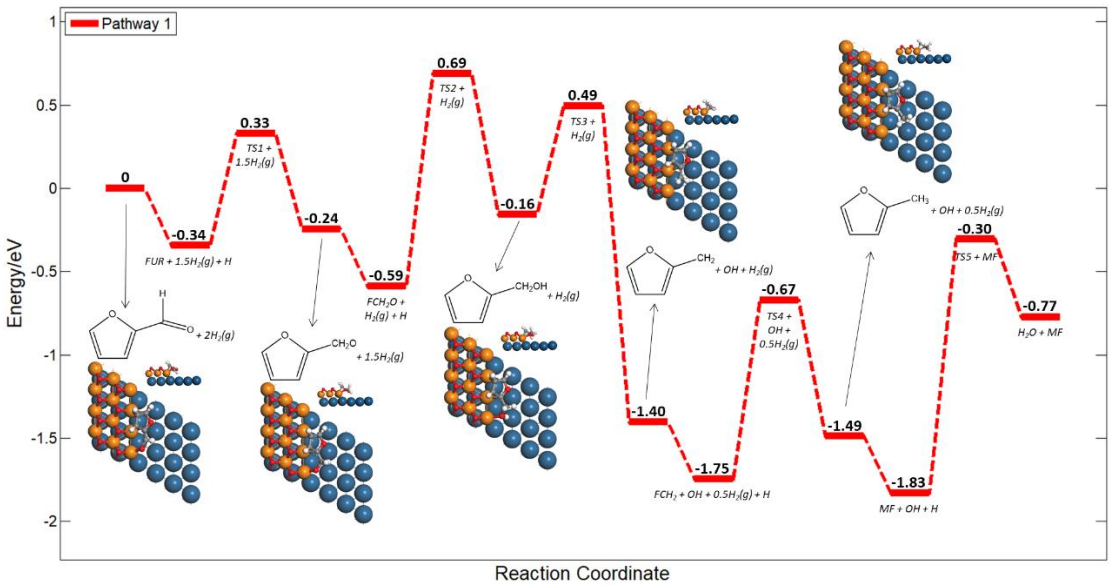

Figure 5-5 a) Reaction profile of 2-methylfuran formation via direct cleavage of C-OH bond of furfuryl alcohol

Which is defined as pathway 1.

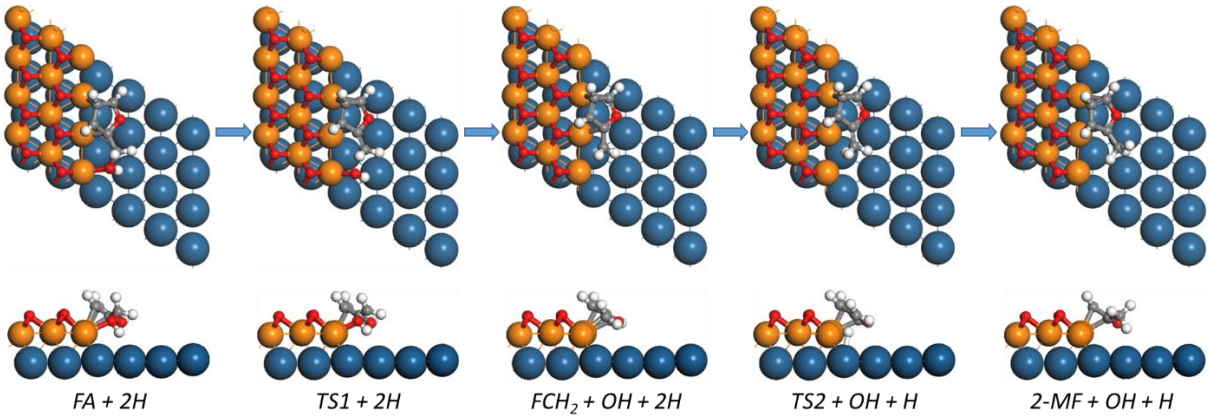

Figure 5-5 b) Mechanism of 2-methylfuran formation via direct cleavage of C-OH bond of furfuryl alcohol

5.3.2.3.2. Cleavage of C-O bond of alkoxide intermediate

Pathway 2 started from the cleavage of the C-O bond of the alkoxide intermediate, followed by successive hydrogenations of the furyl-CH_2 and O intermediates separately. The reaction mechanism is shown in figure 5-6.

In the first step of hydrogenation, the C-O bond increased to 1.96 Å in the transition state, the C-C bond length was 1.43 Å, and the Re-O distance was 1.79 Å. In the final state, furyl-CH_2 was produced with an oxygen atom adsorbed at adjacent bridge site of Re edge with an decrease of the C-C bond length from 1.52 Å to 1.43 Å and an increase of the Re-O bond from 1.91 Å to 1.94 Å comparing with the initial state. The successive furyl-CH_2 hydrogenation was described in pathway 1 (see 5.3.2.3.1.).

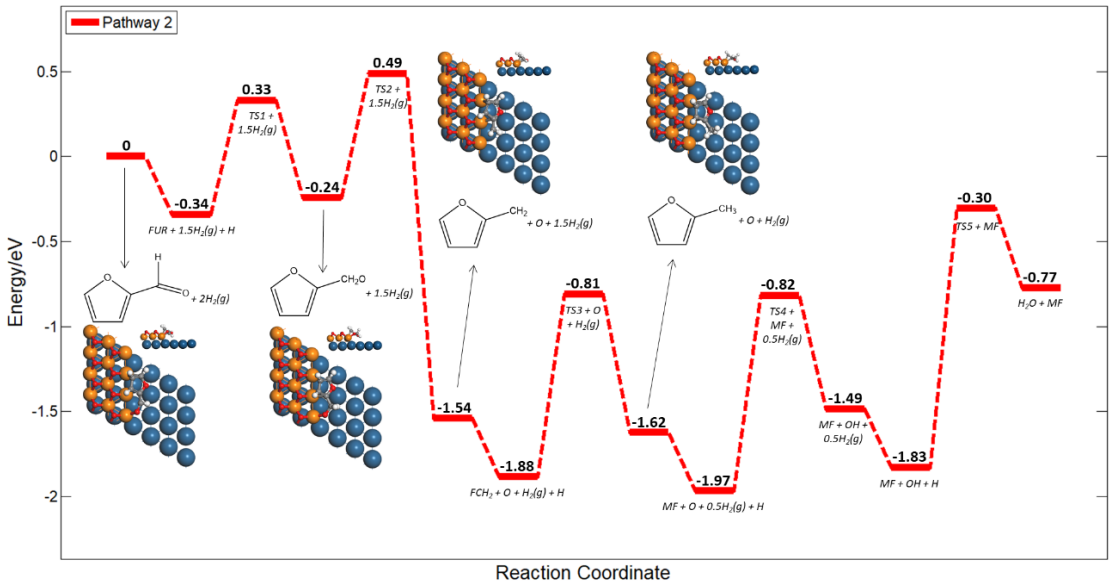

Figure 5-6 a) Reaction profile of 2-methylfuran formation via the cleavage of C-O bond of alkoxide intermediate

Which is defined as pathway 2.

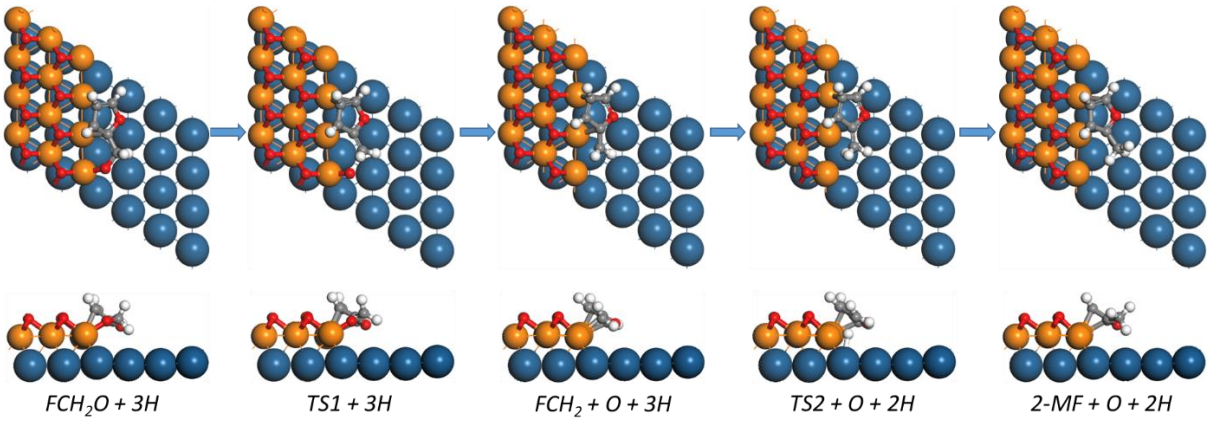

Figure 5-6 b) Mechanism of 2-methylfuran formation via the cleavage of C-O bond of alkoxide intermediate

5.3.2.3.3. Cleavage of OH functional group from hydroxyalkyl species

Pathway 3 originated from the C-OH bond breaking of the hydroxyalkyl species, followed by successive hydrogenations of the furyl-CH and OH intermediates separately. The reaction mechanism is shown in figure 5-7.

In the first step, the C-OH bond stretched to 1.93 Å, the resulting C-C bond was 1.42 Å, and the Re-O distance was 2.09 Å in the transition state, yielded furyl-CH and OH species as products. Contrast to the initial state, at the final state the C-C bond contracted from 1.43 Å to 1.42 Å, and the Re-O bond shortened from 2.28 Å to 2.12 Å. The generated furyl-CH intermediate was then attacked by a hydrogen atom from top site of Re atom, and in the transition state the H-C distance was 1.62 Å and the C-C bond length was 1.45 Å. The new H-C bond was formed at 1.10 Å as the furyl-CH_2 was produced, and the 2-methylfuran production from hydrogenation of furyl-CH_2 intermediate was described in pathway 1 (see 5.3.2.3.1.).

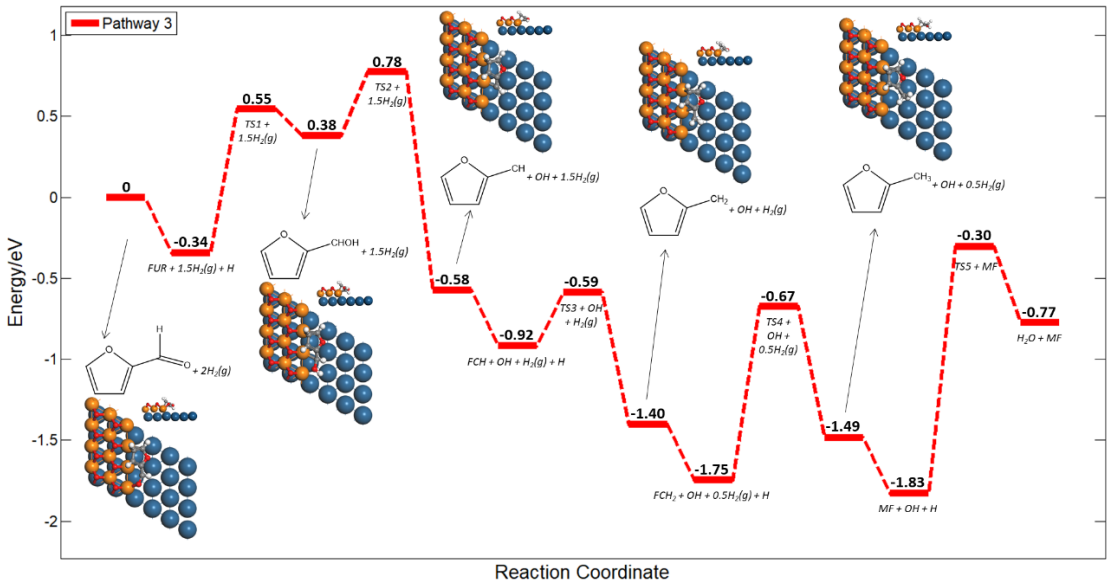

Figure 5-7 a) Reaction profile of 2-methylfuran formation via the cleavage of C-OH bond of hydroxyalkyl intermediate

Which is defined as pathway 3.

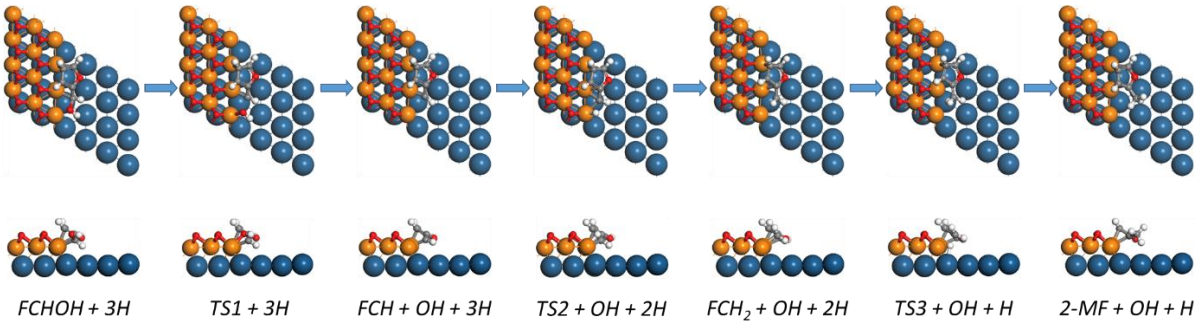

Figure 5-7 b) Mechanism of 2-methylfuran formation via the cleavage of C-OH bond of hydroxyalkyl intermediate

5.3.2.3.4. Direct C-O cleavage from the furfural

Pathway 4 is shown in figure 5-8, which started from the direct cleavage of the carbonyl bond of furfural, followed by successive hydrogenations of the resultant furyl-CH and O intermediates separately. During the C-O bond rupture, the C-O bond lengthened to 1.83 Å in the transition state, while the resulted C-C bond length was 1.42 Å and the Re-O distance was 1.81 Å. Comparing with the initial state, the C-C bond length decreased from 1.43 Å to 1.42 Å, and the Re-O distance decreased from 2.03 Å to 1.94 Å at the final state. Then, furyl-CH and oxygen atom were generated. The successive hydrogenations of furyl-CH intermediate were described in the second step of pathway 3 and second step of pathway 1, respectively.

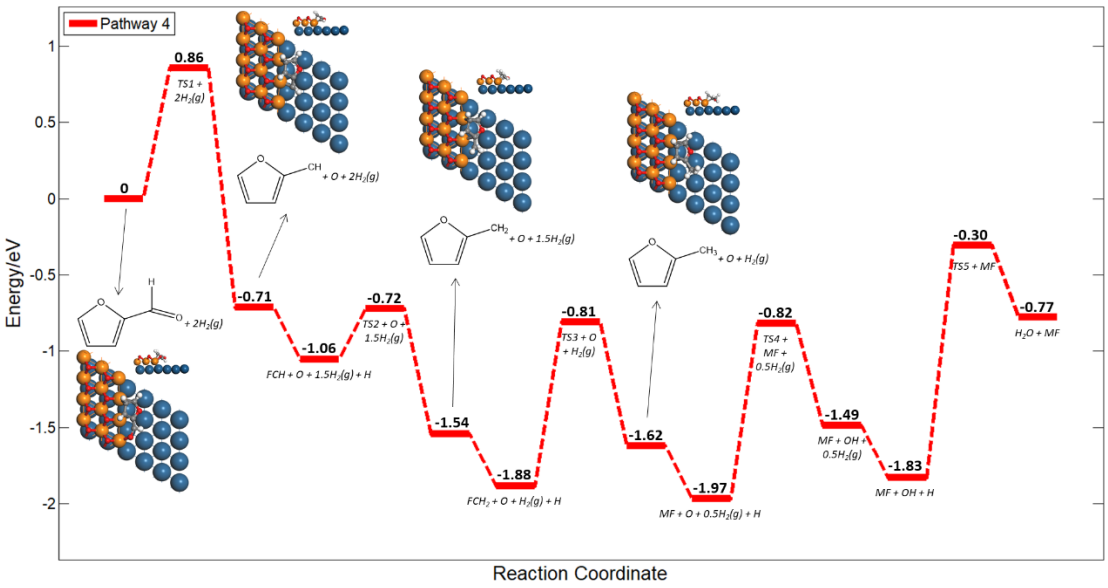

Figure 5-8 a) Reaction profile of 2-methylfuran formation via the direct cleavage of C-O bond of furfural

Which is defined as pathway 4.

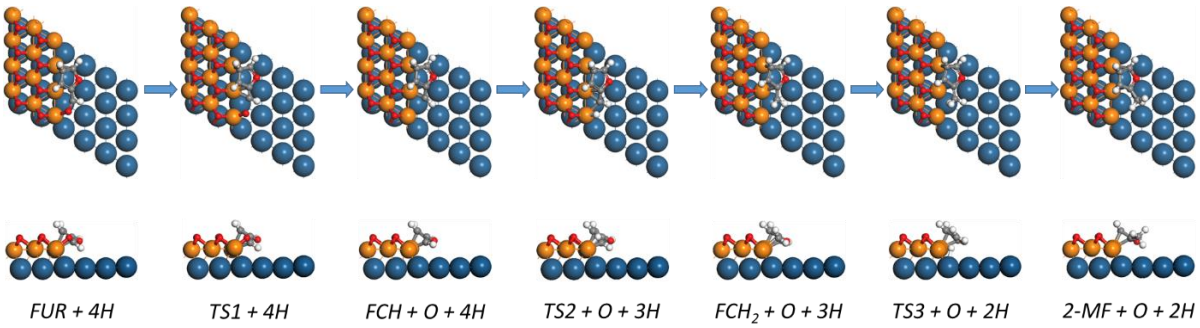

Figure 5-8 b) Mechanism of 2-methylfuran formation via the direct cleavage of C-O bond of furfural

5.3.2.4. Furan formation via decarbonylation pathway

As there is another key compound, furan, which was shown to be the thermodynamically favourable product on Pd(111) and Pt(111),[110, 112] the decarbonylation pathway was also tried. It was supposed to break the carbon-hydrogen bond of carbonyl group first, followed by the bond rupture of aromatic carbon-carbonyl carbon, finally rehydrogenated the furyl intermediate to furan. However, we found that the C-C bond cannot be cleaved, and hence only the initial dehydrogenation step is presented in the figure 5-9.

In the transition state of the first step dehydrogenation, the aliphatic C-H bond stretched to 1.59 Å with the H bonded to a top site of Pt, while the C-O bond length was 1.32 Å, and the C-C bond distance was 1.45 Å. As the furyl-CO intermediate was generated via the rupture of the C-H bond, the hydrogen atom diffused away resulting in an adsorption at a rear Pt hollow site.

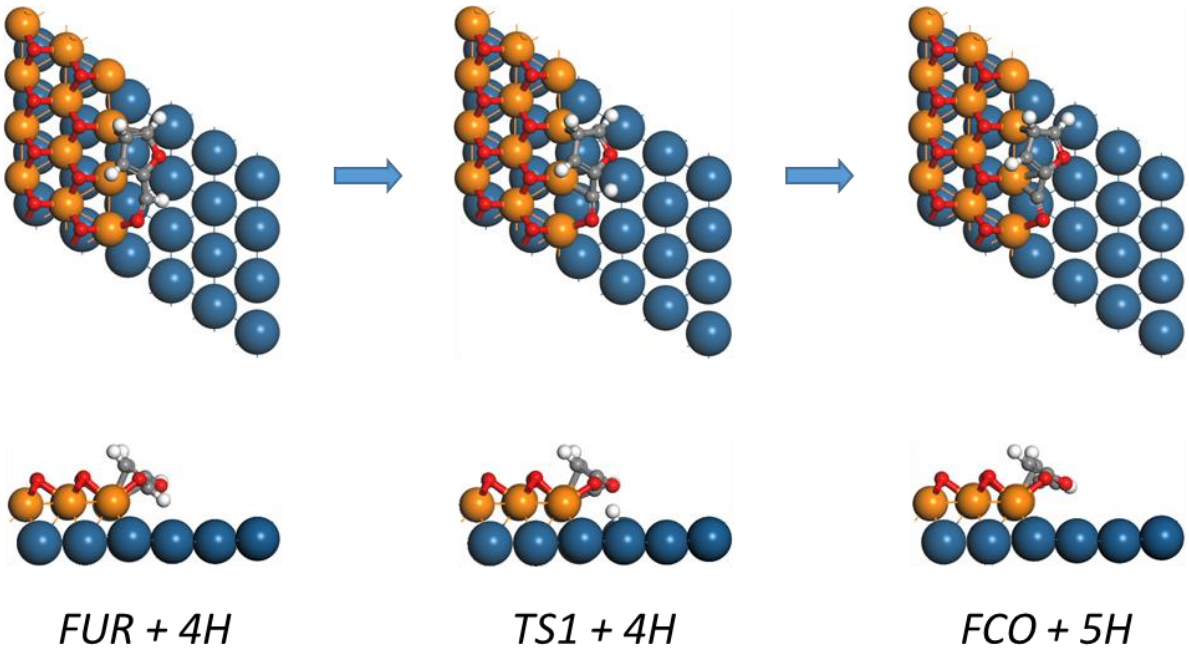

Figure 5-9 Mechanism of furfural dehydrogenation

5.4. Discussions

5.4.1. Determination of the selectivity of hydrogenation and hydrodeoxygenation routes at 403 K on Re/Pt surface

The overall reaction profiles of 2-methylfuran formation, and comparison between the best pathways for the formations of furfuryl alcohol and 2-methylfuran are shown in figure 5-10, from which the best reaction pathway in each route was determined by the effective barrier. The effective barrier was determined from the largest gap between the lowest energy state and the highest energy state in the direction of forward reaction, which was used roughly to estimate the easiness of the pathway. For example, in pathway 4 of figure 5-10 (a), the lowest energy state was -1.97 eV (MF + O + 0.5H_2(g) + H), the highest energy state was -0.30 eV (TS5 + MF), hence the effective barrier was 1.67 eV.

In the bimetallic Re/Pt system, the effective barriers of hydrogenation routes towards the production of furfuryl alcohol were composed of both the hydrogenation steps, as shown in figure 5-3. The effective barriers were 1.28 eV and 1.58 eV for the alkoxide and hydroxyalkyl routes, respectively, and hence it was clear that the generation of furfuryl alcohol was preferred via the alkoxide route which is represented by the red pathway in figure 5-3. While the effective barriers of the hydrodeoxygenation routes towards the production of 2-methylfuran were composed of several reaction steps. For pathways 1 and 3, it was the OH hydrogenation step, with an effective barrier value of 1.53 eV. In pathways 2 and 4, there were two reaction steps involved in the effective barrier calculation, which were the hydrogenations of oxygen atom and OH species successively, and they contributed to an effective barrier value of 1.67 eV. Despite pathways 1 and 3 had the same effective barrier value, pathway 3 had a smaller second effective barrier of 1.12 eV from furfural hydrogenated to hydroxyalkyl intermediate and successive C-O bond rupture, while the second effective barrier of pathway 1 was 1.28 eV which came from the hydrogenation of the alkoxide intermediate. Therefore, pathway 3 was the best reaction pathway for the hydrodeoxygenation of furfural which is represented by the green pathway in figure 5-10 a).

a)

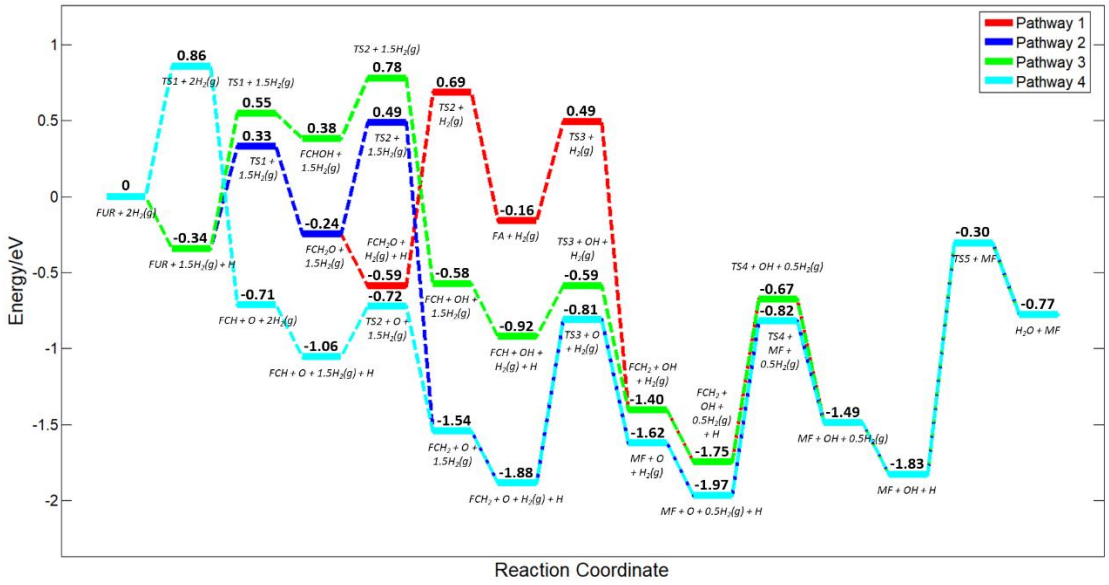

b)

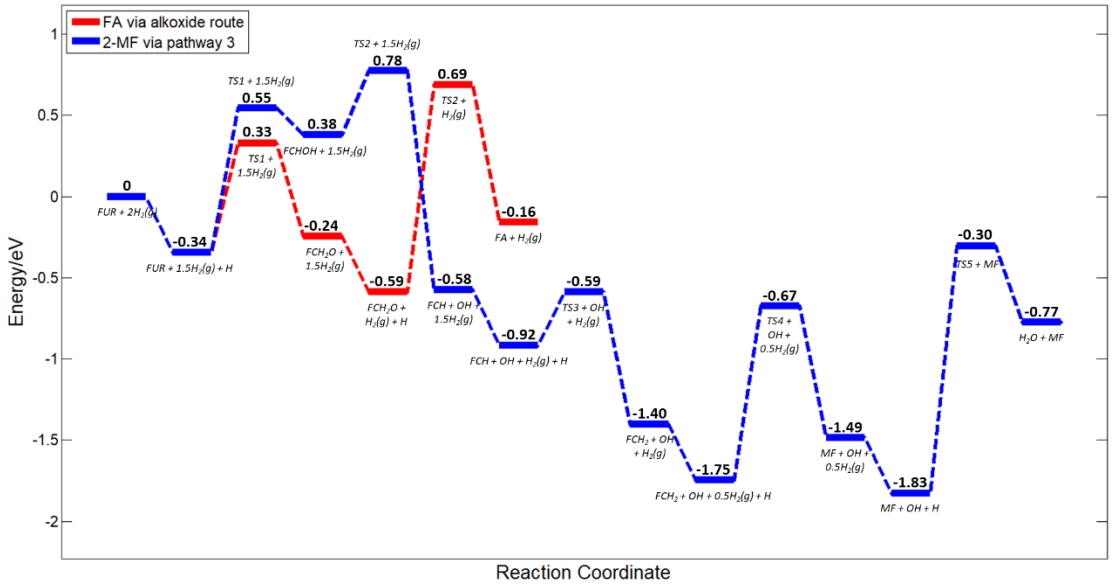

Figure 5-10 Free energy reaction profiles at 403 K in Re/Pt bimetallic system

Which a) shows all the four pathways of production of 2-methylfuran; which the red, blue, green, and cyan lines represent pathway 1, 2, 3, and 4 respectively. b) illustrates overall comparison of the most favoured formation routes of furfuryl alcohol and 2-methylfuran;

which the red and blue lines represent the furfuryl alcohol formation via alkoxide route, pathway 3 of 2-methylfuran formation respectively.

By comparing the effective barriers of the reaction routes in figure 5-10 b), it was clear that at 403 K, the kinetically favoured order was furfuryl alcohol (1.28 eV) > 2-methylfuran + H_2O (1.53 eV); and the thermodynamically favoured order was 2-methylfuran + H_2O (-0.77 eV) > furfuryl alcohol (-0.16 eV). In pathway 3 for 2-methylfuran generation which is represented by the blue route, if the reduction of surface hydroxyl species was not taken into account (the state of MF + OH + H is treated as the final state), the effective barrier was 1.12 eV, which was smaller than the effective barrier of furfuryl alcohol production (1.28 eV); however, when the surface coverage effect was considered, the increased surface coverage of MF + OH + H should enhance the rate of the reverse reaction due to the difficulty of forward reaction. Hence the furfuryl alcohol production pathway was favoured as the products desorbed to the gas phase which is represented by the red route.

In the experiments of Re/Pt furfural conversion,[91] the major product was furfuryl alcohol, which was consistent to our kinetically favoured product. Additionally, the hydrogenation of surface oxygen-related species was proved to be difficult, which was also in agreement with the temperature-programmed reduction profiles from Burch et al.,[178] which showed the rhenium was in its oxidised form at the given reaction temperature of Chen et al.[91]

5.4.2. Rhenium effects on the C-O bond and C-C bond cleavages

There were many studies to show the incorporation of an oxophilic metal to platinum could improve the hydrogenation and hydrodeoxygenation selectivities on furfural conversion. Shi et al. showed that the furfural underwent decarbonylation and ring-opening mechanisms to produce propene and carbon monoxide on Pt(111) surface.[90] Wan et al. performed furfural hydrodeoxygenation over Fe/Pt(111) and Pt(111),[181] and 2-methylfuran was detected as a product in temperature-programmed desorption on Fe/Pt(111), but it did not appear on Pt(111). It was attributed to the oxophilic property of iron which facilitated the rupture of the carbonyl bond. Zhang et al. reported that with the addition of copper to platinum,[182] the hydrogenation selectivity to furfuryl alcohol was improved, while the decarbonylation selectivity to furan was declined. Jiang et al. also investigated the effect of incorporation of oxophilic metals to platinum on furfural hydrodeoxygenation as well,[94] and they found that the strong oxophilic cobalt metal deposited on Pt(111) presented high selectivity to 2-methylfuran. They also concluded that the surface quantity of oxygen could inhibits the production of 2-methylfuran, which were in good agreement with our work. This could be understood as follows: Once the rhenium was covered by oxygens at the given reaction temperature, the acquisition of extra oxygen species from furfural conversion became difficult, which retarded the formation of 2-methylfuran.

In order to gain more insights into the system, similar reactions were computed on monometallic flat surface of Pt to find the additional effect from the oxophilic Re, as shown in figure 5-11. On the flat Pt surface, the rate determining step of decarbonylation route was found to be dehydrogenation of furfural (the barrier is 0.93 eV), which was consistent

with the suggestion of Cai et al.[110] However, as they did not complete the route of 2-methylfuran production, we only computed the key steps in our system for comparison. Using the hydrogenations of furyl-CH_2 intermediate and OH species as key steps, which were attributed to the effective barrier in Re/Pt bimetallic system, we obtained a value of 0.87 eV on Pt(111). This result suggested that the reaction should favour hydrodeoxygenation route, but unfortunately the decarbonylation route was proved to be better by experiments.[90] As the active hydrogenation metals were well known to suppress the C-O bond breaking, hence all the four types of C-O cleavage step were calculated on Pt(111), the C-O bond breaking in furfuryl alcohol, FCH_2O intermediate, FCHOH species, and furfural, contributed to the barrier values of 1.37, 1.16, 2.04, and 3.81 eV, respectively. Therefore, it was obvious that the prohibition of hydrodeoxygenation route came from the cleavage of C-O bond in Pt systems.

Based on the results, that the decarbonylation pathway to generate furan from furfural could not be achieved due to the difficulty of aromatic carbon-carbonyl carbon bond breaking, which was consistent to the experiment results as no furan was detected,[91] while the reactions with Pt only yielded ring open products and carbon monoxide.[90, 91] Therefore, the introduction of Re clearly retarded the rupture of C-C bond. Overall, our calculations showed that with the addition of Re to Pt, the C-O bond cleavage was promoted and C-C bond rupture was prohibited; however, the removal of oxygen-related species was still a crucial factor which prevented the production of 2-methylfuran.

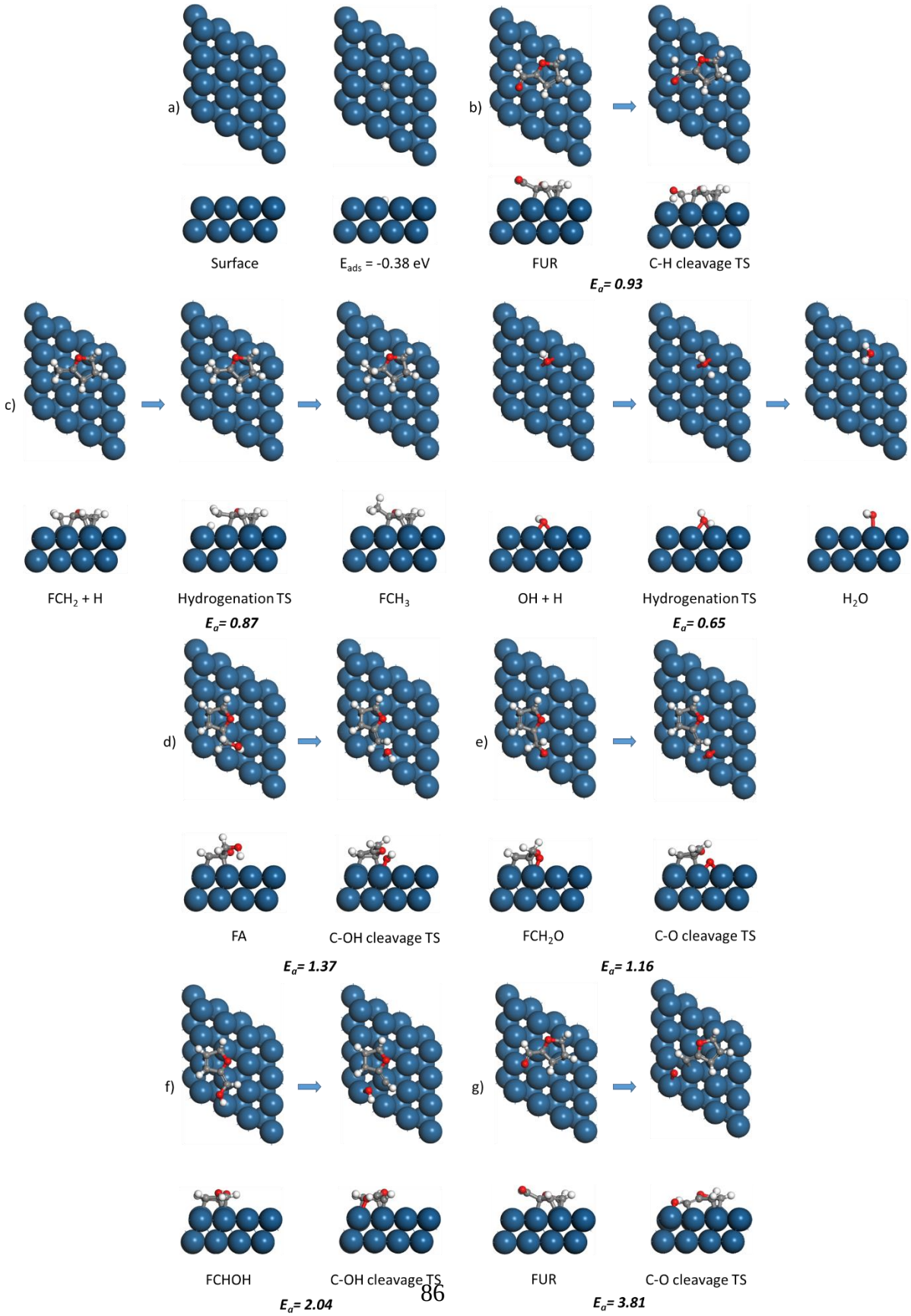
a)
b)
Surface
E_{ads} = -0.38 eV
FUR
C-H cleavage TS
E_a= 0.93
c)
FCH_2 + H
Hydrogenation TS
FCH_3
OH + H
Hydrogenation TS
H_2O
E_a= 0.87
E_a= 0.65
d)
e)
FA
C-OH cleavage TS
FCH_2O
C-O cleavage TS
E_a= 1.37
E_a= 1.16
f)
g)
FCHOH
C-OH cleavage TS
FUR
C-O cleavage TS
E_a= 2.04
E_a= 3.81

Figure 5-11 Key steps of furfural hydrodeoxygenation reaction structures on Pt(111) Which a) shows the Pt(111) surface with single hydrogen atom adsorption energy. b) shows the initial C-H cleavage barrier of furfural. c) shows the hydrogenation barriers of FCH_2 to 2-methylfuran and hydroxyl to water. d), e), f) and g) shows the C-O cleavage barrier of furfuryl alcohol, FCH_2O, FCHOH, and furfural respectively.

5.4.3. Synergistic effects in Re/Pt system

Basically in the calculations, the Re was covered by the maximum amount of oxygen to represent the high oxidation state of Re in the experiment, and no oxygen covered on the Pt layer, which was consistent with the experimental XPS data that indicated the Re was in Re^{6+}/Re^{7+} state, and Pt was in Pt^0 state.[91] The reaction concept was the furfural adsorbed on the Re/Pt interface with the carbonyl group was activated by Re, the hydrogen was activated on the surface of Pt and transferred to the interface to selectively hydrogenate the carbonyl group of furfural, which was also stated in the experimental work.[91, 178]

5.5. Conclusions

Detailed density functional theory calculations on reaction pathways of furfural conversion via hydrogenation and hydrodeoxygenation at 403 K on a Re/Pt(111) surface was computed using the PBE-D3 functional, and the following results achieved:

(1) For all the key compounds, the furyl ring adsorbed on the Re edge site, and the carbonyl oxygen also played a significant role in the adsorption strength.

(2) Furfural conversion was kinetically favoured on the hydrogenation route to generate furfuryl alcohol, but the hydrodeoxygenation mechanism to generate 2-methylfuran and water was thermodynamically favoured.

(3) Production of 2-methylfuran was achievable with the furfural was first hydrogenated into hydroxyalkyl species. The C-OH bond was then cleaved, followed by successive hydrogenation of the furyl-CH intermediate. However, this reaction route was prohibited by the by-product containing oxygen. Because the oxidised Re surface could not accept further oxygen deposition, which were difficult to be removed in the form of water via hydrogenations at the given reaction temperature.

(4) By comparing with the flat Pt surface, the Re/Pt calculation results indicated that the incorporation of the oxophilic metal to active hydrogenation metals could promote the hydrodeoxygenation route by reducing the C-O bond cleavage barrier, and retarded the C-C bond rupture for the furan production.

Chapter 6 DFT Study of Furfural conversion on $Ni_2P(0001)$

6.1. Introduction

Recently, transition metal phosphides have received much attention for hydrodenitrogenation and hydrodesulfurisation.[98, 99] Due to their good hydrogen transfer ability, metal phosphides have also been applied to the hydrodeoxygenation of biomass-derived molecules such as phenol[183], anisole[100], and guaiacol.[101] The nickel phosphides catalysts were shown to have higher hydrodesulfurisation and hydrodenitrogenation activities than other phosphides.[184] It was also shown that the Ni_2P had a greater activity in hydrodeoxygenation of anisole[100] and guaiacol[101] than other transition metal phosphides like Co_2P, Fe_2P, MoP, and WP. Bui et al. also reported that during the hydrodeoxygenation of 2-methyltetrahydrofuran, the oxygenate products were 85% with Ru, 70% with Pd, and only 12% with Ni_2P.[185] Jiménez-Gómez et al. and Wang et al., performed the hydrodeoxygenation of furfural on Ni_2P, and both groups obtained the 2-methylfuran as the major product.[102, 103]

Due to the properties of cost-effective and eco-friendly, the metal phosphides become popular choices to develop new hydrodeoxygenation catalysts.[186] In this work we used PBE-D3 method to investigate the furfural conversion on the $Ni_2P(0001)$ surface at an experimental temperature of 513 K, which was the temperature performed by Wang et al.[103]

6.2. Method

All calculations reported here were carried out by using plane-wave-based DFT method with application of Vienna ab initio simulation package (VASP).[140, 141] The PBE-D3 correction method was employed in order to include van der Waals (vdw) interactions.[132, 147] The project-augmented wave (PAW) method was used to represent the core-valence interaction.[163, 164] A cut-off energy of 400 eV was set for plane wave basis sets to expand the valence electronic states. Transition states (TSs) were determined by a constrained optimisation method[159, 165-168, 187-189] in which the TSs are verified until (i) all forces on atoms are vanished and (ii) the total energy reaches a maximum along the reaction coordinate but a minimum with respect to the rest of the degree of freedom. During the model construction, we considered the phase of nickel phosphide under the experimental conditions, as the Ni/P ratio depended on the calcination temperature of catalyst. It was shown that the Ni_2P phase formed at 550°C for a supported system,[186, 190] which was consistent with the X-ray diffraction (XRD) data provided by Jiménez-Gómez et al.[102] While among the Ni_2P phase, the (0001) facet was found to be the most thermodynamically favoured surface,[191, 192] and it was composed of Ni_3P_2 and Ni_3P_1 terminations alternatively. The Ni_3P_2-termination was applied in the calculations with the following reasons: (i) Ni_3P_2-termination was more stable than Ni_3P_1-termination with a 2.75 eV lower surface free energy per unit cell,[193] (ii) Based on the dynamic low-energy electron diffraction (LEED) data of $Ni_2P(0001)$, the surface was composed of 20% Ni_3P_2-termination and 80% P-covered Ni_3P_2-termination, because the surface reconstruction happened with additional P adatoms covered Ni 3-fold hollow sites of Ni_3P_2-termination.[194] However, it was believed the P adatoms may diffuse and desorb from the surface, and allow reactants to occupy the

Ni 3-fold hollow sites on the Ni_3P_2-termination which was found to be the catalytic active site.[195, 196] While the Ni_3P_1-termination was also performed in the calculations, but it was used for the decarbonylation reaction only due to the reaction could not be achieved on the Ni_3P_2-termination. The flat surface of Ni_2P was modelled by a p(2x2) 4-layer $Ni_2P(0001)$ facet with Ni_3P_2-termination exposed on the top surface. The bottom 2 layers were frozen and the vacuum between the slabs was set at 15 Å. The Brillouin zone was sampled with a 2x2x1 k-point grid for the calculations. Surface relaxations were performed until all forces were lower than 0.05 eV/Å. To obtain the free energy of species, some standard formulae of statistical mechanics were used to calculate the thermodynamic correction including zero point energy, thermal energy, and entropy derived from partition functions.[171, 172] The total energies were converted into Gibbs free energies according to $G = E + E_{ZPE} + U - TS$ (ZPE = zero point energy) at 513 K. All the reaction energies and activation barriers were reported as the Gibbs free energy calculated under reaction condition of 513 K with the hydrogen pressure of 20 bar, which was reported in the experiment work,[102] while other components were treated at 1 bar pressure. The adsorption energy (ΔG_{ad}) was defined as

$$\Delta G_{ad} = G_{adsorbate+slab} - G_{adsorbate} - G_{slab}$$

where G_{slab}, $G_{adsorbate}$, and $G_{adsorbate+slab}$ are the free energies of slab, adsorbate in the gas phase, and adsorbate adsorbed on the slab, respectively. Vibrational analyses were carried out to ensure the transition states had one imaginary frequency only along the reaction coordinate, and all of the lowest-energy conformations and intermediates were confirmed to have all real frequencies.

6.3. Results and discussions

6.3.1. Adsorption of intermediates (furfural, furfuryl alcohol, and 2-methylfuran)

There were three key intermediates in the furfural conversion to 2-methylfuran on nickel phosphide,[103] which were furfural, furfuryl alcohol and 2-methylfuran. Figure 6-1 shows the Ni_3P_2-termination surface and adsorption conformations of the most stable geometries.

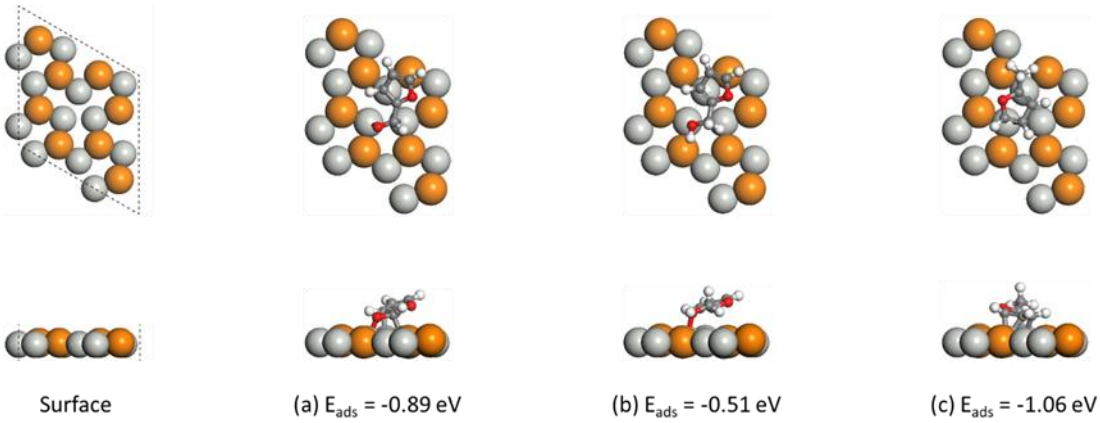

Figure 6-1 Top and side views of the Ni_3P_2-termination surface structure and the most stable adsorption geometries

Which (a) is furfural, (b) is furfuryl alcohol, (c) is 2-methylfuran. Nickel, phosphorus, carbon, oxygen and hydrogen atoms are marked in light grey, orange, dark grey, red and white respectively.

In the furfural adsorption configuration, the furyl ring was tilted away from the surface with only one beta carbon bonded to a Ni atom with a considerable long distance of 2.20 Å, while its carbonyl group adsorbed on the adjacent Ni atoms. As the carbonyl group of furfural was hydrogenated to form furfuryl alcohol, only the aliphatic oxygen bonded to

the surface Ni atom. However, when the carbonyl bond of furfural was converted into methyl group via hydrogenolysis, the 2-methylfuran adsorption geometry was very different from that of furfural and furfuryl alcohol, which bonded to the surface Ni atoms mainly via the ring carbon atoms.

Comparing the adsorption geometries of furfural, furfuryl alcohol, and 2-methylfuran; the intermediates preferred to adsorb on the surface Ni atoms by a priority of the carbonyl group over the furyl ring group. The relative adsorption energies of these intermediates showed that they were in a moderate stabilisation scale when interact with the Ni_3P_2-termination surface.

6.3.2. Reaction mechanisms

During the mechanism research, we identified the energy barriers and the reaction energies to obtain the free energy profiles. Hydrogen atom adsorption was most stable at the Ni trimer site with the adsorption energy of -0.63 eV in the system, the geometry of which is shown in figure 6-2. All the free energy profiles were set with a reference of the relative species in their corresponding adsorption states. In order to identify the best pathway of the conversions, the effective barrier was used as a main reference, which was determined from the largest gap between the lowest energy state and the highest energy state in the direction of forward reaction.[171, 197, 198]

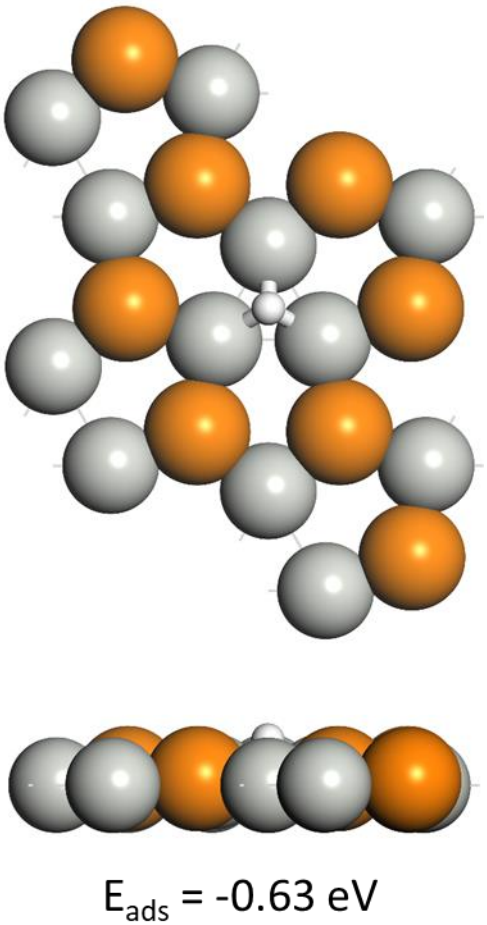

Figure 6-2 Adsorption geometry of hydrogen atom on Ni_3P_2-termination surface

6.3.2.1. Water formation

Before the description of furfural conversions, the water formation was illustrated first, due to the C-O bond rupture was necessary in the 2-methylfuran production. As a result, oxygen atom and hydroxyl species were generated as by-products, hence the water formation via hydrogenations of these species should be considered in the whole reaction mechanism. The calculations showed that these reaction steps possessed larger activation barriers than

the hydrogenolysis reactions of furfural. It was found from the calculations that the oxygen-related species could adsorb either at the Ni trimer site or Ni-P bridge site.

6.3.2.1.1. Ni trimer site route

The reaction started with oxygen atom adsorbed at a Ni-trimer site, and the hydrogen approached from a Ni top site. The H-O distance was 1.61 Å in the transition state. As the hydroxyl species was generated, the new H-O bond formed at a distance of 0.97 Å. By comparing the transition state with the initial state, the Ni-O distance increased from 1.91 Å to 2.03 Å. The hydroxyl species was then attacked by another hydrogen from a Ni top site in the transition state, and the H-O distance was 1.48 Å. As the water was produced and adsorbed at a Ni top site via its oxygen atom, the new H-O bond formed at a distance of 0.98 Å in the final state. The Ni-O distance also increased from 2.03 Å in the initial state to 2.13 Å. The activation barriers of hydrogenation of oxygen atom and hydroxyl species were 1.55 eV and 1.58 eV, respectively.

6.3.2.1.2. Ni-P bridge site route

The reaction started with oxygen atom adsorbed at a Ni-P bridge site, and the hydrogen approached from another P top site. The H-O distance was 1.49 Å in the transition state. As the hydroxyl species was generated, the new H-O bond formed at a distance of 0.99 Å. By comparing the transition state with the initial state, the Ni-O distance increased from 1.97 Å to 2.10 Å, and the P-O bond stretched from 1.57 Å to 1.76 Å simultaneously. The hydroxyl species was then attacked by another hydrogen from a P top site in the transition state, and the H-O distance was 1.37 Å. The water was produced with the same position

described in the Ni-trimer site section. The activation barriers of hydrogenation of oxygen atom and hydroxyl species were 1.40 eV and 1.81 eV, respectively.

As the reaction profile is shown in figure 6-3 a), both hydrogenation steps were involved in the effective barriers of these two routes, which provided the barrier values of 1.61 and 2.33 eV for the Ni trimer and Ni-P bridge routes respectively. Hence, it was clear that the hydrogenations preferred to be achieved at the Ni trimer site rather than the Ni-P bridge site. To obtain a better understanding of the reaction, a charge analysis of the hydroxyl species hydrogenation step was computed, which is shown in figure 6-3 c) and d). On the Ni trimer site, surface Ni atoms promoted the reaction by donating electron charges to both the hydrogen atom and the oxygen of the hydroxyalkyl species. While on the Ni-P bridge site, the P atom transferred more electron charges to make the oxygen more negative than that at the Ni trimer site, and it converted the hydrogen into a hydride species. As both the attacked hydrogen and oxygen possessed higher negative charges, they repelled each other more during the water formation which was represented by the higher activation barrier value (1.81 eV vs 1.58 eV).

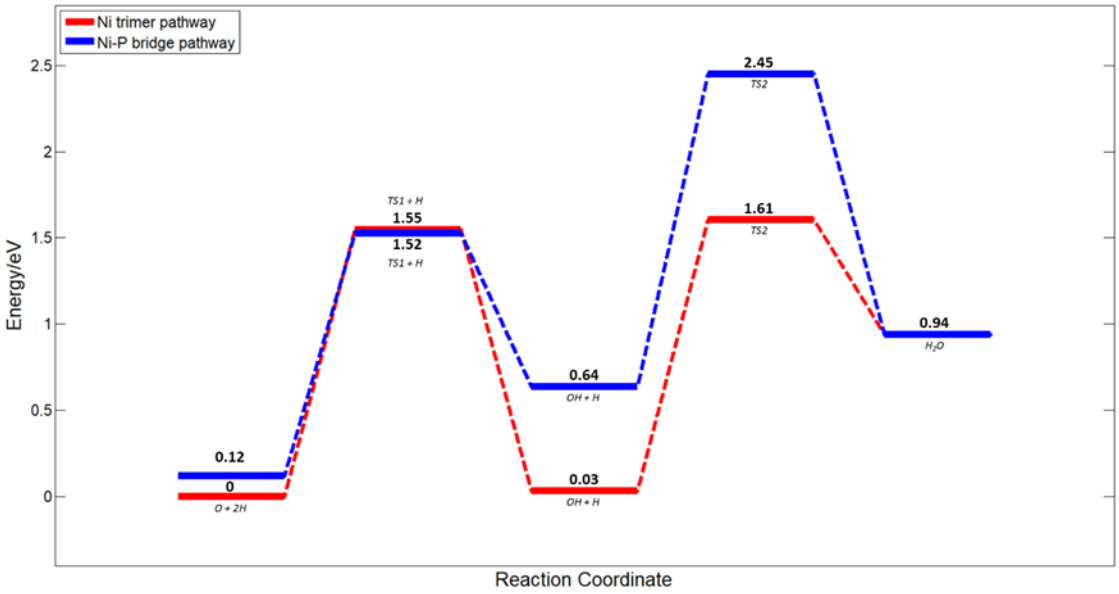

Figure 6-3 a) Reaction profile of water formation via successive hydrogenations of oxygen atom

Which the red line represents the Ni trimer route, and the blue line represents the Ni-P bridge route.

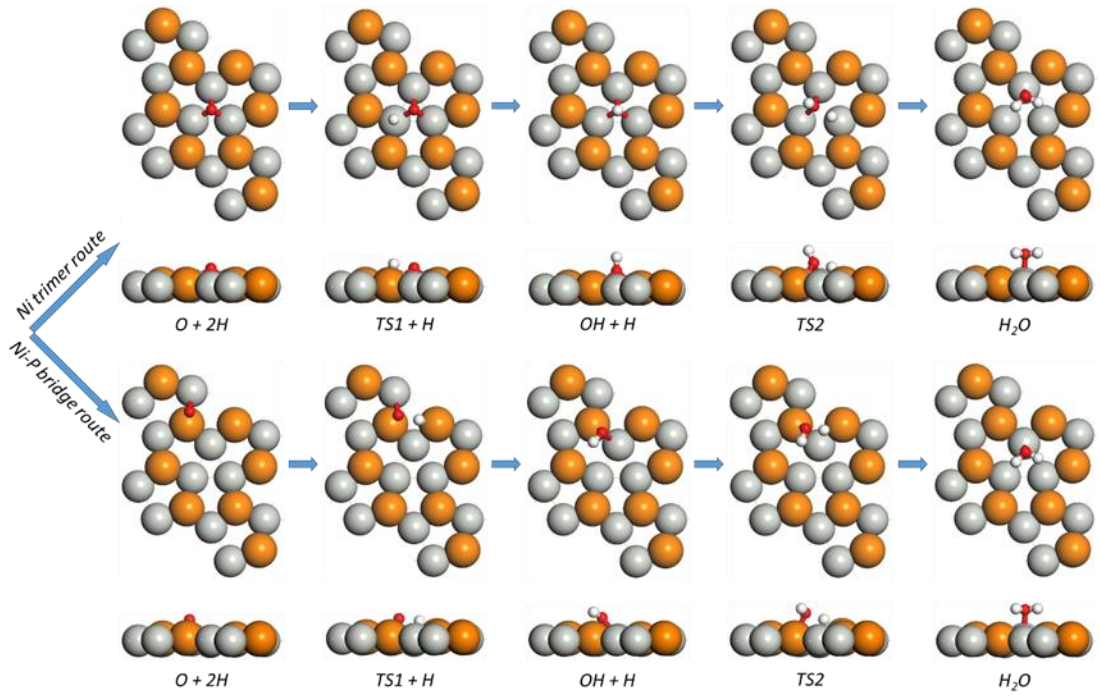

Figure 6-3 b) Mechanisms of successive hydrogenations of oxygen into water

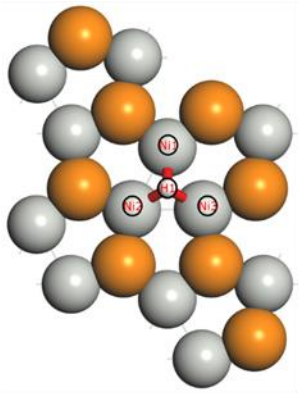

IS(a)

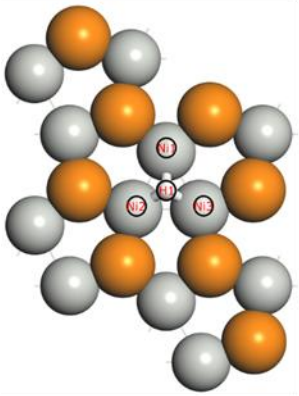

IS(b)

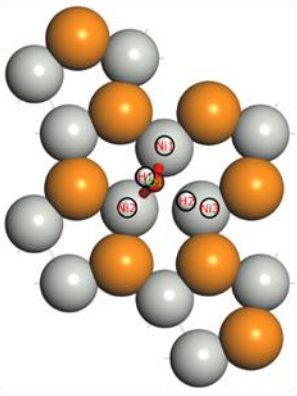

TS

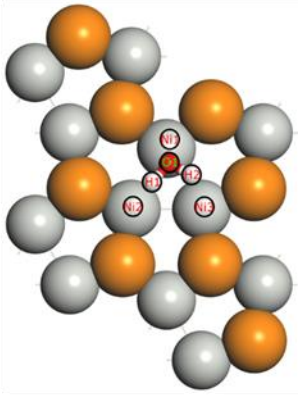

FS

Charge	Ni1	Ni2	Ni3	H1	H2	O1
IS(a)	+0.39	+0.38	+0.39	+1		-1.60
IS(b)	+0.28	+0.25	+0.28	-0.31		
TS	+0.41	+0.40	+0.13	+1	+0.15	-1.54
FS	+0.36	+0.15	+0.16	+1	+1	-1.96

Figure 6-3 c) Charge analysis of the step of hydrogenation of hydroxyl species at Ni trimer site

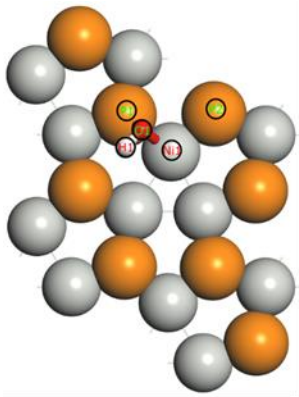

IS(a)

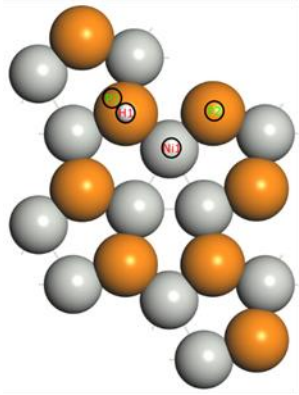

IS(b)

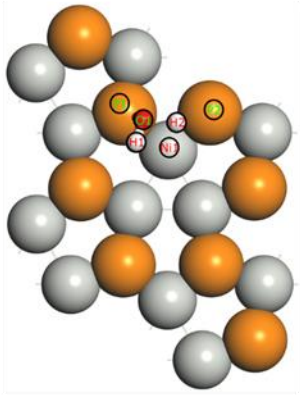

TS

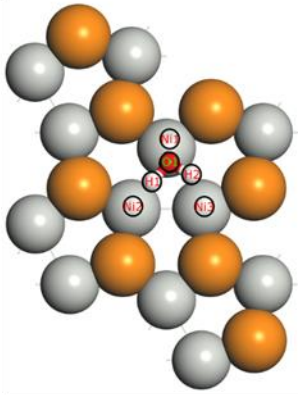

FS

Charge	Ni1	P1	P2	H1	H2	O1
IS(a)	+0.32	+0.64	-0.35	+1		-1.99
IS(b)	+0.18	+0.81	-0.37	-1.07		
TS	+0.16	+0.33	-0.40	+1	+0.26	-1.75
	Ni1	Ni2	Ni3	H1	H2	O1
FS	+0.36	+0.15	+0.16	+1	+1	-1.96

Figure 6-3 d) Charge analysis of the step of hydrogenation of hydroxyl species at Ni-P bridge site

6.3.2.2. Furfuryl alcohol formations via hydrogenations of furfural

As DFT work on Pd suggested that 2-methylfuran was generated via the production of furfuryl alcohol,[112] the hydrogenation of furfural into furfuryl alcohol was calculated. The reaction pathways could be split via either an alkoxide intermediate or a hydroxyalkyl species in the order of hydrogenation. The reaction profile is shown in figure 6-4 a). Both reaction pathways had the similar transition state structures, as the hydrogenations at the carbonyl oxygen and carbon initiated from hydrogens at a P top site and a Ni top site respectively.

6.3.2.2.1. Hydroxyalkyl route

The hydroxyalkyl route started with the hydrogen approached from a P top site. In the transition state, the formed H-O distance was 1.46 Å, the O-Ni bond distance was 2.08 Å, and C-O bond length was 1.36 Å. As the hydroxyalkyl species was generated, the new H-O bond formed at a distance of 0.99 Å. Comparing with the initial state, the O-Ni distance increased from 1.96 Å to 2.26 Å, and the C-O bond length also extended from 1.32 Å to 1.43 Å. When the second hydrogen approached the aliphatic carbon of furfural from a Ni top site, the H-C distance was 1.60 Å, the C-O bond length was 1.41 Å, and the C-C bond distance was 1.45 Å in the transition state. As the furfuryl alcohol was produced, the new C-H bond formed at a distance of 1.11 Å. By comparing with the initial state, the C-O bond increased from 1.43 Å to 1.44 Å, and the C-C bond length also extended from 1.45 Å to 1.49 Å.

6.3.2.2.2. Alkoxide route

The first hydrogenation at the carbonyl carbon was initiated by the hydrogen approached the aliphatic carbon of furfural at a Ni top site with a H-C distance of 1.63 Å in the transition state. The carbonyl C-O bond length was 1.31 Å, and the bond length of aromatic C-aliphatic C was 1.47 Å. The alkoxide intermediate was generated at the final state, in which the new C-H bond had a length of 1.17 Å with the C moved away from the surface. In contrast to the initial state, the C-O bond increased from 1.32 Å to 1.36 Å, and the C-C bond also extended from 1.45 Å to 1.50 Å. The aliphatic oxygen was further attacked by a hydrogen atom at a P top site. In the transition state, the H-O distance was 1.53 Å, while the O-Ni bond length was 1.99 Å, and the C-O distance was 1.40 Å. With the furfuryl alcohol was generated subsequently in the final state, the new H-O bond formed at a length of 0.98 Å. By comparing with the alkoxide initial state, the bond length of O-Ni increased from 1.91 Å to 2.18 Å, while the C-O distance also extended from 1.36 Å to 1.44 Å.

Based on the information of the hydrogenation barriers, it could be expected that the hydrogenation of the carbonyl carbon did not strongly affect the accessibility of the hydrogenation on the carbonyl oxygen (1.15 eV vs 1.19 eV), while the hydrogenation of the carbonyl carbon became more difficult once the oxygen became hydrogenated (1.54 eV vs 1.27 eV), as the oxygen could not further bonding with the surface Ni to stabilise the intermediate. The effective barriers of furfuryl alcohol formation were composed of both the hydrogenation steps regardless of the hydrogenation order, which gave the values of 2.13 eV and 2.17 eV for the hydroxyalkyl route and alkoxide route respectively. Hence,

the hydroxyalkyl route was preferred in the generation of furfuryl alcohol via hydrogenations of furfural.

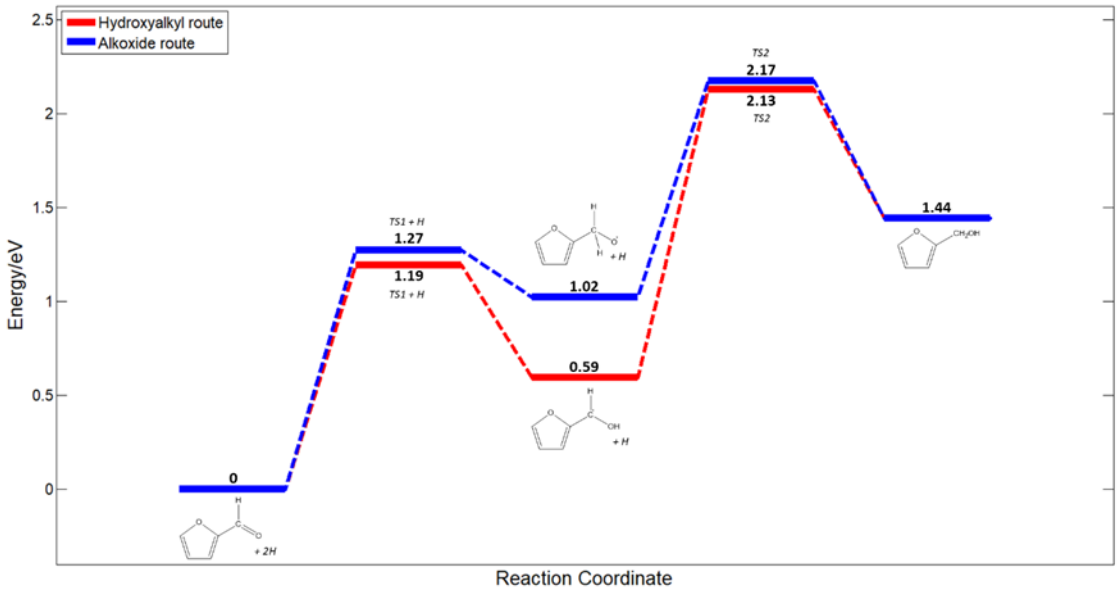

Figure 6-4 a) Reaction profile of furfuryl alcohol formations via successive hydrogenations of furfural

Which the red line represents the hydroxyalkyl route, and the blue line represents the alkoxide route.

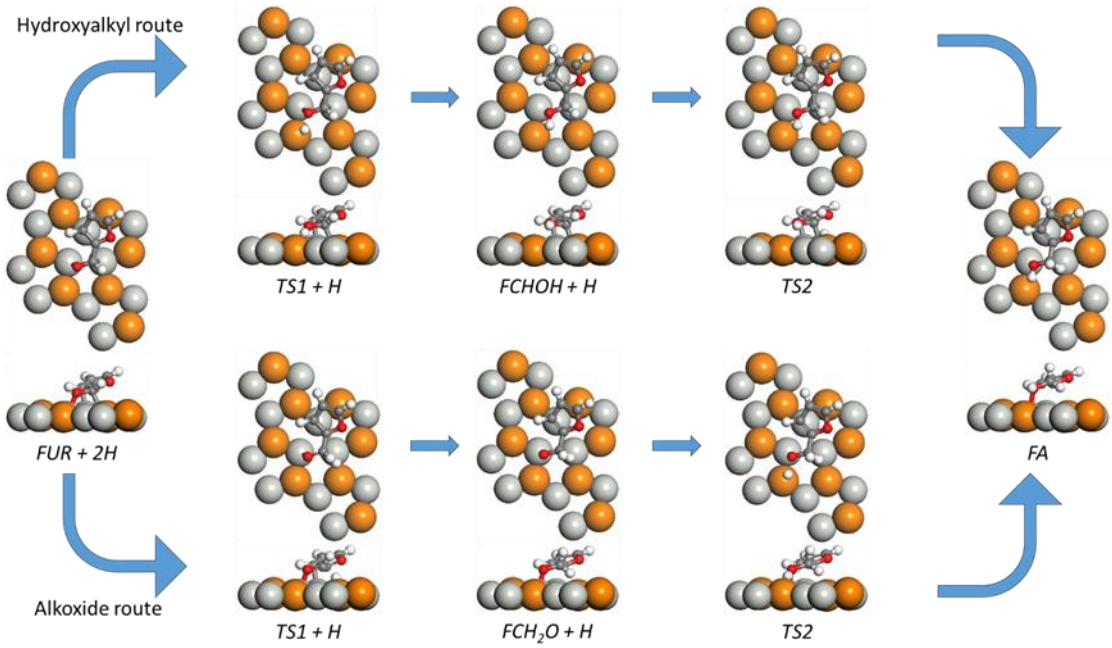

Figure 6-4 b) Mechanisms of furfural conversion to furfuryl alcohol

6.3.2.3. Reaction pathways of 2-methylfuran formation

In the investigation of the 2-methylfuran formation mechanism, four pathways were considered in total, which originated from furfural, alkoxide intermediate, hydroxyalkyl species and furfuryl alcohol respectively. However, 2-methylfuran could not be generated via the alkoxide intermediate pathway from our calculations due to the failure of the C-O bond breaking, as the aliphatic carbon was not activated by the surface atoms. The pathways were presented in the order of successive hydrogenations before the C-O bond cleavage, which means pathway 1 via the production of furfuryl alcohol, pathway 2 via the hydroxyalkyl species, and pathway 3 directly from furfural. All these pathways had the same products of 2-methylfuran and water generated at the end. Because the cleavage of the key C-O bond occurred at different locations on the Ni_3P_2-termination surface, different

water formation routes were allocated to all three pathways which means the water formation via Ni trimer route was incorporated into pathway 1, and the water formation via Ni-P bridge route was incorporated into pathway 2 and 3 respectively.

6.3.2.3.1. Direct cleavage of OH functional group from furfuryl alcohol

Route 1 initiated with the direct cleavage of the C-OH bond at the beginning, followed by successive hydrogenations of the furyl-CH_2 and OH intermediates separately. The reaction mechanism is shown in figure 6-5.

In order to cleave the C-OH bond of furfuryl alcohol, the furfuryl alcohol has to be diffused to a position which the adsorption of it is mainly attributed through the ring carbon atoms, the geometry is shown in 6-5. In the first step, the C-O bond stretched to 2.02 Å in the transition state, the resulted C-C bond was 1.40 Å, and the Ni-O distance was 1.95 Å. As the furyl-CH_2 intermediate was generated via the complete cleavage of the C-O bond, OH species diffused away and adsorbed at an adjacent Ni-trimer site. Comparing the initial and final states, the C-C bond length decreased from 1.51 Å to 1.47 Å. The furyl-CH_2 intermediate was then attacked by a hydrogen atom at a P top site, and in the transition state the H-C distance was 1.83 Å, while the C-C bond length was 1.37 Å. When the 2-methylfuran was produced, the new H-C bond formed with a distance of 1.10 Å, and the C-C bond length extended from 1.47 Å in the initial state to 1.48 Å.

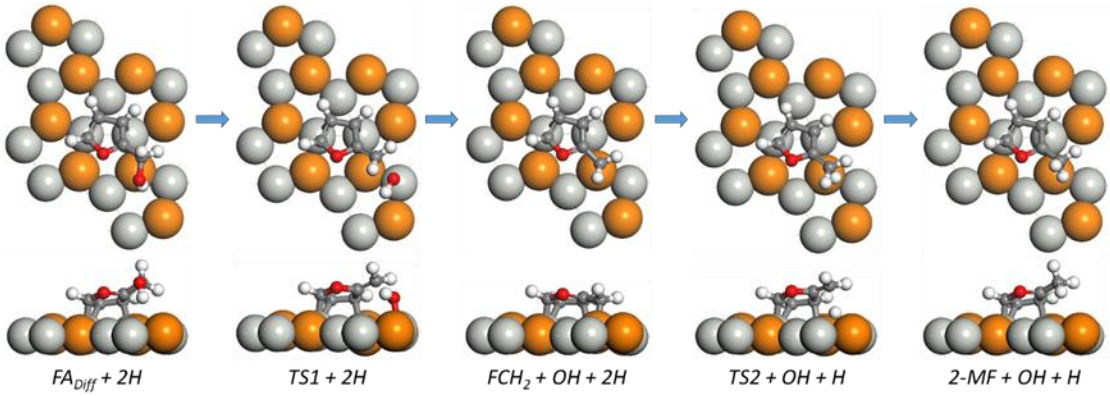

Figure 6-5 Mechanism of 2-methylfuran formation via direct cleavage of C-OH bond of furfuryl alcohol

6.3.2.3.2. Cleavage of OH functional group from hydroxyalkyl species

Route 2 originated from the C-OH bond breaking of the hydroxyalkyl species, followed by successive hydrogenations of the furyl-CH and OH intermediates separately. The reaction mechanism is shown in figure 6-6.

In the first step, the C-OH bond stretched to 1.98 Å, the resulted C-C bond was 1.45 Å, and the Ni-O distance was 1.97 Å in the transition state, which yielded furyl-CH and OH species as products. Contrast to the initial state, at the final state the C-C bond contracted from 1.45 Å to 1.44 Å, and the Ni-O bond shortened from 2.26 Å to 2.03 Å at the Ni trimer site. The generated furyl-CH intermediate was then attacked by a hydrogen atom from a top site of Ni atom, and in the transition state the H-C distance was 1.96 Å and the C-C bond length 1.45 Å. The new H-C bond was formed at 1.10 Å as the furyl-CH_2 was produced. Then the furyl-CH_2 intermediate was attacked by a hydrogen atom from a Ni bridge site, and in the transition state the H-C distance was 1.54 Å, while the C-C bond

length was 1.46 Å. When the 2-methylfuran was produced, the new H-C bond formed with a distance of 1.10 Å, and the C-C bond length extended from 1.43 Å in the initial state to 1.49 Å.

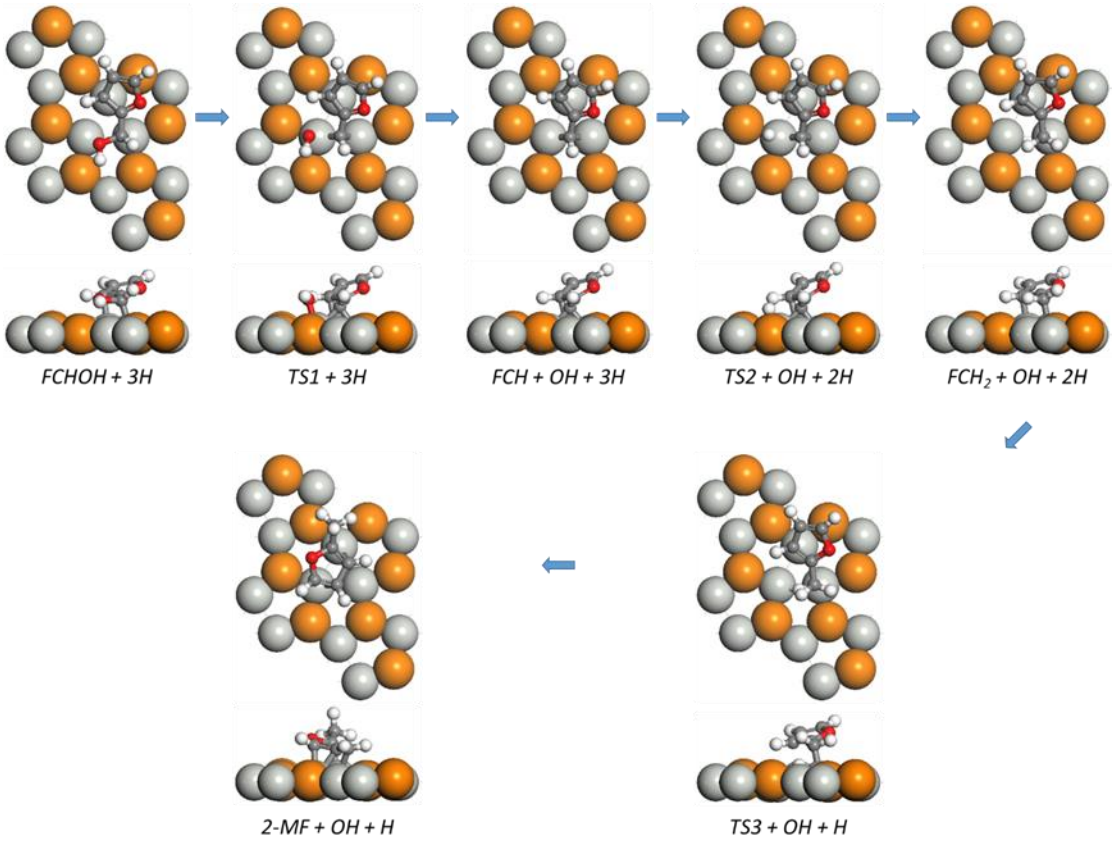

Figure 6-6 Mechanism of 2-methylfuran formation via the cleavage of C-OH bond of hydroxyalkyl intermediate

6.3.2.3.3. Direct C-O cleavage from the furfural

Figure 6-7 shows the mechanism of route 3, which started from the direct cleavage of the carbonyl bond of furfural, followed by successive hydrogenations of the resultant furyl-CH and O intermediates separately.

During the C-O bond rupture, the C-O bond lengthened to 2.03 Å in the transition state, while the resulted C-C bond length was 1.44 Å and the Ni-O distance was 2.05 Å. Comparing with the initial state, the C-C bond length decreased from 1.45 Å to 1.44 Å, and the Ni-O distance increased from 1.96 Å to 2.05 Å in the Ni-P bridge site at the final state. Then, furyl-CH and oxygen atom were generated. The successive hydrogenations of furyl-CH intermediate were described in route 2 (see 6.3.2.3.2.).

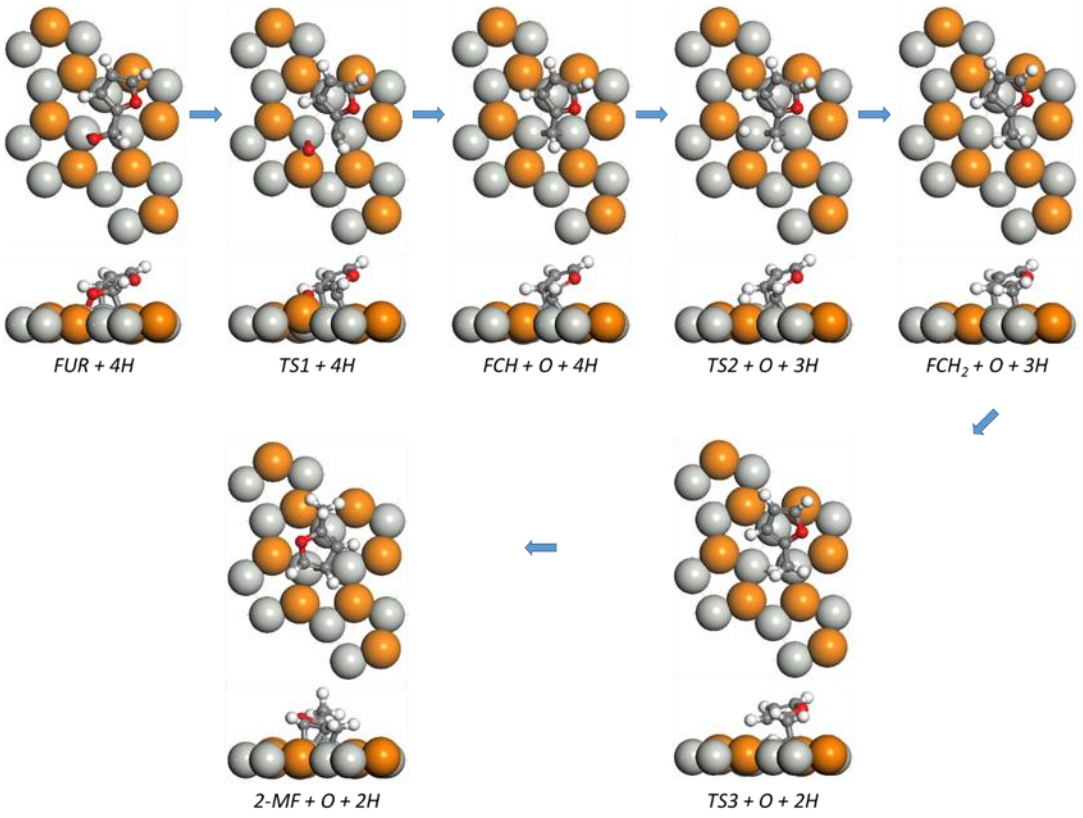

Figure 6-7 Mechanism of 2-methylfuran formation via the direct cleavage of C-O bond of furfural

The reaction profile of all three pathways for 2-methylfuran formation is shown in figure 6-8 a). Based on the comparison of the relative energies of the final states, it was obvious that pathways 2 and 3 were 0.14 eV more thermodynamically favoured over pathway 1, which came from the water formation at Ni-P bridge site rather than at Ni-trimer site. The rate determining step of all these 3 pathways were the hydrogenations of the hydroxyl species to water, with the barrier values of 1.57 eV for pathway 1, and 1.81 eV for pathway 2 and 3 respectively, which indicated that pathway 1 should be favoured if only the rate determining step was considered. However, when the whole reaction scheme was taken into account, the stability of the hydroxyalkyl intermediate became important. The reaction preferred to cleave the C-OH bond when FCHOH was generated rather than hydrogenation on the carbonyl carbon, hence pathway 2 was promoted. Furthermore, there was a diffusion step of the furfuryl alcohol in pathway 1 for the following reactions to carry out. However, this step was likely to be difficult under the real experimental condition due to the high surface coverage of the reactant species, which made pathway 1 further inhibited. By comparing pathways 2 and 3, despite the rate determining step was the same, the initial direct cleavage of the carbonyl bond was more kinetically hindered than the hydrogenation at the carbonyl oxygen (1.43 eV vs 1.19 eV). Once the carbonyl bond was broken, the FCH intermediate and oxygen on the catalyst surface were too stable to proceed the further hydrogenations, which resulted in a higher effective barrier than that in pathway 2. The effective barriers were determined by steps of hydrogenations of furfural to furfuryl alcohol for pathway 1, hydrogenation steps of the FCH intermediate and hydroxyl species for pathway 2, and all four hydrogenation steps of the FCH intermediate and oxygen for pathway 3, which contributed to the barrier values of 2.13 eV, 1.94 eV and 2.47 eV

respectively. Therefore, it was clear that the pathway 2 was the best reaction pathway to generate 2-methylfuran from furfural which is represented by the blue pathway in figure 6-8 a), it also means the furfuryl alcohol was not a necessary intermediate for the 2-methylfuran formation.

Additionally, the effect of hydrogenations on the carbonyl bond to the C-O bond rupture was also investigated, with the kinetic barriers for these step were found to be 1.43 eV for furfural, 1.21 eV for the hydroxyalkyl intermediate, and 0.77 eV for the furfuryl alcohol respectively. Hence, it was obvious that the hydrogenations on the carbonyl bond could facilitate the bond breaking of C-O. Moreover, as the C-O bond cleavage of furfuryl alcohol was achieved on the phosphorus, the charge analysis was also performed, which is shown in figure 6-8 b), c) and d). However, the charge of the phosphorus was not changed too much based on our results, and therefore the phosphorus may not be a crucial factor to promote the C-O bond cleavage.

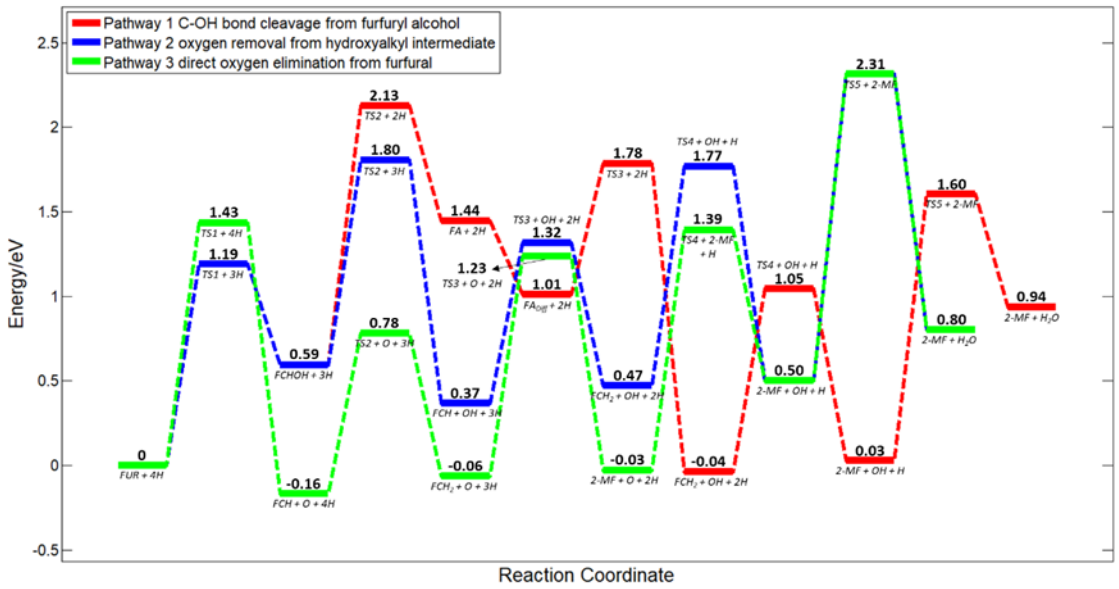

Figure 6-8 a) Reaction profile of 2-methylfuran formations

Which the red line represents the pathway 1 that the 2-methylfuran is generated from hydrogenolysis of furfuryl alcohol, the blue line represents the pathway 2 that the 2-methylfuran is generated from C-O bond cleavage of the hydroxyalkyl intermediate, and the green line represents the pathway 3 that the 2-methylfuran is generated from direct oxygen elimination of furfural respectively.

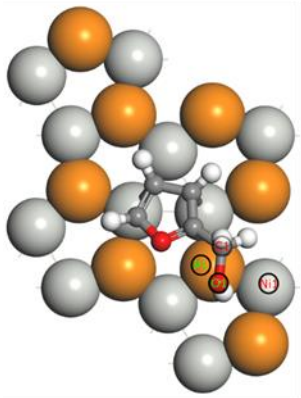

IS

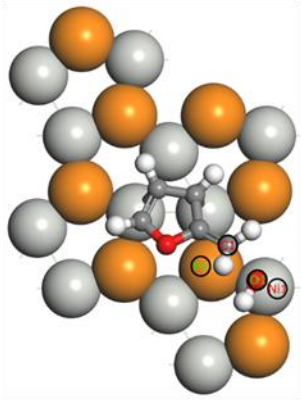

TS

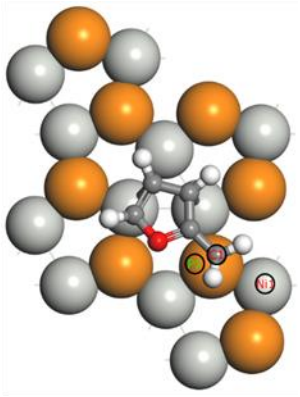

FS(a)

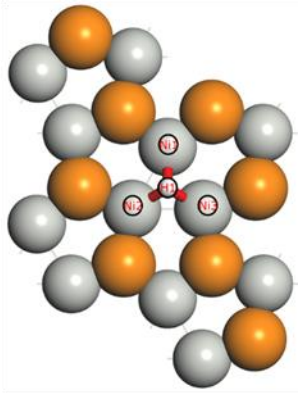

FS(b)

Charge	Ni1	P1	C1	O1	
IS	+0.18	-0.40	+0.81	-1.83	
TS	+0.42	-0.31	+0.21	-1.43	
FS(a)	+0.15	-0.01	-0.24		
	Ni1	Ni2	Ni3	H1	O1
FS(b)	+0.39	+0.38	+0.39	+1	-1.60

Figure 6-8 b) Charge analysis of the C-OH cleavage step in pathway 1

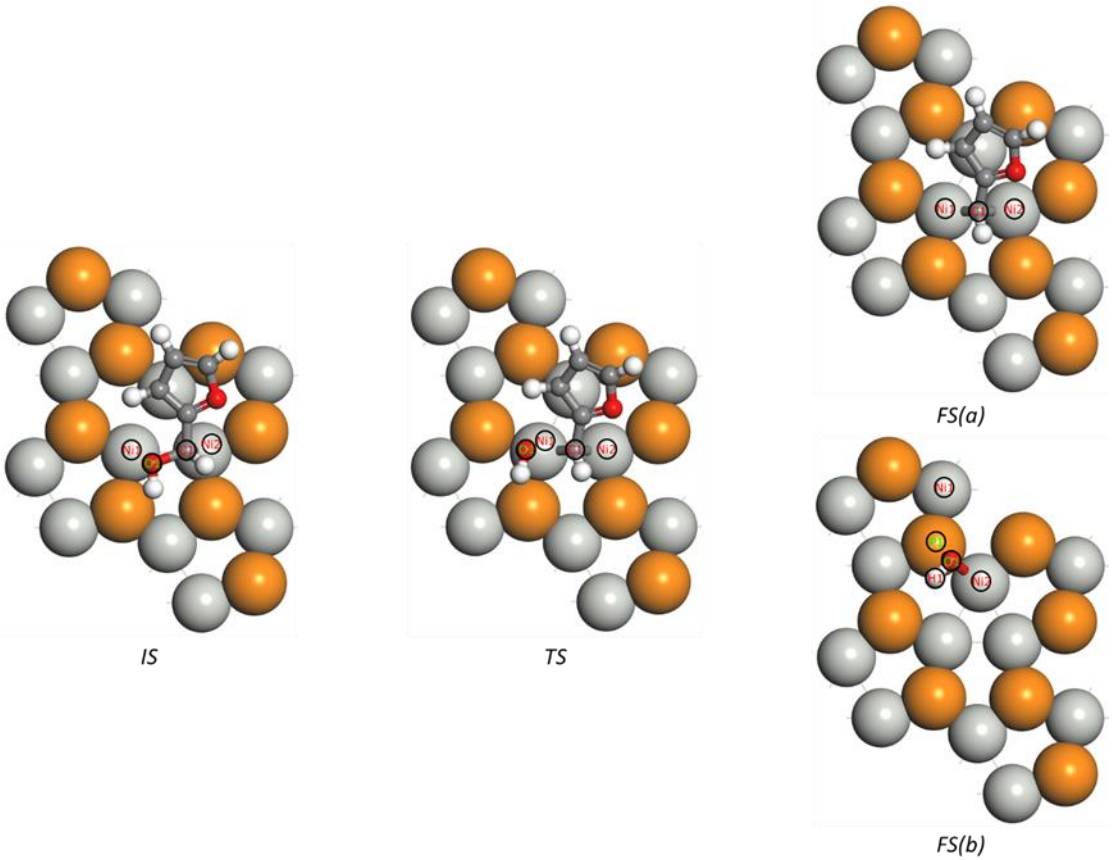

Charge	Ni1	Ni2	C1	O1	
IS	+0.32	+0.31	+0.51	-1.74	
TS	+0.49	+0.31	-0.15	-1.39	
FS(a)	+0.34	+0.33	-0.37		
	Ni1	Ni2	P1	H1	O1
FS(b)	+0.20	+0.32	+0.64	+1	-1.99

Figure 6-8 c) Charge analysis of the C-OH cleavage step in pathway 2

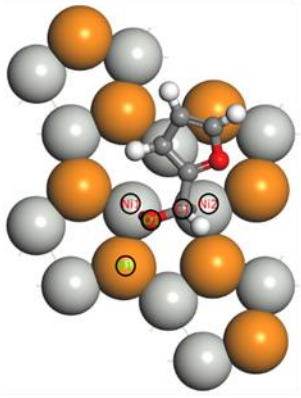

IS

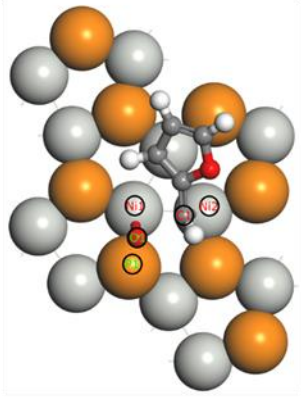

TS

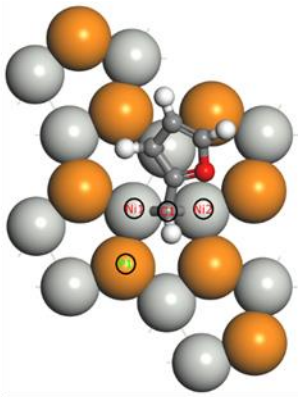

FS(a)

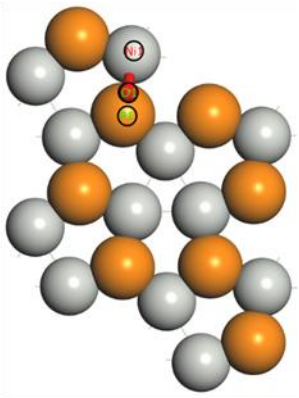

FS(b)

Charge	Ni1	Ni2	P1	C1	O1
IS	+0.42	+0.29	-0.30	+1.22	-1.68
TS	+0.31	+0.33	+1.22	-0.17	-1.77
FS(a)	+0.34	+0.33	-0.32	-0.37	
	Ni1	P1	O1		
FS(b)	+0.38	+1.25	-1.82		

Figure 6-8 d) Charge analysis of the C-O cleavage step in pathway 3

6.3.2.4. The concern of decarbonylation pathway of furfural

As there was another key compound, furan, which was shown to be the thermodynamically favourable product on Pd(111) and Pt(111),[110, 112] the decarbonylation pathway was also tried on the Ni_3P_2-termination surface. However, due to the adsorption configuration of furfural, the C-C bond could not be cleaved from our calculations. Because Jiménez-Gómez et al. detected the furan as a minor product on Ni_2P catalysis,[102] one may consider that it may work on the relatively unstable surface of $Ni_2P(0001)$ facet, which was the Ni_3P_1-termination surface that allowed the decarbonylation of furfural. This pathway initiated from the rupture of the aliphatic C-H bond, followed by the breaking of the C-C bond, and finally the rehydrogenation to form an aromatic C-H bond. Overall, the products were furan and carbon monoxide. The reaction profile and detailed mechanisms are shown in figure 6-9 a) and b).

In the transition state of the first step hydrogenation, the aliphatic C-H bond stretched from 1.10 Å to 1.62 Å with the H bonded to a top site of Ni, while the C-O bond length was 1.26 Å, and the C-C bond distance was 1.43 Å. As the furyl-CO intermediate was generated via the rupture of the C-H bond, the hydrogen atom diffused away resulted in an adsorption at a rear Ni trimer site. The decarbonylation was further achieved via the C-C bond stretched to 1.85 Å in the transition state, with the resulted CO bond at a distance of 1.20 Å. The furyl intermediate was produced after the C-C bond breaking and the carbon monoxide diffused away, which leading to adsorb at a Ni top site vertically via its carbon. Comparing with the initial state, the C-O bond length reduced from 1.26 Å to 1.16 Å. Finally, the hydrogen approached the aromatic carbon at a Ni top site, and the H-C distance was 1.71

Å in the transition state. When the furan was generated, the new H-C bond formed at a distance of 1.09 Å.

Our calculations demonstrated that the decarbonylation pathway could be achieved on the Ni_3P_1-termination surface. However, due to the low abundance of this surface,[194] the decarbonylation pathway was not favoured in the whole reaction mechanism. In order to get better understand the reason why the pathway was prohibited, the charge analysis of the adsorption geometries of furfural on Ni_3P_1-termination and Ni_3P_2-termination surface was computed and shown in figure 6-9 c). Both the carbons that involved in the C-C bond cleavage had similar reduced positive charges compared to those in gas phase of furfural, which indicated that the activation of these carbons by surface Ni atoms were almost the same on these two surfaces. Additionally, as the P/Ni ratio in Ni_2P increased, the Ni possessed less partial positive charges, which should be more likely to donate the electron density to the carbons of furfural to facilitate the C-C bond cleavage. However, the furan could not be generated on the Ni_3P_2-termination surface, which indicated that the main factor to dominate the decarbonylation mechanism came from the geometry of the surface. Due to the lower composition of phosphorus on the Ni_3P_1-termination than Ni_3P_2-termination surface, the Ni atoms provided a planar adsorption of furfural similar to Pd(111),[112] Pt(111),[110] and Ru(0001),[113] which promoted the decarbonylation reaction.

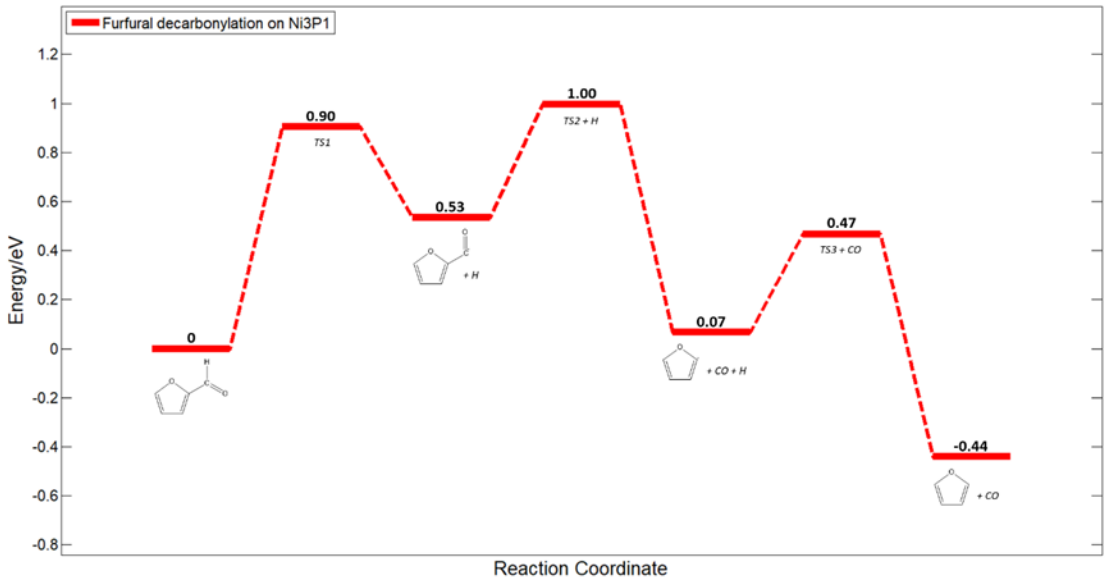

Figure 6-9 a) Reaction profile of furan formation via the decarbonylation of furfural on Ni_3P_1-termination surface

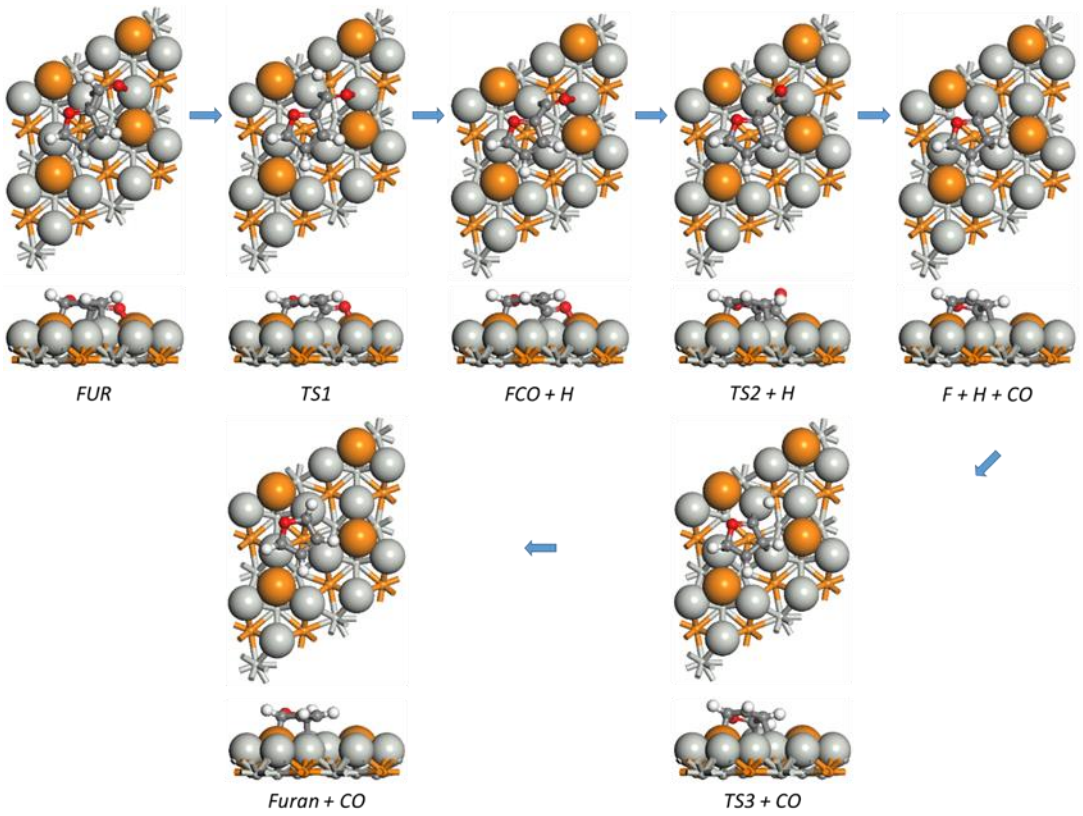

Figure 6-9 b) Mechanism of furan formation via the decarbonylation of furfural on Ni_3P_1-termination surface

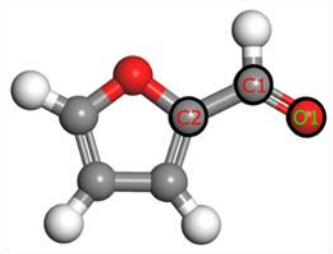

FUR(g)

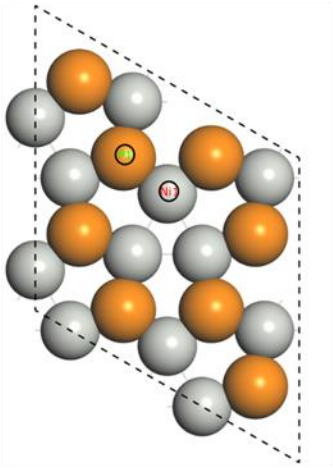

Ni_3P_2-termination

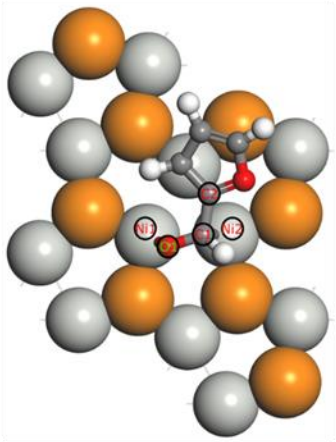

FUR adsorption on Ni_3P_2-termination

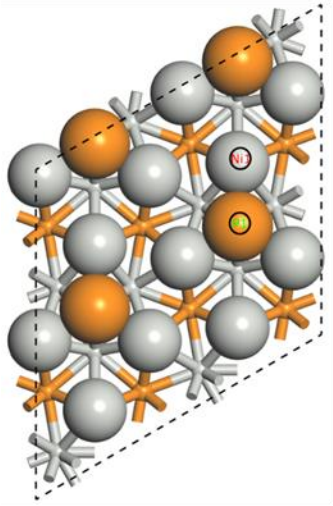

Ni_3P_1-termination

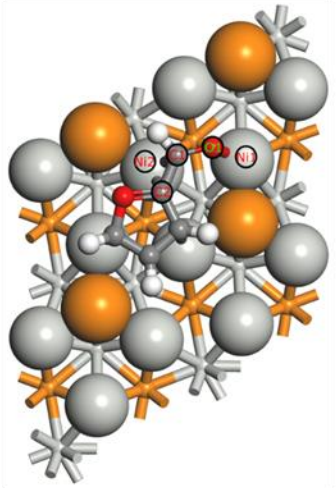

FUR adsorption on Ni_3P_1-termination

Charge	Ni1	P1			
Ni_3P_2 termination	+0.21	-0.37			
Ni_3P_1 termination	+0.25	-0.46			
	Ni1	Ni2	C1	C2	O1
FUR gas			+1.79	+0.42	-1.81
FUR ad Ni_3P_2	+0.42	+0.29	+1.22	+0.63	-1.68
FUR ad Ni_3P_1	+0.49	+0.35	+1.27	+0.71	-1.75

Figure 6-9 c) Charge analysis of furfural adsorption geometries on Ni_3P_2 and Ni_3P_1 termination surfaces

6.3.2.5. The by-products production (difurfuryl ether, 2-methyltetrahydrofuran, and 2-pentanone)

It was shown in the experimental work of Wang et al,[103] which the difurfuryl ether, 2-methyltetrahydrofuran and 2-pentanone were detected as by-products, these by-products came from the dimerisation, ring saturation and ring opening reactions respectively.

6.3.2.5.1. Production of difurfuryl ether

The difurfuryl ether formation was achieved via the migration of furyl-CH_2 group of a furfuryl alcohol to its relative alkoxide intermediate. However, these components needed to change their adsorption conformations to the vertical patterns with only their aliphatic oxygens binding to the surface Ni atoms. The adsorption geometry of difurfuryl ether on Ni_3P_2-termination surface is shown in figure 6-10 a).

The distance between the aliphatic oxygen of alkoxide intermediate and the aliphatic carbon of furyl-CH_2 group was 2.09 Å in the transition state, once the dimerisation was completed, the new formed C-O bond was 1.46 Å, and the left hydroxyl group of furfuryl alcohol was diffused to the Ni-trimer site with a following hydrogenation to water molecule which the step was described in section 6.3.2.1.1.

Based on our reaction profile that is shown in figure 6-10 b), the dimerisation step had a moderate reaction barrier of 1.27 eV, which was easier than the hydrogenation of the by-product hydroxyl species at the Ni trimer site with a barrier of 1.58 eV. It was found that this dimerisation reaction could not be achieved without the participation of the surface phosphorus atoms, which may be attributed to the acidic sites originated from the phosphorus that catalysed the dimerisation reaction.[199] This was consistent with the experimental results of Wang et al,[103] which showed that an increase of the proportion of phosphorus in Ni_2P could facilitate the production of difurfuryl ether. In order to further understand this reaction, a charge analysis was performed and shown in figure 6-10 d). However, there was no important clues that could be extracted from the data. Additionally,

with the consideration of a positive adsorption energy at the given reaction temperature (E_{ads} = 0.65 eV), the difurfuryl ether should desorb from the surface directly and could not be converted into 2-methylfuran.

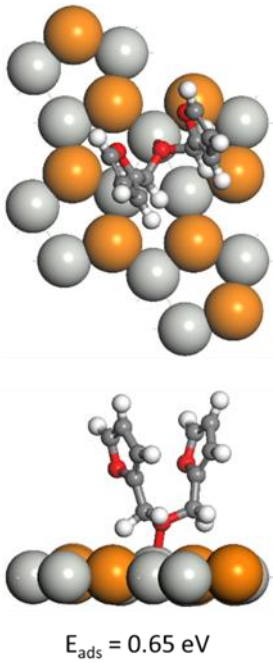

Figure 6-10 a) Adsorption geometry of difurfuryl ether on Ni_3P_2-termination surface

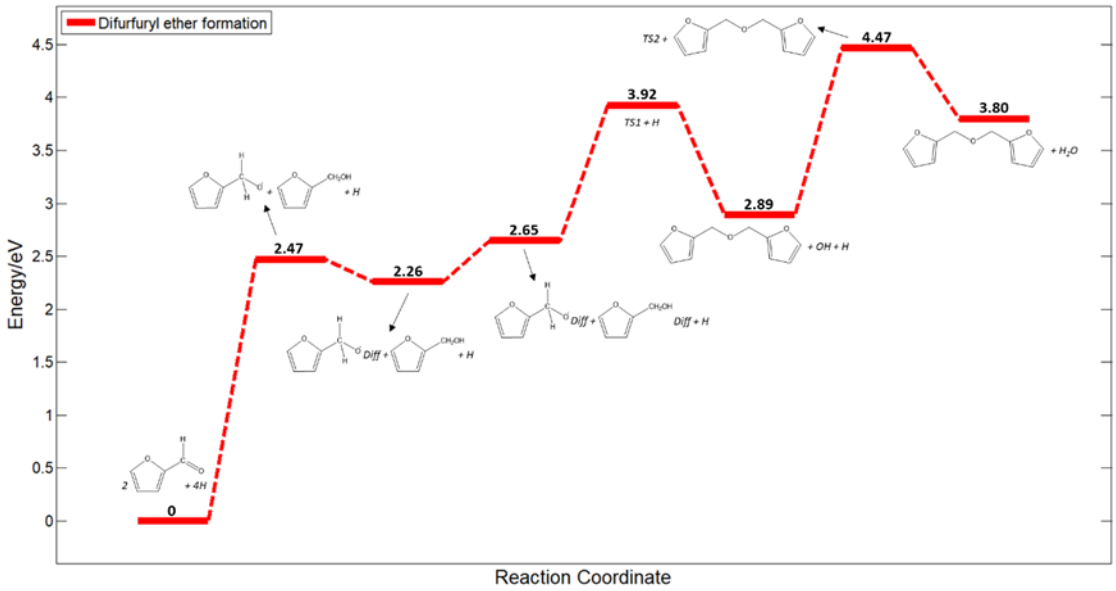

Figure 6-10 b) Reaction profile of difurfuryl ether formation from furfural

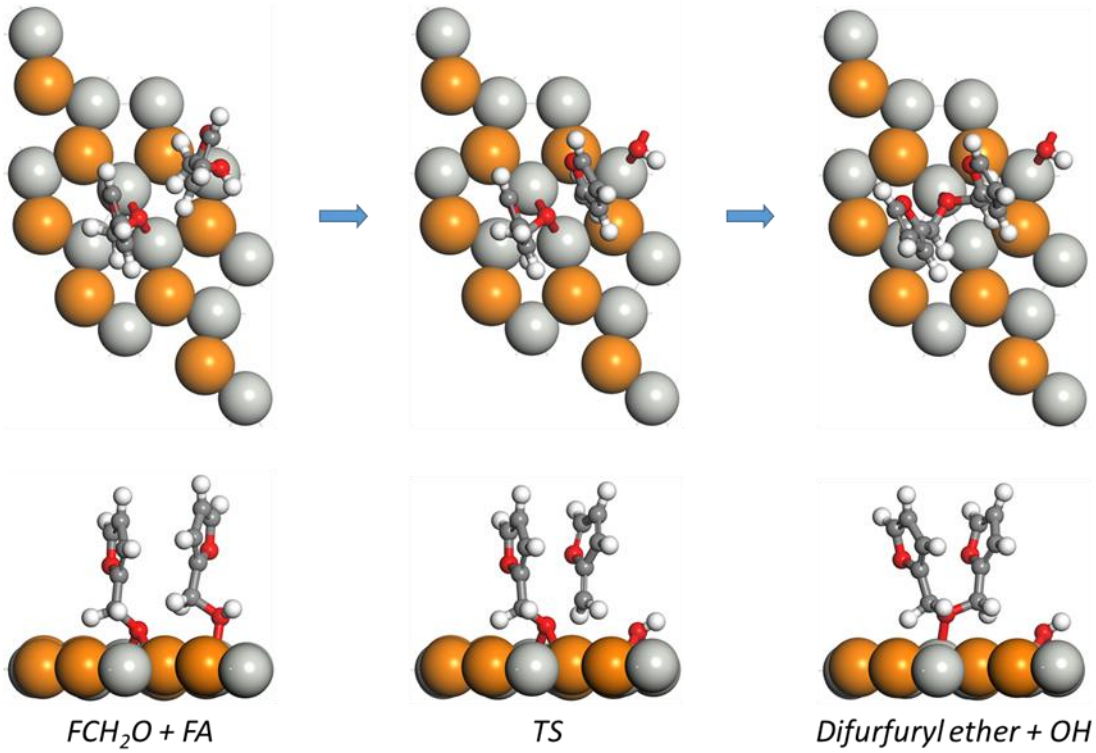

Figure 6-10 c) Mechanism of difurfuryl ether formation

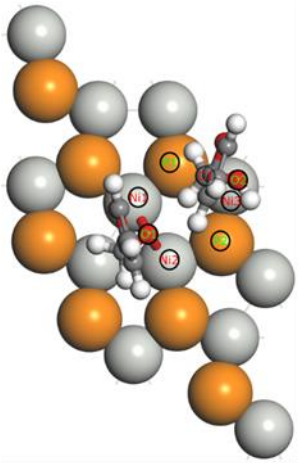

IS

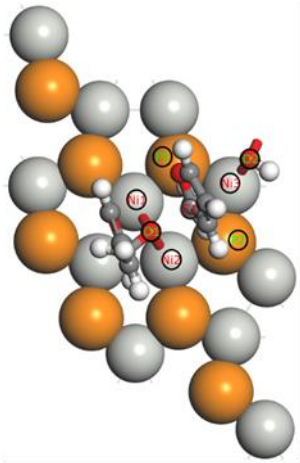

TS

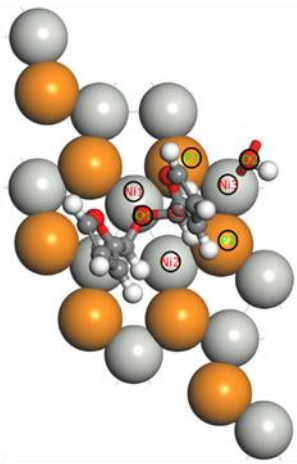

FS

Charge	Ni1	Ni2	Ni3	P1	P2	C1	O1	O2
IS	+0.42	+0.41	+0.38	-0.36	-0.35	+0.37	-1.30	-1.59
TS	+0.38	+0.37	+0.40	-0.37	-0.38	+0.21	-1.15	-1.56
FS	+0.37	+0.19	+0.41	-0.35	-0.38	+0.53	-1.37	-1.55

Figure 6-10 d) Charge analysis of the dimerisation step

6.3.2.5.2. Hydrogenations of 2-methylfuran to 2-methyltetrahydrofuran

The generation of the 2-methyltetrahydrofuran was achieved via four successive hydrogenations on the furyl ring of 2-methylfuran, which the hydrogenation order initiated from the less hinder alpha carbon, then followed by adjacent beta, the other beta, and the methyl-hindered alpha carbon. The reaction profile and mechanism are shown in figure 6-11. After each hydrogenation step, the corresponding saturated carbon was repelled from the Ni_3P_2 surface, which made the adsorption geometry was absent for 2-methyltetrahydrofuran.

The first hydrogenation started with a hydrogen approached the alpha carbon on the same adsorbed Ni atom. In the transition state, the H-C distance was 1.50 Å, and the C-Ni bond distance was 2.12 Å. Then the second hydrogenation on the adjacent beta carbon was also initiated by a hydrogen adsorbed on the same Ni atom as the target carbon, the H-C distance was 1.62 Å, and the C-Ni bond length was 2.13 Å in the transition state. The third hydrogenation was achieved via the other beta-carbon attacked by a hydrogen on a Ni bridge site. In the transition state, the H-C distance was 1.46 Å, and the C-Ni bond distance was 2.21 Å. finally, the last hydrogenation initiated from a hydrogen located at a Ni-top site, which was beneath the hindered alpha carbon, the H-C length was 1.86 Å in the transition state. All of these new formed H-C bonds were 1.10 Å in their relative final states.

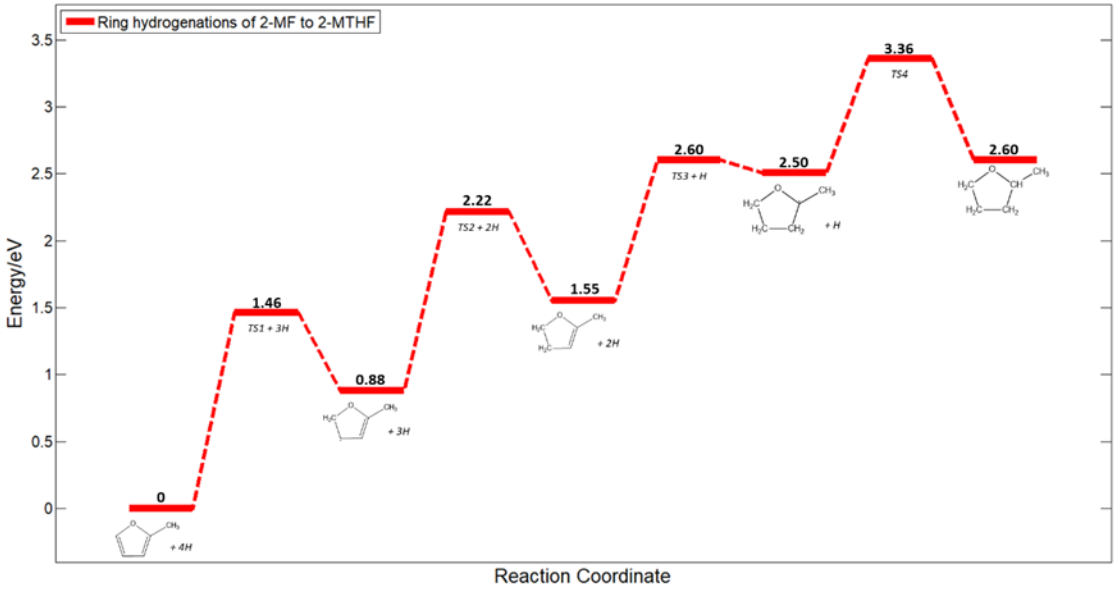

Figure 6-11 a) Reaction profile of 2-methyltetrahydrofuran formation via the successive hydrogenations of 2-methylfuran

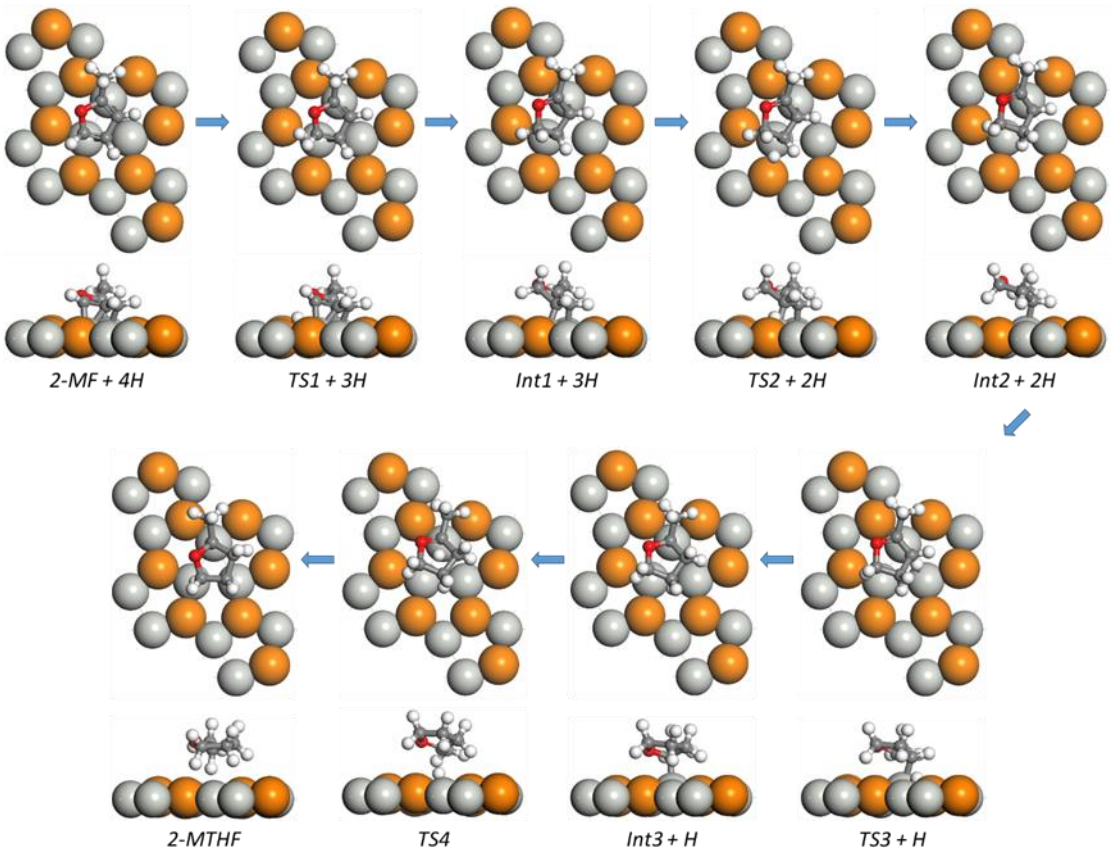

Figure 6-11 b) Mechanism of 2-methyltetrahydrofuran formation via successive hydrogenations of 2-methylfuran

6.3.2.5.3. Conversion of 2-methylfuran to 2-pentanone

The 2-pentanone was generated via the first cleavage of the ring C-O bond between the less hindered carbon and the oxygen, followed by successive hydrogenations on the carbons. Like the saturated carbons of 2-methyltetrahydrofuran, once the hydrogenation steps were completed, the saturated carbon was repelled from the Ni_3P_2-termination surface. The adsorption geometry and reaction profile are shown in figure 6-12 a) and b) respectively.

The C-O bond stretched from 1.39 Å to 2.19 Å in the transition state, this step also increased distance between the resultant carbonyl carbon and the Ni atom from 2.21 Å to 2.71 Å. When the C-O bond breaking was completed, the resultant terminal carbon was adsorbed at a Ni bridge site, and the carbonyl group was tilted away from the surface. The following hydrogenation happened at the alpha carbon related to the carbonyl group, which the hydrogen approached the carbon on the same adsorbed Ni atom. The H-C distance was 1.52 Å in the transition state, and the Ni-C bond length was 2.16 Å respectively. The new forming H-C bond was 1.13 Å in the final state. Then the second hydrogenation was operated on the beta carbon with a hydrogen also adsorbed on the same Ni atom, the H-C distance was 1.64 Å and the Ni-C bond length was 2.22 Å in the transition state. The formed H-C bond was 1.11 Å in the final state. The last two hydrogenations were targeted on the terminal unsaturated gamma carbon, the H-C distance were 1.90 and 1.76 Å in the transition states relatively, and the formed H-C bonds were 1.10 and 1.13 Å respectively in their final states.

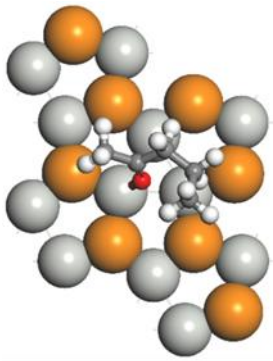

E_{ads} = 0.17 eV

Figure 6-12 a) Adsorption geometry of 2-pentanone on Ni_3P_2-termination surface

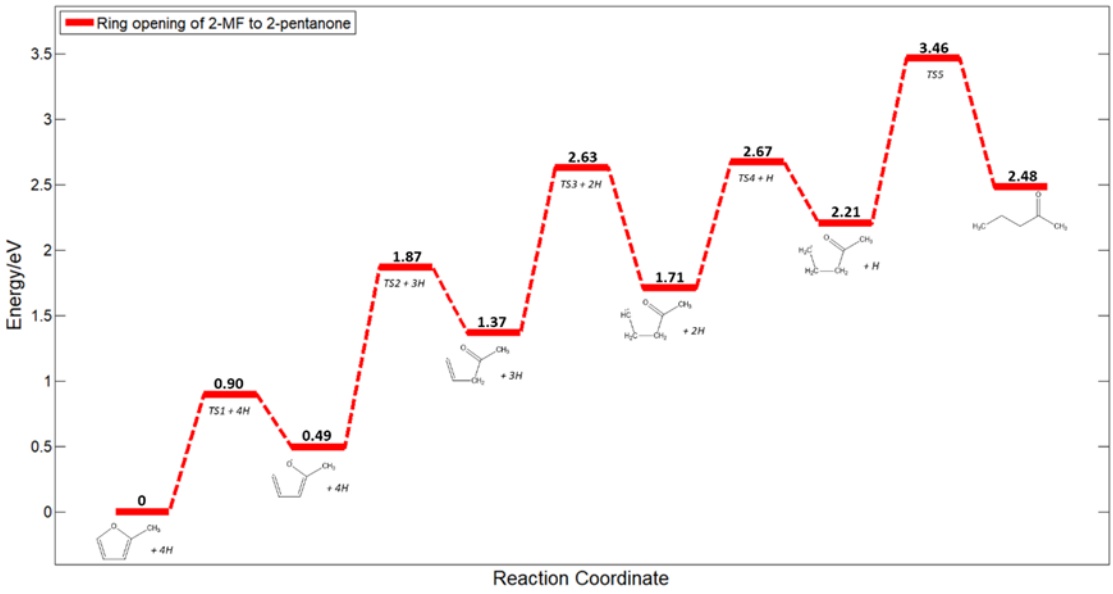

Figure 6-12 b) Reaction profile of 2-pentanone formation from 2-methylfuran

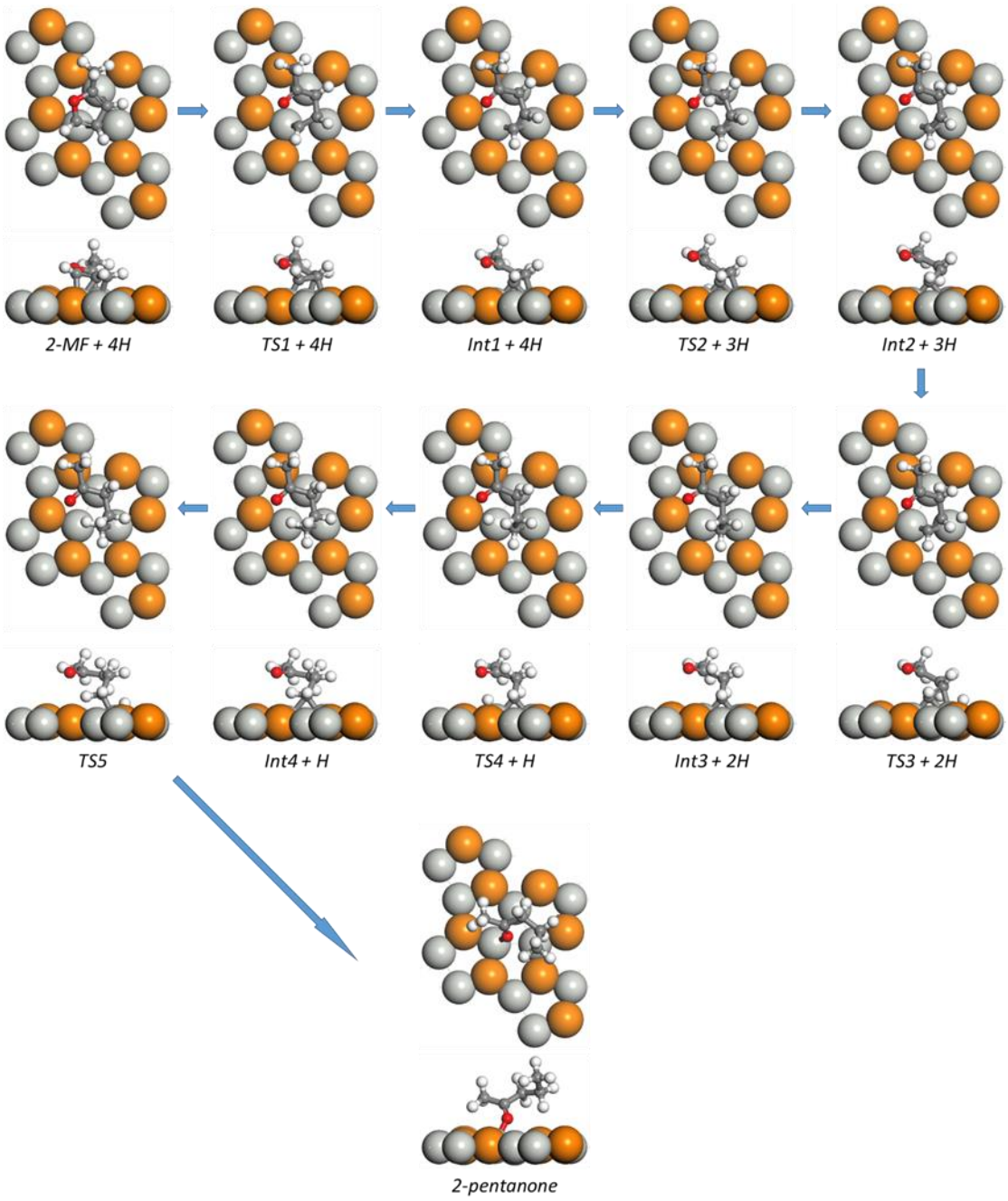

Figure 6-12 c) Mechanism of 2-pentanone formation from 2-methylfuran

Based on the determination of the effective barriers, all of the reaction steps were involved in 2-methyltetrahydrofuran and 2-pentanone pathways, which gave the barrier values of

3.36 eV in figure 6-11 a) and 3.46 eV in figure 6-12 b), respectively. This indicated that the formation of 2-methyltetrahydrofuran was slightly kinetically favoured over the production of 2-pentanone, which coincided with the experimental results of Wang et al,[103] as there was a higher yield of 2-methyltetrahydrofuran detected than the 2-pentanone. Beyond this, there would be a higher surface coverage of hydrogen under the experimental condition, which occupied the adjacent sites to promote the hydrogenations on 2-methylfuran, and provided further steric hindrance for the ring-open step of 2-methylfuran. Moreover, because the calculated adsorption strength of 2-methylfuran was quite small (-1.06 eV) in comparison with other DFT calculation results on Pd(111) and Re/Pt bimetallic surfaces,[112, 200] this strength would be even smaller under the reaction condition, which led to the selectivities of 2-methylfuran and 2-pentanone were very low.[103]

6.4. Conclusions

Detailed density functional theory calculations of furfural conversions at 513 K on the $Ni3P_2$-termination surface were carried using the PBE-D3 functional, and the following results are achieved:

1) The water formation via the successive hydrogenation of oxygen-related species was easier to proceed at Ni trimer site than the Ni-P bridge site.

2) The generation of furfuryl alcohol from furfural hydrogenations was preferred via the hydroxyalkyl intermediate pathway. However, it was not a necessary intermediate for the formation of the main product 2-methylfuran.

3) 2-methylfuran was generated via the hydrogenation of the carbonyl oxygen of furfural first, followed by the cleavage of the C-OH bond and successive hydrogenations of the FCH intermediate.

4) Based on a higher composition ratio of P/Ni, the most stable adsorption geometry of furfural was changed from ring adsorption on the Ni_3P_1-termination surface to carbonyl group adsorption on Ni_3P_2-termination surface, which resulted in the consequence that the decarbonylation mechanism to generate furan and carbon monoxide could be achieved on Ni_3P_1-termination surface, but could not be performed on the Ni_3P_2-termination surface.

5) The dimerisation reaction to produce difurfuryl ether could not be achieved without the participation of phosphorus.

6) In the section of further conversions of 2-methylfuran, the hydrogenation route to 2-methyltetrahydrofuran was kinetically favoured than the ring-opening route to generate the 2-pentanone. But their low yields were mainly determined by the weak adsorption strength of 2-methylfuran on the Ni_3P_2-termination surface.

Chapter 7 Conclusions and Recommendations

7.1. Conclusions

Based on the DFT calculations of the furfural hydrodeoxygenations, this study consisted of three sections: which were the hydrodeoxygenations of furfural on Ru/Co_3O_4 surface, Re/Pt bimetallic system, and Ni_2P (0001) surface, respectively. The conclusions of this work are summarised as below.

7.1.1. Furfural hydrotreating on Ru/Co_3O_4 surface

It was found that an oxygen vacancy was necessary to be created on the Ru/Co_3O_4 surface for the furfural adsorption to carry out the hydrodeoxygenation reactions. The oxygen vacancy could not be generated by hydrogen transfer on Co_3O_4 surface itself, as the activation barrier of reaction was too high to overcome. Upon the addition of ruthenium, the hydrogenation ability was improved dramatically, which made the oxygen vacancy was easy to form. The furfural was then adsorbed on the vacancy with the carbonyl oxygen was stabilised by the cobalt atoms, with the carbonyl carbon also bonded to a cobalt atom. During the furfural hydrodeoxygenation, the carbonyl carbon was first hydrogenated into the FCH_2O alkoxide intermediate, then the carbonyl C-O bond was cleaved, and finally the FCH_2 species was converted into 2-methylfuran via hydrogen transfer from surface oxygen. It was not necessary to generate furfuryl alcohol as an intermediate for the formation of 2-methylfuran, hence the minor yield of furfuryl alcohol detected in the experimental work should be attributed to the outstanding hydrogenation ability of ruthenium. The undesirable decarbonylation pathway was prohibited due to the adsorption

geometry of furfural on Ru/Co_3O_4 oxygen vacancy, because the C-C bond was difficult to be activated.

7.1.2. Furfural upgrading on Re/Pt bimetallic surface

Furfural adsorbed strongly via its furyl ring and carbonyl oxygen on the Re edge site of the Re/Pt bimetallic surface. The partial hydrogenation pathway to generate furfuryl alcohol was kinetically favoured via the alkoxide route; while the hydrodeoxygenation pathway to produce 2-methylfuran and water was thermodynamically favoured via the generation of hydroxyalkyl species first, followed by C-OH bond cleavage and successive hydrogenations of the furyl-CH intermediate. However, the 2-methylfuran generation was inhibited by the by-product oxygen species, because at the experimental temperature, the oxidised Re surface could not further accept oxygen depositions and the oxygen removal in terms of water was difficult. Hence the furfuryl alcohol was observed as the major product. By comparing with the flat Pt surface, the calculation results of Re/Pt system indicated that the incorporation of the oxophilic metal to active hydrogenation metals could decrease the activation barrier of C-O bond breaking, and inhibit the C-C bond cleavage for the undesirable furan production.

7.1.3. Furfural conversion on Ni_2P (0001) surface

As the Ni_2P (0001) facet was composed of Ni_3P_2 and Ni_3P_1 termination surfaces, the more stable Ni_3P_2-termination was mainly focused for the calculations. It was found that the generation of furfuryl alcohol was preferred via the hydroxyalkyl intermediate pathway, but it was not a necessary intermediate for the formation of the 2-methylfuran. While 2-

methylfuran was favoured to be generated via the hydrogenation of carbonyl oxygen of furfural first, followed by the C-OH bond breaking and successive hydrogenations of the FCH intermediate. Additionally, as the water was also generated as a by-product during 2-methylfuran production, it should be considered in the whole reaction mechanism; it was found that the water formation could be achieved either at the Ni trimer site or the Ni-P bridge site, in which the Ni trimer site route was facilitated. The inhibited decarbonylation pathway was determined by the adsorption geometry of furfural on the surface, which could be performed on the less abundant Ni_3P_1-termination but not on the Ni_3P_2-termination. The dimerisation for the difurfuryl ether formation could not be achieved without the participation of phosphorus. In the further reactions of 2-methylfuran, the formation of 2-methyltetrahydrofuran was kinetically favoured over the 2-pentanone. However, the weak adsorption strength of 2-methylfuran prevented it from further conversion.

7.2. Recommendations

Based on the DFT calculations of the furfural upgrading, the selectivity of the 2-methylfuran was mainly determined by the adsorption geometry of furfural on the catalyst surface. In order to selectively hydrogenolyse the carbonyl bond, the furyl ring should be repelled from the catalyst surface, which could be either achieved via the formation of surface oxygen vacancy or incorporation of oxophilic/electronegative elements to the active hydrogenation metals. While according to the calculation results, the oxygen vacancy formation was indicated to be a better choice due to the better hindrance of the ring-surface interaction, hence other combinations of active hydrogenation metals with

reducible metal oxides could have the potential for high efficiency production of 2-methylfuran from furfural.

Bibliography

1. J. L. Sawin, F. Sverrisson, W. Rickerson, C. Lins, L. E. Williamson, R. Adib, H. E. Murdock, E. Musolino, M. Hullin and A. Reith, 2015.
2. J. N. Chheda and J. A. Dumesic, *Catalysis Today*, 2007, 123, 59-70.
3. J. C. Serrano-Ruiz, R. M. West and J. A. Dumesic, *Annual review of chemical and biomolecular engineering*, 2010, 1, 79-100.
4. P. S. Nigam and A. Singh, *Progress in energy and combustion science*, 2011, 37, 52-68.
5. A. Ravishankara, Y. Rudich and J. A. Pyle, ACS Publications, 2015.
6. G. W. Huber, S. Iborra and A. Corma, *Chemical reviews*, 2006, 106, 4044-4098.
7. D. M. Alonso, J. Q. Bond and J. A. Dumesic, *Green Chemistry*, 2010, 12, 1493-1513.
8. J. H. Clark, V. Budarin, F. E. Deswarte, J. J. Hardy, F. M. Kerton, A. J. Hunt, R. Luque, D. J. Macquarrie, K. Milkowski and A. Rodriguez, *Green Chemistry*, 2006, 8, 853-860.
9. A. F. Lee and K. Wilson, *Catalysis Today*, 2015, 242, 3-18.
10. H. Lee, Y.-M. Kim, I.-G. Lee, J.-K. Jeon, S.-C. Jung, J. D. Chung, W. G. Choi and Y.-K. Park, *Korean Journal of Chemical Engineering*, 2016, 33, 3299-3315.
11. C. Kordulis, K. Bourikas, M. Gousi, E. Kordouli and A. Lycourghiotis, *Applied Catalysis B: Environmental*, 2016, 181, 156-196.
12. A. T. To and D. E. Resasco, *Applied Catalysis A: General*, 2014, 487, 62-71.
13. P. Lanzafame, G. Centi and S. Perathoner, *Catalysis Today*, 2014, 234, 2-12.
14. A. V. Bridgwater, *Biomass and Bioenergy*, 2012, 38, 68-94.
15. P. Bui, J. A. Cecilia, S. T. Oyama, A. Takagaki, A. Infantes-Molina, H. Zhao, D. Li, E. Rodríguez-Castellón and A. Jiménez López, *Journal of Catalysis*, 2012, 294, 184-198.
16. M. J. Climent, A. Corma and S. Iborra, *Green Chemistry*, 2014, 16, 516-547.
17. Q. Xia, Z. Chen, Y. Shao, X. Gong, H. Wang, X. Liu, S. F. Parker, X. Han, S. Yang and Y. Wang, *Nature Communications*, 2016, 7, 11162.
18. K. Barta and P. C. Ford, *Accounts of Chemical Research*, 2014, 47, 1503-1512.
19. J. N. Chheda, G. W. Huber and J. A. Dumesic, *Angewandte Chemie International Edition*, 2007, 46, 7164-7183.
20. M. Crocker, *Thermochemical conversion of biomass to liquid fuels and chemicals*, Royal Society of Chemistry, 2010.
21. R. Mariscal, P. Maireles-Torres, M. Ojeda, I. Sádaba and M. López Granados, *Energy & Environmental Science*, 2016, 9, 1144-1189.
22. Y. Sun and J. Cheng, *Bioresource Technology*, 2002, 83, 1-11.
23. D. J. M. Hayes, *Wiley Interdisciplinary Reviews: Energy and Environment*, 2013, 2, 304-334.
24. C. N. Hamelinck, G. v. Hooijdonk and A. P. C. Faaij, *Biomass and Bioenergy*, 2005, 28, 384-410.
25. A. Limayem and S. C. Ricke, *Progress in Energy and Combustion Science*, 2012, 38, 449-467.

26. F. Lenk, S. Bröring, P. Herzog and J. Leker, *Biotechnology Journal*, 2007, 2, 1497-1504.
27. J. J. Bozell and G. R. Petersen, *Green Chemistry*, 2010, 12, 539-554.
28. W. De Jong and G. Marcotullio, in *International Journal of Chemical Reactor Engineering*, 2010, vol. 8.
29. P. Gallezot, *Chemical Society Reviews*, 2012, 41, 1538-1558.
30. G. Centi, P. Lanzafame and S. Perathoner, *Catalysis Today*, 2011, 167, 14-30.
31. J.-P. Lange, E. van der Heide, J. van Buijtenen and R. Price, *ChemSusChem*, 2012, 5, 150-166.
32. A. Oasmaa and S. Czernik, *Energy & Fuels*, 1999, 13, 914-921.
33. F. A. Agblevor, O. Mante, R. McClung and S. T. Oyama, *Biomass and Bioenergy*, 2012, 45, 130-137.
34. R. Venderbosch and W. Prins, *Biofuels, bioproducts and biorefining*, 2010, 4, 178-208.
35. J. Wildschut, F. H. Mahfud, R. H. Venderbosch and H. J. Heeres, *Industrial & Engineering Chemistry Research*, 2009, 48, 10324-10334.
36. Q. Zhang, J. Chang, T. Wang and Y. Xu, *Energy Conversion and Management*, 2007, 48, 87-92.
37. M. Fatih Demirbas, *Applied Energy*, 2009, 86, S151-S161.
38. L. C. Meher, D. Vidya Sagar and S. N. Naik, *Renewable and Sustainable Energy Reviews*, 2006, 10, 248-268.
39. M. G. Kulkarni, R. Gopinath, L. C. Meher and A. K. Dalai, *Green Chemistry*, 2006, 8, 1056-1062.
40. J. Row and A. Doukas, *Fuel Quality in Canada: Impact on Tailpipe Emissions*, Pembina Institute, 2008.
41. S. N. Naik, V. V. Goud, P. K. Rout and A. K. Dalai, *Renewable and sustainable energy reviews*, 2010, 14, 578-597.
42. Y.-B. Huang and Y. Fu, *Green Chemistry*, 2013, 15, 1095-1111.
43. B. C. Saha, in *Handbook of industrial biocatalysis*, CRC Press, 2005, pp. 447-458.
44. J. P. Lange, E. Van Der Heide, J. van Buijtenen and R. Price, *ChemSusChem*, 2012, 5, 150-166.
45. J. Zakzeski, P. C. Bruijnincx, A. L. Jongerius and B. M. Weckhuysen, *Chemical reviews*, 2010, 110, 3552-3599.
46. J. P. Lange, *Biofuels, Bioproducts and Biorefining: Innovation for a sustainable economy*, 2007, 1, 39-48.
47. D. Mohan, C. U. Pittman and P. H. Steele, *Energy & fuels*, 2006, 20, 848-889.
48. F. Cherubini, G. Jungmeier, M. Wellisch, T. Willke, I. Skiadas, R. Van Ree and E. de Jong, *Biofuels, Bioproducts and Biorefining*, 2009, 3, 534-546.
49. R. A. Sheldon, *Chemicals from synthesis gas: catalytic reactions of CO and*, Springer Science & Business Media, 1983.
50. E. Rytter, E. Ochoa-Fernández and A. Fahmi, *Catalytic Process Development for Renewable Materials*, 2013, 10, 2.
51. A. Bridgwater, *Fuel*, 1995, 74, 631-653.

52. D. Sutton, B. Kelleher and J. R. Ross, *Fuel processing technology*, 2001, 73, 155-173.
53. S. Czernik and A. Bridgwater, *Energy & fuels*, 2004, 18, 590-598.
54. S. Chen, R. Wojcieszak, F. Dumeignil, E. Marceau and S. b. Royer, *Chemical reviews*, 2018, 118, 11023-11117.
55. K. Zeitsch, Elsevier, The Netherlands, 2000.
56. K. J. Zeitsch, *The chemistry and technology of furfural and its many by-products*, Elsevier, 2000.
57. K. Yan, G. Wu, T. Lafleur and C. Jarvis, *Renewable and sustainable energy reviews*, 2014, 38, 663-676.
58. I. Agirrezabal-Telleria, I. Gandarias and P. Arias, *Catalysis Today*, 2014, 234, 42-58.
59. A. S. Mamman, J. M. Lee, Y. C. Kim, I. T. Hwang, N. J. Park, Y. K. Hwang, J. S. Chang and J. S. Hwang, *Biofuels, Bioproducts and Biorefining: Innovation for a sustainable economy*, 2008, 2, 438-454.
60. L. R. Lynd, J. H. Cushman, R. J. Nichols and C. E. Wyman, *Science*, 1991, 251, 1318-1323.
61. R. Xing, W. Qi and G. W. Huber, *Energy & Environmental Science*, 2011, 4, 2193-2205.
62. B. Sain, A. Chaudhuri, J. Borgohain, B. Baruah and J. Ghose, *JOURNAL OF SCIENTIFIC & INDUSTRIAL RESEARCH*, 1982, 41, 431-438.
63. M. S. Feather, D. W. Harris and S. B. Nichols, *The Journal of Organic Chemistry*, 1972, 37, 1606-1608.
64. C. Wang, H. Xu, R. Daniel, A. Ghafourian, J. M. Herreros, S. Shuai and X. Ma, *Fuel*, 2013, 103, 200-211.
65. A. Bohre, S. Dutta, B. Saha and M. M. Abu-Omar, *ACS Sustainable Chemistry & Engineering*, 2015, 3, 1263-1277.
66. X. Ma, C. Jiang, H. Xu, H. Ding and S. Shuai, *Fuel*, 2014, 116, 281-291.
67. M. I. Alam, S. De, S. Dutta and B. Saha, *RSC Advances*, 2012, 2, 6890-6896.
68. R. M. West, Z. Y. Liu, M. Peter, C. A. Gärtner and J. A. Dumesic, *Journal of Molecular Catalysis A: Chemical*, 2008, 296, 18-27.
69. H. Kobayashi and A. Fukuoka, *Green Chemistry*, 2013, 15, 1740-1763.
70. S. De, B. Saha and R. Luque, *Bioresource Technology*, 2015, 178, 108-118.
71. S. Sitthisa and D. E. Resasco, *Catalysis letters*, 2011, 141, 784-791.
72. Y. Zhao, *Environmental chemistry letters*, 2014, 12, 185-190.
73. J. G. Stevens, R. A. Bourne, M. V. Twigg and M. Poliakoff, *Angewandte Chemie International Edition*, 2010, 49, 8856-8859.
74. T. Ishida, K. Kume, K. Kinjo, T. Honma, K. Nakada, H. Ohashi, T. Yokoyama, A. Hamasaki, H. Murayama, Y. Izawa, M. Utsunomiya and M. Tokunaga, *ChemSusChem*, 2016, 9, 3441-3447.
75. N. S. Biradar, A. A. Hengne, S. N. Birajdar, R. Swami and C. V. Rode, *Organic Process Research & Development*, 2014, 18, 1434-1442.
76. M. J. Taylor, L. J. Durndell, M. A. Isaacs, C. M. Parlett, K. Wilson, A. F. Lee and G. Kyriakou, *Applied Catalysis B: Environmental*, 2016, 180, 580-585.

77. P. Panagiotopoulou and D. G. Vlachos, *Applied Catalysis A: General*, 2014, 480, 17-24.
78. M. Lesiak, M. Binczarski, S. Karski, W. Maniukiewicz, J. Rogowski, E. Szubiakiewicz, J. Berlowska, P. Dziugan and I. Witońska, *Journal of Molecular Catalysis A: Chemical*, 2014, 395, 337-348.
79. F. Dong, Y. Zhu, H. Zheng, Y. Zhu, X. Li and Y. Li, *Journal of Molecular Catalysis A: Chemical*, 2015, 398, 140-148.
80. F. Dong, G. Ding, H. Zheng, X. Xiang, L. Chen, Y. Zhu and Y. Li, *Catalysis Science & Technology*, 2016, 6, 767-779.
81. N. S. Date, A. M. Hengne, K. W. Huang, R. C. Chikate and C. V. Rode, *Green Chemistry*, 2018, 20, 2027-2037.
82. S. Sitthisa, W. An and D. E. Resasco, *Journal of catalysis*, 2011, 284, 90-101.
83. C. Wang, J. Luo, V. Liao, J. D. Lee, T. M. Onn, C. B. Murray and R. J. Gorte, *Catalysis Today*, 2018, 302, 73-79.
84. C. P. Jiménez-Gómez, J. A. Cecilia, C. García-Sancho, R. Moreno-Tost and P. Maireles-Torres, *ACS Sustainable Chemistry & Engineering*, 2019, 7, 7676-7685.
85. B. Seemala, C. M. Cai, R. Kumar, C. E. Wyman and P. Christopher, *ACS Sustainable Chemistry & Engineering*, 2018, 6, 2152-2161.
86. Z. Fu, Z. Wang, W. Lin, W. Song and S. Li, *Applied Catalysis A: General*, 2017, 547, 248-255.
87. Y. Nakagawa, K. Takada, M. Tamura and K. Tomishige, *ACS Catalysis*, 2014, 4, 2718-2726.
88. X. Chang, A. F. Liu, B. Cai, J. Y. Luo, H. Pan and Y. B. Huang, *ChemSusChem*, 2016, 9, 3330-3337.
89. N. Pino, S. Sitthisa, Q. Tan, T. Souza, D. López and D. E. Resasco, *Journal of Catalysis*, 2017, 350, 30-40.
90. D. Shi and J. M. Vohs, *ACS Catalysis*, 2015, 5, 2177-2183.
91. B. Chen, F. Li, Z. Huang and G. Yuan, *Applied Catalysis A: General*, 2015, 500, 23-29.
92. A. B. Merlo, V. Vetere, J. F. Ruggera and M. L. Casella, *Catalysis Communications*, 2009, 10, 1665-1669.
93. M. G. Dohade and P. L. Dhepe, *Clean Technologies and Environmental Policy*, 2018, 20, 703-713.
94. Z. Jiang, W. Wan, Z. Lin, J. Xie and J. G. Chen, *ACS Catalysis*, 2017, 7, 5758-5765.
95. S. K. Jaatinen, R. S. Karinen and J. S. Lehtonen, *ChemistrySelect*, 2017, 2, 51-60.
96. B. Seemala, R. Kumar, C. M. Cai, C. E. Wyman and P. Christopher, *Reaction Chemistry & Engineering*, 2019, 4, 261-267.
97. M. Tamura, K. Tokonami, Y. Nakagawa and K. Tomishige, *Chemical Communications*, 2013, 49, 7034-7036.
98. Z. Sun, X. Li, A. Wang, Y. Wang and Y. Chen, *Topics in Catalysis*, 2012, 55, 1010-1021.
99. I. I. Abu and K. J. Smith, *Journal of Catalysis*, 2006, 241, 356-366.
100. K. Li, R. Wang and J. Chen, *Energy & Fuels*, 2011, 25, 854-863.

101. H. Zhao, D. Li, P. Bui and S. Oyama, *Applied Catalysis A: General*, 2011, 391, 305-310.
102. C. P. Jiménez‐Gómez, J. A. Cecilia, R. Moreno‐Tost and P. Maireles‐Torres, *ChemCatChem*, 2017, 9, 2881-2889.
103. Y. Wang, F. Liu, H. Han, L. Xiao and W. Wu, *ChemistrySelect*, 2018, 3, 7926-7933.
104. Y. Bonita, V. Jain, F. Geng, T. P. O'Connell, W. N. Wilson, N. Rai and J. C. Hicks, *Catalysis Science & Technology*, 2019, 9, 3656-3668.
105. A. Sampath, S. A. Chang and D. W. Flaherty, *The Journal of Physical Chemistry C*, 2018, 122, 23600-23609.
106. M. Bradley, J. Robinson and D. Woodruff, *Surface Science*, 2010, 604, 920-925.
107. B. Liu, L. Cheng, L. Curtiss and J. Greeley, *Surface Science*, 2014, 622, 51-59.
108. K. Xiong, W. Wan and J. G. Chen, *Surface Science*, 2016, 652, 91-97.
109. Z.-M. NI, M.-Y. XIA, W. SHI and P.-P. QIAN, *Acta Physico-Chimica Sinica*, 2013, 29, 1916-1922.
110. Q. X. Cai, J. G. Wang, Y. G. Wang and D. Mei, *AIChE Journal*, 2015, 61, 3812-3824.
111. S. Sitthisa, T. Pham, T. Prasomsri, T. Sooknoi, R. G. Mallinson and D. E. Resasco, *Journal of catalysis*, 2011, 280, 17-27.
112. V. Vorotnikov, G. Mpourmpakis and D. G. Vlachos, *ACS Catalysis*, 2012, 2, 2496-2504.
113. A. Banerjee and S. H. Mushrif, *ChemCatChem*, 2017, 9, 2828-2838.
114. A. Banerjee and S. H. Mushrif, *The Journal of Physical Chemistry C*, 2018, 122, 18383-18394.
115. Y. Shi, Y. Zhu, Y. Yang, Y.-W. Li and H. Jiao, *ACS Catalysis*, 2015, 5, 4020-4032.
116. S. Sitthisa, T. Sooknoi, Y. Ma, P. B. Balbuena and D. E. Resasco, *Journal of catalysis*, 2011, 277, 1-13.
117. W. Yu, K. Xiong, N. Ji, M. D. Porosoff and J. G. Chen, *Journal of catalysis*, 2014, 317, 253-262.
118. W. Wan, Z. Jiang and J. G. Chen, *Topics in Catalysis*, 2018, 61, 439-445.
119. C. R. Second, E. Edition, G. Ertl, H. Knözinger, F. Schüth, J. Weitkamp, W.-V. V. G. KGaA and Co, 2008.
120. I. Langmuir, *Journal of the American chemical society*, 1916, 38, 2221-2295.
121. G. A. Somorjai and Y. Li, *Introduction to surface chemistry and catalysis*, John Wiley & Sons, 2010.
122. D. P. Woodruff, *Modern techniques of surface science*, Cambridge university press, 2016.
123. R. I. Masel, *Principles of adsorption and reaction on solid surfaces*, John Wiley & Sons, 1996.
124. M. Born and R. Oppenheimer, *Annalen der physik*, 1927, 389, 457-484.
125. J. C. Slater, *Physical review*, 1951, 81, 385.
126. P. Hohenberg and W. Kohn, *Kohn W, Sham LJ (1965) Phys Rev*, 1964, 140, A1133.
127. W. Kohn and L. J. Sham, *Physical Review*, 1965, 140, A1133-A1138.

128. L. Hedin and B. I. Lundqvist, *Journal of Physics C: Solid state physics*, 1971, 4, 2064.
129. P. Hu, D. King, S. Crampin, M.-H. Lee and M. Payne, *Chemical physics letters*, 1994, 230, 501-506.
130. J. Joannopoulos, Plenum, New York, 1985.
131. J. P. Perdew, S. Kurth, A. Zupan and P. Blaha, *Physical review letters*, 1999, 82, 2544.
132. J. P. Perdew, K. Burke and M. Ernzerhof, *Physical Review Letters*, 1996, 77, 3865-3868.
133. N. W. Ashcroft and N. Mermin, *Physics (New York: Holt, Rinehart and Winston)*, 1976, 131-151,561.
134. J. C. Slater, *Physical Review*, 1930, 36, 57.
135. R. Ditchfield, W. J. Hehre and J. A. Pople, *The Journal of Chemical Physics*, 1971, 54, 724-728.
136. J. C. Phillips, *Physical Review*, 1958, 112, 685.
137. M. Yin and M. L. Cohen, *Physical review B*, 1982, 25, 7403.
138. L. Kleinman and D. Bylander, *Physical Review Letters*, 1982, 48, 1425.
139. D. Vanderbilt, *Physical review B*, 1990, 41, 7892.
140. G. Kresse and J. Furthmüller, *Computational Materials Science*, 1996, 6, 15-50.
141. G. Kresse and J. Hafner, *Physical Review B*, 1994, 49, 14251-14269.
142. J. Cheng, T. Song, P. Hu, C. M. Lok, P. Ellis and S. French, *Journal of catalysis*, 2008, 255, 20-28.
143. R. Cortright and J. Dumesic, 2001.
144. A. A. Gokhale, S. Kandoi, J. P. Greeley, M. Mavrikakis and J. A. Dumesic, *Chemical Engineering Science*, 2004, 59, 4679-4691.
145. R. Dennington, T. Keith and J. Millam, *Semichem Inc.: Shawnee Mission, KS*, 2009.
146. M. Frisch, G. Trucks, H. Schlegel, G. Scuseria, M. Robb, J. Cheeseman, G. Scalmani, V. Barone, B. Mennucci and G. Petersson, *There is no corresponding record for this reference*, 2015.
147. S. Grimme, J. Antony, S. Ehrlich and H. Krieg, *The Journal of chemical physics*, 2010, 132, 154104.
148. S. L. Dudarev, G. A. Botton, S. Y. Savrasov, C. J. Humphreys and A. P. Sutton, *Physical Review B*, 1998, 57, 1505-1509.
149. J. Wang, X. Liu, B. Hu, G. Lu and Y. Wang, *RSC Advances*, 2014, 4, 31101-31107.
150. J. Hutchison and N. Briscoe, *Ultramicroscopy*, 1985, 18, 435-438.
151. S. Petitto and M. Langell, *Journal of Vacuum Science & Technology A: Vacuum, Surfaces, and Films*, 2004, 22, 1690-1696.
152. S. Petitto and M. Langell, *Surface science*, 2005, 599, 27-40.
153. S. C. Petitto, E. M. Marsh, G. A. Carson and M. A. Langell, *Journal of Molecular Catalysis A: Chemical*, 2008, 281, 49-58.
154. W. Meyer, K. Biedermann, M. Gubo, L. Hammer and K. Heinz, *Journal of Physics: Condensed Matter*, 2008, 20, 265011.

155. X.-L. Xu, Z.-H. Chen, Y. Li, W.-K. Chen and J.-Q. Li, *Surface Science*, 2009, 603, 653-658.
156. L. Hu, Q. Peng and Y. Li, *Journal of the American Chemical Society*, 2008, 130, 16136-16137.
157. X. Xie and W. Shen, *Nanoscale*, 2009, 1, 50-60.
158. X. Xie, Y. Li, Z.-Q. Liu, M. Haruta and W. Shen, *Nature*, 2009, 458, 746.
159. H.-F. Wang, R. Kavanagh, Y.-L. Guo, Y. Guo, G. Lu and P. Hu, *Journal of catalysis*, 2012, 296, 110-119.
160. H. F. Wang, R. Kavanagh, Y. L. Guo, Y. Guo, G. Z. Lu and P. Hu, *Angewandte Chemie International Edition*, 2012, 51, 6657-6661.
161. S. Selcuk and A. Selloni, *The Journal of Physical Chemistry C*, 2015, 119, 9973-9979.
162. L. Wang, T. Maxisch and G. Ceder, *Physical Review B*, 2006, 73, 195107.
163. P. E. Blöchl, O. Jepsen and O. K. Andersen, *Physical Review B*, 1994, 49, 16223-16233.
164. G. Kresse and D. Joubert, *Physical Review B*, 1999, 59, 1758-1775.
165. Z.-P. Liu and P. Hu, *Journal of the American Chemical Society*, 2003, 125, 1958-1967.
166. A. Alavi, P. Hu, T. Deutsch, P. L. Silvestrelli and J. Hutter, *Physical Review Letters*, 1998, 80, 3650-3653.
167. X. Sun, X. Cao and P. Hu, *Science China Chemistry*, 2015, 58, 553-564.
168. A. Michaelides and P. Hu, *Journal of the American Chemical Society*, 2001, 123, 4235-4242.
169. P. L. Meena, R. Kumar and K. Sreenivas, *AIP Conference Proceedings*, 2013, 1512, 1204-1205.
170. P. Dutta, M. Seehra, S. Thota and J. Kumar, *Journal of Physics: Condensed Matter*, 2007, 20, 015218.
171. Z. Wang, X. M. Cao, J. Zhu and P. Hu, *Journal of Catalysis*, 2014, 311, 469-480.
172. Z. Wang, H.-F. Wang and P. Hu, *Chemical Science*, 2015, 6, 5703-5711.
173. S. H. Pang and J. W. Medlin, *Acs Catalysis*, 2011, 1, 1272-1283.
174. M. J. Gilkey, P. Panagiotopoulou, A. V. Mironenko, G. R. Jenness, D. G. Vlachos and B. Xu, *Acs Catalysis*, 2015, 5, 3988-3994.
175. R. C. Nelson, B. Baek, P. Ruiz, B. Goundie, A. Brooks, M. C. Wheeler, B. G. Frederick, L. C. Grabow and R. N. Austin, *ACS catalysis*, 2015, 5, 6509-6523.
176. Y. Zu, P. Yang, J. Wang, X. Liu, J. Ren, G. Lu and Y. Wang, *Applied Catalysis B: Environmental*, 2014, 146, 244-248.
177. C. Y. Ma, Z. Mu, J. J. Li, Y. G. Jin, J. Cheng, G. Q. Lu, Z. P. Hao and S. Z. Qiao, *Journal of the American Chemical Society*, 2010, 132, 2608-2613.
178. R. Burch, C. Paun, X. M. Cao, P. Crawford, P. Goodrich, C. Hardacre, P. Hu, L. McLaughlin, J. Sá and J. M. Thompson, *Journal of Catalysis*, 2011, 283, 89-97.
179. P. J. Feibelman, *Science*, 2002, 295, 99-102.
180. A. Michaelides, A. Alavi and D. A. King, *Journal of the American Chemical Society*, 2003, 125, 2746-2755.
181. W. Wan, Z. Jiang and J. G. Chen, *Topics in Catalysis*, 2018, 1-7.
182. C. Zhang, Q. Lai and J. H. Holles, *Catalysis Communications*, 2017, 89, 77-80.

183. Y. Li, X. Yang, L. Zhu, H. Zhang and B. Chen, *RSC Advances*, 2015, 5, 80388-80396.
184. S. T. Oyama, *Journal of Catalysis*, 2003, 216, 343-352.
185. A. Iino, A. Cho, A. Takagaki, R. Kikuchi and S. Ted Oyama, *Journal of Catalysis*, 2014, 311, 17-27.
186. R. Prins and M. E. Bussell, *Catalysis Letters*, 2012, 142, 1413-1436.
187. W. Hu, J. Lan, Y. Guo, X.-M. Cao and P. Hu, *ACS Catalysis*, 2016, 6, 5508-5519.
188. J. Wang, H. Wang and P. Hu, *Science China Chemistry*, 2018, 61, 336-343.
189. M. Yang, H. Yuan, H. Wang and P. Hu, *Science China Chemistry*, 2018, 61, 457-467.
190. J. A. Rodriguez, J.-Y. Kim, J. C. Hanson, S. J. Sawhill and M. E. Bussell, *The Journal of Physical Chemistry B*, 2003, 107, 6276-6285.
191. Q. Li and X. Hu, *Physical Review B*, 2006, 74, 035414.
192. Q. Yuan, H. Ariga and K. Asakura, *Topics in Catalysis*, 2015, 58, 194-200.
193. A. E. Nelson, M. Sun and A. S. M. Junaid, *Journal of Catalysis*, 2006, 241, 180-188.
194. A. B. Hernandez, H. Ariga, S. Takakusagi, K. Kinoshita, S. Suzuki, S. Otani, S. T. Oyama and K. Asakura, *Chemical Physics Letters*, 2011, 513, 48-52.
195. U. Guharoy, T. Ramirez Reina, E. Olsson, S. Gu and Q. Cai, *ACS Catalysis*, 2019, 9, 3487-3497.
196. Á. Morales-García, J. He, P. Lyu and P. Nachtigall, *Biomass Conversion and Biorefinery*, 2017, 7, 377-383.
197. Y. Mao, Z. Wang, H.-F. Wang and P. Hu, *ACS Catalysis*, 2016, 6, 7882-7891.
198. J. Cheng, P. Hu, P. Ellis, S. French, G. Kelly and C. M. Lok, *The Journal of Physical Chemistry C*, 2008, 112, 1308-1311.
199. M. Choura, N. M. Belgacem and A. Gandini, *Macromolecules*, 1996, 29, 3839-3850.
200. H. Dong, Y. Zheng and P. Hu, *Physical Chemistry Chemical Physics*, 2019, 21, 8384-8393.

Curriculum Vitae

Candidate's full name: He Dong

Universities attended:

Master of Science in Chemistry, Queen's University of Belfast, Belfast, United Kingdom, 2015.6

Publications:

1. H. Dong, Y. Zheng and P. Hu, *Physical Chemistry Chemical Physics*, 2019, 21, 1597-1605.

2. H. Dong, Y. Zheng and P. Hu, *Physical Chemistry Chemical Physics*, 2019, 21, 8384-8393.